Title

Stretchable Electronics and Soft Actuators via Elastic Instability Design and Facile Fabrication

Author

Xu, Renxiao

Publication Date

2020

Stretchable Electronics and Soft Actuators

via Elastic Instability Design and Facile Fabrication

By

Renxiao Xu

A dissertation submitted in partial satisfaction of the

requirements for the degree of

Doctor of Philosophy

in

Engineering - Mechanical Engineering

in the

Graduate Division

of the

University of California, Berkeley

Committee in charge:

Professor Liwei Lin, Chair

Professor Hayden Taylor

Professor Ali Javey

Fall 2020

Abstract

Stretchable Electronics and Soft Actuators

via Elastic Instability Design and Facile Fabrication

by

Renxiao Xu

Doctor of Philosophy in Mechanical Engineering

University of California, Berkeley

Professor Liwei Lin, Chair

Soft and deformable electronics and actuators have attracted high research interests toward practical applications. This work focuses on two goals: (1) applying the concept of elastic instability in the structural design for soft systems; and (2) exploring rapid and low-cost schemes for their facile fabrications. Specifically, Kirigami, curved serpentines, auxetics, bistable and multistable structures, have all been utilized in different electronics and actuator systems to obtain unique and desirable properties, such as ultrahigh deformability, omnidirectional stretchability, and impact-resistant mechanics in this work.

First, a construct inspired by Kirigami designs has been developed to make highly deformable micro-supercapacitor patches with high areal coverages of electrode and electrolyte materials. These patches are fabricated in simple and efficient steps by a laser assisted graphitic conversion and cutting process, utilizing different laser power and scanning speeds on a laser cutter. The Kirigami cuts significantly increase the structural compliance such that individual segments in the patches can buckle, rotate, bend and twist to accommodate large overall deformations with only a small strain in active electrode areas. Electrochemical testing results have proved that electrochemical performances are preserved under large deformations up to 282.5% of overall structural elongations.

A time- and cost-effective fabrication approach to construct stretchable electronics with the "island-bridge" constructs has been established without using photomasks. A low-cost commercially available vinyl cutter is used to define patterns by adjusting the cutting force and

depth on the blade. Metal interconnects and pads can be patterned via the "tunnel cut" process and the flexible overall structure can be defined via the "through cut" process. The capabilities of the proposed method is shown by two demonstration devices, a skin-mounted module for monitoring breathing and a water-resistant supercapacitor array with omni-directionally stretchable capability. These devices can accommodate large deformations through the buckling and post-buckling instability without affecting their functions.

Finally, a class of magnetically powered, untethered soft actuators has been built based on a bioinspired "flesh-and-bone" construct. This construct has both key attributes of fast actuation and compliant impact-resistant mechanics and it also renders a simple fabrication process using generic 3D printers and off-the-shelf neodymium magnets as well as silicone elastomers. Actuators of diverse shapes of elastomeric "fleshes" and different placements of magnetic "bones" have displayed several distinct types of tasks, including auxetic expansion and shrinking, out-of-plane transformations, transition among multiple stable states, and manipulation of small objects.

Table of Contents

List of Figures

Chapter 1

Chapter 2

patch (SMSP) with parallel, alternating offset Kirigami cuts. **(a)** 3D exploded view and **(b)** top view illustrations of the layout in the SMSP. Different colors denote three key constituents: Kirigami cutting slots (red), graphitic electrodes (black), and polymer-based electrolyte (semi-transparent blue). **(c)** Cyclic voltammetry and **(d)** galvanostatic charge/discharge tests of the SMSP. **(e-g)** Optical image of (f) SMSP and (g) an intact polyimide sheet of the same size in initial and deformed configurations.

Figure 2.7 Buckling determinism analysis of a representative SMSP. **(a)** The first four buckling modes of a SMSP shown in top view (top row), side view (middle row) and 3D view (bottom row). The color denotes out-of-plane displacement. **(b)** Critical buckling strain corresponding to the first four modes. **(c)** Deformation energy as a function of elongation for the first four modes. Mode 1 (shown in red) has both the smallest critical buckling strain and the lowest deformation energy.

Figure 2.8 **(a)** Schematic illustration of the experimental setup for measuring resistance of test sample during its bending deformation. **(b)** The relative change in resistance of the test sample as a function of the relative change in length, for both upward (blue) and downward (red) bending. **(c)** The FEA-predicted (top left in each group) and experimentally observed (top right in each group) deformation of the test sample at 50% compression. The color in the top view FEA image of the test sample denotes computed maximum absolute principal strain.

Figure 2.9 **(a)** Post-buckling deformation of a representative SMSP, featuring FEA predictions (left column) and optical images (right column) of the SMSP at four deformation stages. The center column highlights strain distributions at selected sites with large deformation at each stage of deformation. Color in FEA images denotes computed maximum absolute principal strain. **(b)** Cyclic voltammetry curves and **(c)** capacitance retentions of the SMSP under different elongations. The scan rate is 200 mV/s.

Figure 2.10 Deformation of the SMSP with “alternating offset cuts” design at elongations beyond 282.5%, predicted by FEA. The magnified view shows the distribution of maximum absolute principal strain $\varepsilon_{\max}$ in the graphitic material, at the site with the largest deformation. $\varepsilon_{\max}$ reaches 5.5% when the overall elongation is 510%. The circles highlight local regions where $\varepsilon_{\max}$ is greater than 5.5% (with grey or black colors).

Figure 2.11 Optical images of the SMSP at different stages of deformation in a stretching test by hand.

Figure 2.12 Design, deformation and performances of SMSPs with two other Kirigami-inspired designs, namely, **(a-d)** the “double spiral” design and **(e-h)** the “zigzag serpentine” design. In (a) and (e), colors denote the layout of electrodes (black), Kirigami cuts (red) and electrolyte (semi-

Chapter 3

blue for the Mylar film. Scale bars: 50 μm in (d), 5 μm in (e). **(f)** Cyclic Voltammetry of one WSSC unit and a control group sample before and after 16-hour water immersion.

Figure 3.6 **(a)** Fabrication processes for WSSC using the two-mode mechanical cutting process. **(b)** A time break-up for each fabrication steps shown in (a). Five samples are fabricated simultaneously.

Figure 3.7 Electrochemical and water resistivity evaluations of one WSSC unit. **(a-b)** Optical images of one WSSC unit and a control group sample (a) in top views and (b) immersed in water. **(c)** Areal capacitance vs. discharge current density for one WSSC unit and the control group sample. **(d-e)** Nyquist plots of one WSSC unit and the control group sample before and after 16-hour water immersion.

Figure 3.8 **(a-c)** Optical images of WSSC (a) in its initial configuration, (b) folded by hand to half and (c) folded to 1/6 of its initial nominal area. **(d-e)** Equi-biaxial stretching of WSSC, as (d) recorded in experiments and (e) predicted by FEA. **(f)** Cyclic Voltammetry measurement of the entire device. The measurement was performed before and after repetitive deformation and extensive water immersion. **(g-j)** Uniaxial elongation (left column) and out-of-plane stretching (center column) of WSSC, as (g,i) recorded in experiments and (h,j) predicted by FEA. Color in FEA results denotes maximum principal strain in the layer of gold collectors and interconnects.

Figure 3.9 Stretchable skin-mounted human breath monitor module. **(a)** Schematic illustration of the device. **(b)** Optical image of the device mounted on a volunteer's face. **(c)** Magnified optical image featuring one unit-cell in the device. Scale bar: 2 mm. **(d-f)** Demonstration of the device's mechanical compliance and deformability. The device can be (d) wrapped on a stirring rod, (e) twisted, and (f) stretched by hands. **(g)** The breathing patterns of a volunteer in three different scenarios. **(h)** Magnitude scalogram representation of a volunteers' breathing patterns for post-exercise recovery. **(i-j)** Breathing signals from (i) a volunteer with symmetric nose and (j) a volunteer with nasal septum deviation, as captured by sensors at different locations.

Figure 3.10 Fabrication processes for the stretchable skin-mounted breath monitor module using two-mode mechanical cutting.

Chapter 4

Figure 4.1 **(a)** The flexing of a human arm, featuring the bones and flesh components. **(b)** Schematics of the working mechanism of a bioinspired bone-and-flesh actuator, with magnets as "bones" and elastomers as "flesh". **(c)** Effective modulus, and **(d)** deformability (evaluated by the amount of elongation at break) of “bone” and “flesh” components in human body and in the proposed actuators.

Figure 4.2 **(a)** Experimental setup for testing an actuator’s response under an alternating magnetic field. **(b)** Response vs. drive frequency of an actuator, as read from video images at 240 frames/sec. **(c)** Comparison in actuation time between magnetically powered soft actuators and actuators of similar length scale but using other working mechanisms. The numbers in the square brackets denote the corresponding references.

Figure 4.3 **(a-b)** Recorded sequence images during a free-fall drop test, for a column-shaped magnet (a) with and (b) without the encapsulating elastomeric “flesh”. The inset in (a) shows the intact structure after the test. **(c)** Force on magnet and **(d)** elastic strain energy in the magnet during the impact with the ground, as computed by FEA. **(e)** Maximum principal strain distribution on the magnet (with or without “flesh”) after impact(s), as computed by FEA.

Figure 4.4 **(a-b)** Schematics of the free-fall drop test and FEA simulations, for a column-shaped magnet (a) encapsulated with elastomeric “flesh” and (b) without “flesh”. **(c)** Sequence images from FEA, showing the bone-and-flesh structure’s 1st and 2nd impact, and eventual departure from the ground. **(d)** Force and **(e)** kinetic and elastic strain energy during the impacts with ground, as calculated from FEA.

Figure 4.5 Fabrication procedures of bone-and-flesh soft actuators. **(a)** 3D print ABS molds. **(b)** Fill the printed mold with Ecoflex and cure in room temperature. **(c)** Place and seal NdFeB magnets into selected sites. **(d)** Test and actuate the device under an external magnetic field.

Figure 4.6 **(a)** Schematics of a soft actuator for 2D auxetic contraction, in top and side views. The red/blue arrows denote the polarity of magnets, and the 1cm scale bar shows the overall dimensions of the actuator. **(b)** Recorded (top row) and computed (bottom row) deformation of the actuator, during four representative stages. **(c)** Percentage decrease in lengths and nominal area vs. the rotation angle of magnets during the contraction actuation, as predicted by FEA (lines) and measured in experiments (dots). **(d)** Schematics of a soft actuator for 2D auxetic expansion, in top and side views. **(e)** Recorded (top row) and computed (bottom row) deformation of the actuator, during four representative stages. **(f)** Percentage increase in lengths and nominal area vs. the rotation angle of magnets during the contraction actuation, as predicted by FEA (lines) and measured in experiments (dots). For panels (b) and (e), colors in FEA results denote total displacement.

Figure 4.7 **(a)** Schematics of a soft actuator for 3D auxetic contraction, featuring the “flesh” (left column) and the 36 “bones” (right column). The red/blue arrows denote the representative polarity of magnets. **(b)** Recorded and **(c)** computed shape of the actuator in (a), without (left) and with (right) external magnetic field. **(d)** Schematics of a soft actuator for 3D auxetic expansion, featuring the "flesh" (left column) and the 36 "bones" (right column). **(e)** Recorded and **(f)** computed shape of the actuator in (d), without (left) and with (right) external magnetic field.

Figure 4.8 **(a)** Schematics of a soft actuator for bending-based 2D-to-3D transformation, in top and side views. **(b)** Recorded (top column) and computed (bottom column) transitions among the "butterfly" state, the undeformed flat state, and the "saddle" state. **(c)** Changes in height and length vs. magnet rotation angle during the actuation process. **(d)** Schematics of a soft actuator for Origami-type 2D-to-3D transformation, in top, side and tilted 3D views. **(e)** Recorded (top column) and computed (bottom column) transitions among the "Red-Up" state, the undeformed flat state, and the "Blue-Up" state. In photos, the letters "R" and "B" denote red and blue faces, respectively. **(f)** Schematics of a soft actuator with magnet bundles for 2D-to-3D transformation, in top, side and tilted 3D views. The inset shows a cross-sectional profile of a two-bone and a three-bone bundle. **(g)** Recorded (top column) and computed (bottom column) deformations during the actuation process. For panels (b) and (g), colors in FEA denote out-of-plane displacement.

Figure 4.9 **(a)** Schematics of a bistable, pop-up switch, in top and 3D tilted views. **(b)** Recorded (top row) and computed (bottom row) images for the process of mechanical loading/unloading (first three columns) and magnetically powered reset (last column). Colors in FEA denote normalized out-of-plane displacement. **(c)** Schematics of a multistable tower, in bottom and 3D tilted views. The red/blue arrows denote the representative polarity of magnets. **(d)** Recorded (top row) and computed (bottom row) images showing the four stable states of the system in (c). Colors in FEA denote out-of-plane displacement. **(e-f)** Elastic strain energy and applied force vs. normalized displacement in the z-direction for (e) the bistable, pop-up switch, and (f) the multistable tower.

Figure 4.10 **(a)** Schematics of a six-finger bone-and-flesh gripper, in top and 3D tilted views. **(b)** FEA-predicted deformation in the tightening and the opening modes. Colors denote total displacement. **(c)** Optical images demonstrating the grasping, transferring and release of a small object. **(d-f)** Optical images of the gripper manipulating (d) a peanut, (e) a screw bolt and (f) a set of nut, washer and bolt.

Acknowledgements

The doctoral study at Berkeley has been such an interesting learning experience for me. During the process, I am grateful that I have received invaluable help and support from many individuals. First of all, I would like to thank my advisor, Prof. Liwei Lin, for his strong support and insightful guidance during the Ph.D. program. Apart from his professional opinions in research, I have also benefited a lot from his generous advice in career developments. I could not thank him enough.

I am also grateful to Prof. Hayden Taylor and Prof. Ali Javey, who have been kind enough to serve as members in both my dissertation committee and qualifying exam committee. Their comments and suggestions during and since my qualifying presentation have helped my research projects tremendously. In addition, I would like to thank many other professors who have taught me or helped me during my graduate studies. They have added to my knowledge base and made me a better scholar.

Although a Ph.D. program is full of hardship, I am fortunate enough to have a positive experience overall, which I owe to my wonderful coworkers and friends. I would like to thank my fellow Ph.D. students and visiting scholars in the Liwei Lin Lab, including but not limited to Dr. Takeshi Hayasaka, Dr. Caiwei Shen, Peisheng He, Fanping Sui, Ruiqi Guo, Yu Long, Yande Peng, Kamyar Behrouzi, Dongkai Wang, Tao Jiang, Dr. Yuanyuan Huang, Dr. Po Chen Yeh, Wenying Qiu, and Bing Zhang, etc.. I would also thank the more than twenty undergraduate students who have contributed to my research projects, in particular Guangchen Lan, Wei Yue, and Liangjie Ren. All of the aforementioned people have offered me great assistance and suggestions, and made the lab a happy place. Besides, I also want to thank the staff members at Berkeley Marvell NanoLab, Biomolecular Nanotechnology Center, Berkeley Sensor and Actuator Center, and the Molecular Foundry for facilitating parts of my research. Apart from research, I would acknowledge my friends at Berkeley and in many other places for listening to my complaints and worries and offering me great suggestions and moral support. They have filled a monotonic graduate life with lots of fun.

Last but definitely one of the most important, I would like to express my sincere gratitude to my parents, my grandparents, and many other relatives of mine, for their understanding, encouragement, and support during my long academic journey and the first thirty years of my life. Unfortunately due to the pandemic, I could not fly back to them the minute I finish my doctorate degree, I will definitely share the good news, the happiness and my appreciation with them over video chats.

Chapter 1: Introduction

1.1 Dissertation Introduction

1.1.1 A Brief Background on Elastic Instability

Soft electronics (including stretchable and flexible electronics) and soft actuators have attracted great research interests in recent years [1-4]. They can generally accommodate large, reversible mechanical deformation while maintaining full functionality. Many of these systems, including the ones studied in this dissertation, achieve their repetitive deformability through utilizing the idea of elastic instability. **Figure 1.1** shows the different types of instability that have been studied in the following chapters. Specifically, "buckling" refers to the *sudden* large deformation of a structure when the applied load or displacement exceeds a critical value. There is a dramatic change in the pattern here, as the structure's deformation is small and gradual before the critical load or displacement is reached. From an energy standpoint, buckling is the result of strain energy minimization. The structure deviates from the previous route of deformation and snaps through to the "buckled" route as there is (sometimes remarkably) less strain energy in the latter status.

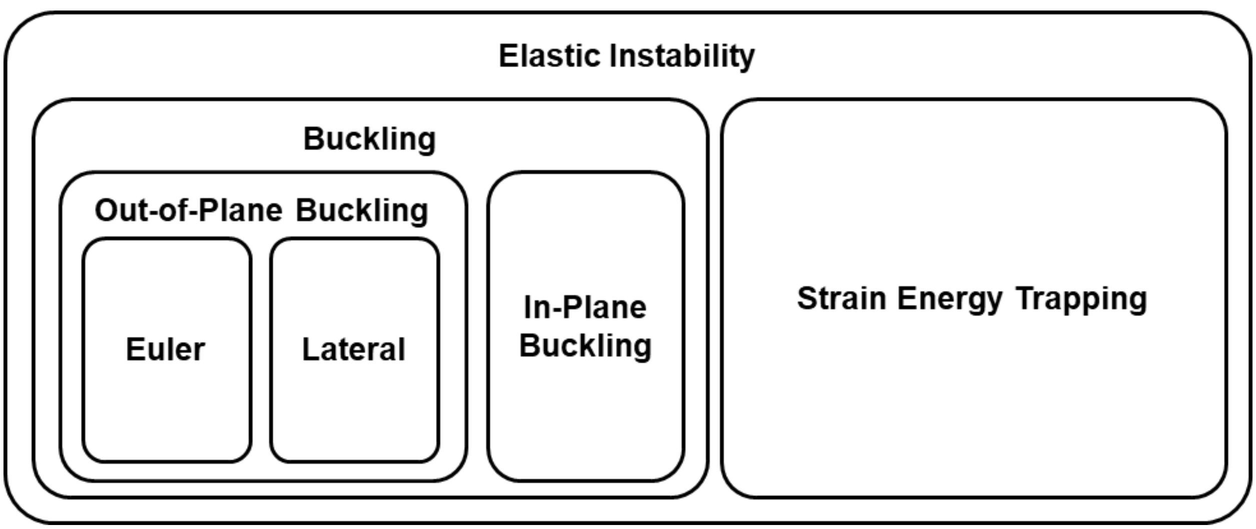

Figure 1.1 *Different categories of elastic instability studied in this dissertation.*

Euler buckling is the most frequently-studied type of buckling phenomenon (**Figure 1.2**). When an applied compression load on a slender column exceeds a critical value, the column will bend, rather than stay in the route of uniaxial compression. This critical load P_{cr} is given as:

$$P_{cr} = \frac{\pi^2 EI}{(kL)^2} \tag{1.1}$$

where EI is the bending stiffness, k is the column effective length factor related to boundary conditions, and L is the length of the column. For a displacement-control problem, the critical buckling strain ε_{cr} (defined as the percentage change in column length at the onset of buckling) is:

$$\varepsilon_{cr} = \frac{P_{cr}}{EA} = \frac{\pi^2 I}{(kL)^2 A} \tag{1.2}$$

where E and A are Young's modulus and cross-sectional area of the column respectively. As an example, for a clamped-clamped ($k = 0.5$) elastic beam ($E = 4$ GPa, Poisson's ratio $\nu = 0.34$) with a rectangular cross-section given in **Fig. 1.2a**, Eqn (1.2) gives the critical buckling strain $\varepsilon_{cr} =$ 0.329%. This agrees very well with results from finite-element analysis (0.331%). When the percentage compression exceeds ε_{cr}, the beam experiences post-buckling deformation, featured by substantial amount of bending and out-of-plane displacement, instead of uniaxial compression (**Fig. 1.2b**). **Fig. 1.2c** shows a comparison in elastic strain energy between post-buckling deformation (red curve) and uniaxial compression without buckling (blue), up to 10% compression. Because the elastic strain energy in the "buckled" route is lower than that in the uniaxial compression route, and the difference of the two grows throughout the deformation process to more than 167 times, the post-buckling deformation is the expected route according to the minimum strain energy principle.

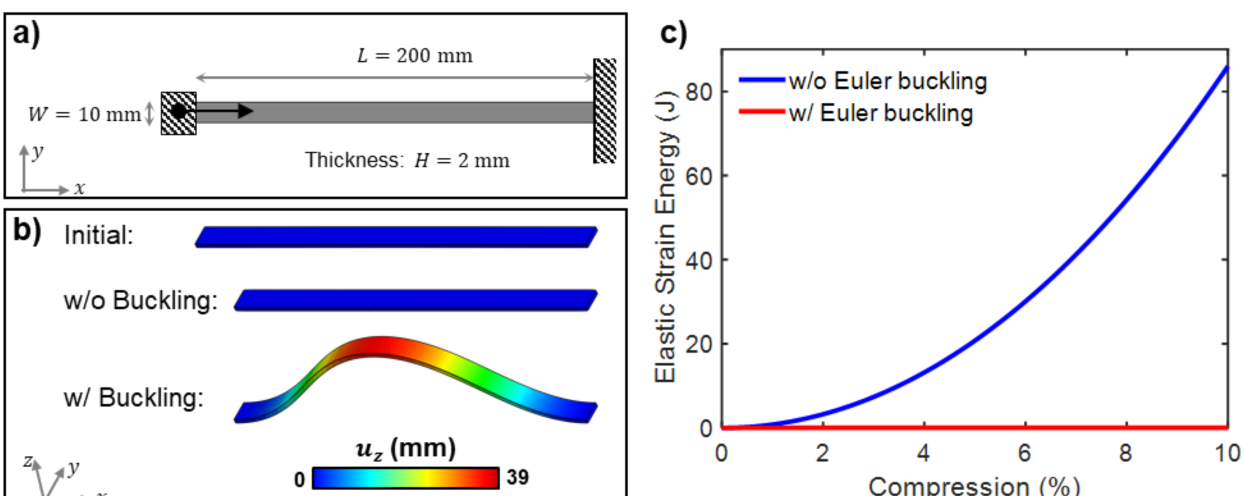

Figure 1.2 *An example of Euler buckling.* ***(a)*** *Illustration of the geometric dimensions and boundary conditions for a beam undergoing Euler buckling.* ***(b)*** *FEA-calculated deformation of the beam under the 10% length compression. Color denotes out-of-plane (z) displacements.* ***(c)*** *Elastic strain energy vs. percentage compression.*

Lateral buckling is another type of buckling, although not as widely known (**Figure 1.3**). For a slender beam (length $L \gg$ width W) with thin cross-section ($W \gg$ thickness H) and clamped-guided boundary condition, applying a *shear* (rather than compressive) load or displacement beyond a critical value along the width (y-direction in **Fig. 1.3a**) direction can cause the beam to buckle out-of-plane (in z-, or "lateral" direction). For the lateral buckling behavior, the critical buckling load P_{cr} is defined as:

$$P_{cr} = C\frac{\sqrt{(EI)(GJ)}}{L^2} \quad \textbf{(1.3)}$$

where $EI = \frac{1}{12}EWH^3$ is the bending stiffness, $GJ = \frac{1}{3}\frac{E}{2(1+\nu)}WH^3$ is the torsional rigidity, and C is a constant depending on boundary conditions and the mode of buckling [5]. Compared with in-plane deformation (without buckling), the post-buckling route features significant out-of-plane deflection and much lower strain energy, and hence is the practical route of deformation (**Fig. 1.3b,c**).

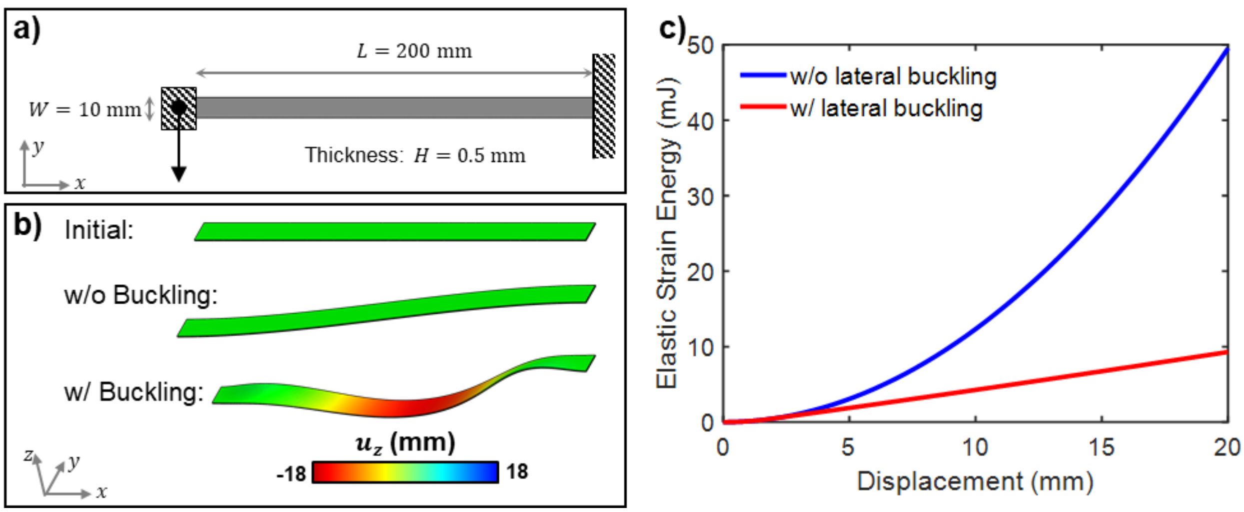

Figure 1.3 *An example of lateral buckling.* ***(a)*** *Illustration of the geometric dimensions and boundary conditions for a beam undergoing lateral buckling.* ***(b)*** *FEA-calculated deformation of the beam with 20 mm displacement in the y-direction. Color denotes out-of-plane (z) displacement.* ***(c)*** *Elastic strain energy vs. displacement.*

The buckling of a complex structure is likely due to the combined effects of the two aforementioned mechanisms. As an example, we analyze the clamped-clamped zigzag structure in **Figure 1.4**. When the right-hand-side end-point is pulled to extend the structure in the x-direction by 100% (**Fig. 1.4a**), the three slender segments in the y-direction may experience both Euler buckling (due to Poisson effect) and lateral buckling (due to the different translation at the two ends of a segment). Their combined effects cause the buckling and out-of-plane deformation of the structure with remarkably lower elastic strain energy than the non-buckling deformation (**Fig. 1.4b,c**). The critical buckling load (or strain) is a function of bending stiffness (EI), torsional rigidity (GJ), the amplitude (L_1), and the span ($\sim L_2$) of the structure [6].

Two geometric variations of this structure lay the foundation of many stretchable electronics systems. The first variation, "curved serpentine", composes of one or multiple periods of the zigzag structure, with some or all of the straight corners and segments changed to fillets and curves for alleviating stress concentration. Curved serpentines can be utilized as deformable interconnects ("bridges") in many electronic systems with "island-bridge" designs, including the systems to be discussed in **Chapter 3**. Another variation, the "Kirigami" design, is used for stretchable electronics systems requiring both high areal coverage and high stretchability. The Kirigami cuts convert an intact sheet densely filled with "hard" functional electronic components into several structurally compliant segments, without wasting much of the surface areas. The strain in each segment remains low even when the entire structure deforms considerably, thanks to the low-strain-energy nature of the buckling/post-buckling route of deformation. The devices to be presented in **Chapter 2** are good examples of this variation.

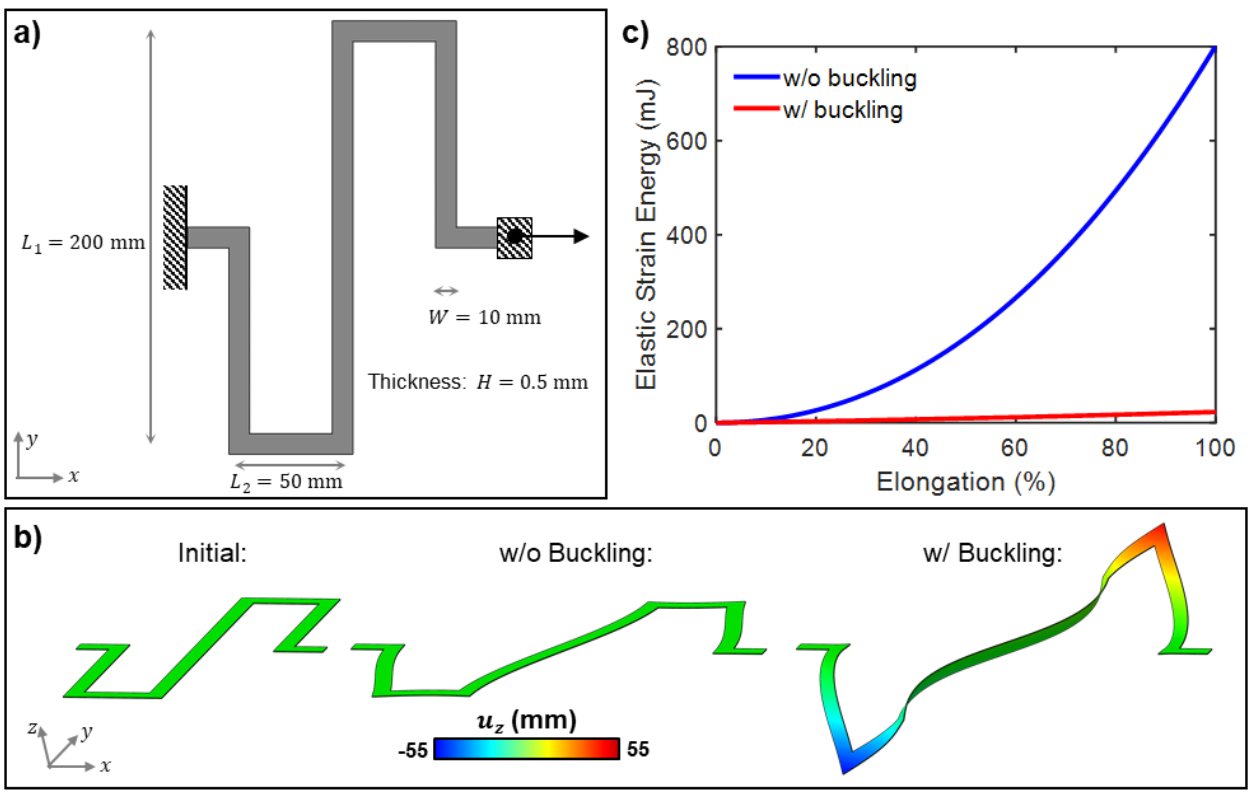

Figure 1.4 *Buckling of a complex structure.* ***(a)*** *Illustration of the geometric dimensions and boundary conditions.* ***(b)*** *FEA-calculated deformation of the structure with 100% elongation in the x-direction. Color denotes displacements in the out-of-plane (z) direction.* ***(c)*** *Elastic strain energy vs. percentage elongation.*

While most people consider buckling as a form of out-of-plane deformation on structures with small thickness ($H \ll W$), it can also occur as the in-plane deformation for thick but narrow segments ($W \ll H$) of structured, elastomeric media. **Figure 1.5a** illustrates a typical example of in-plane segment buckling, similar to that studied by Mullin et. al. [7]. This thick structured elastomeric solid (initial shear modulus $\mu_0 = 1.1$ MPa, bulk modulus $K_0 = 55$ MPa, Neo-Hookean model) featuring an array of periodic holes could be simplified using a plane strain model. When the structured solid is compressed in the y-direction, the relatively narrow segments separating the holes will buckle and bend in the x-y plane to reduce the strain energy, so that the overall structure deviates from uniaxial tension (**Fig. 1.5b**) and eventually forms the shape with alternating voids in **Fig. 1.5c**. It is noteworthy that this route of deformation not only satisfies the minimum strain energy condition (**Fig. 1.5d**), but also gives the structure a negative Poisson's ratio (i.e., auxeticity) when the percentage compression exceeds ~5% (**Fig. 1.5e**). Many mechanical metamaterials use the same or a similar concept to achieve the desirable auxeticity [8-10]. A similar structure is also applied to one of the soft actuators to be presented in **Chapter 4**.

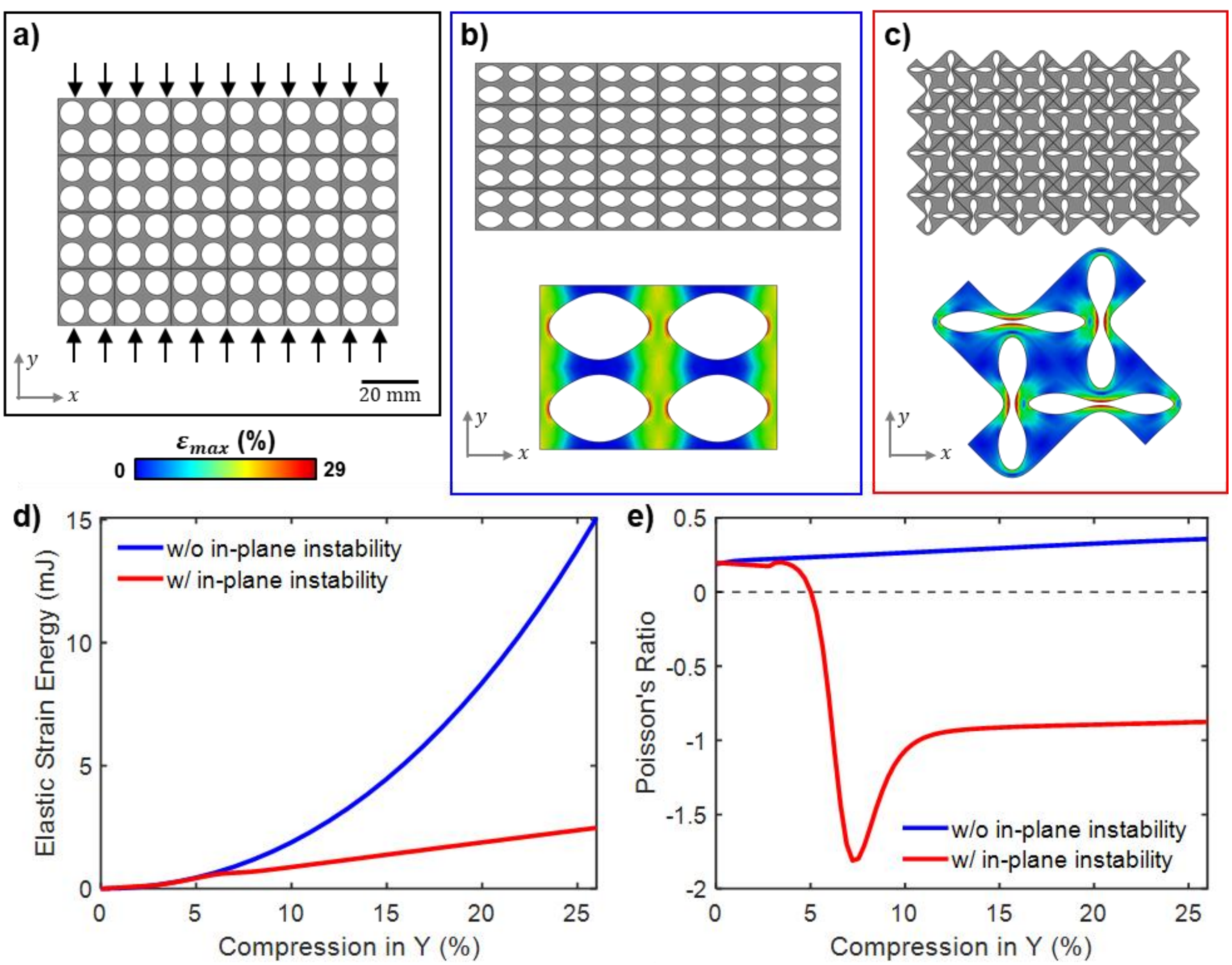

Figure 1.5 *An example of in-plane buckling.* ***(a)*** *Illustration of the geometric dimensions of the*

structure and boundary conditions. ***(b-c)*** *FEA-calculated deformation of the structure in the route (b) without in-plane buckling and (c) with in-plane buckling. Color denotes maximum principal strain on a representative unit in the array with the smallest periodicity.* ***(d)*** *Elastic strain energy and* ***(e)*** *effective Poisson's ratio vs. percentage compression in the y-direction.*

Other than buckling, strain energy trapping is another intriguing type of elastic instability. **Figure 1.6a** shows a classic structure with the energy trapping phenomenon [11]. This thick elastomeric structure (initial shear modulus $\mu_0 = 320$ kPa, bulk modulus $K_0 = 800$ MPa, Neo-Hookean model) is composed of two solid blocks, connected via two narrow slender beams. The top surface of the structure is pushed downwards by 8.45 mm during loading, and then the force is retracted during unloading.

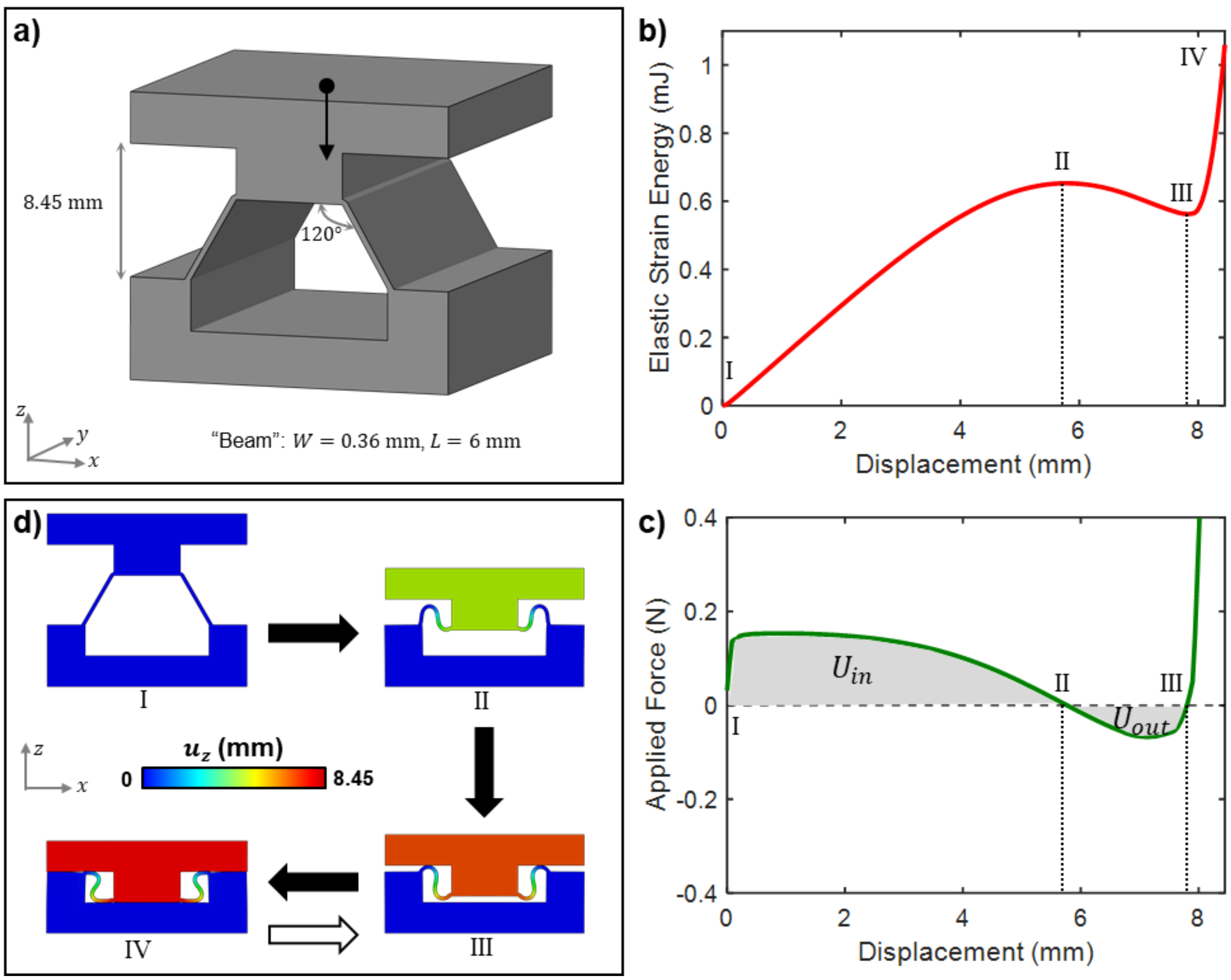

Figure 1.6 *An example of a structure with energy trapping.* ***(a)*** *Illustration of the geometric dimensions of the structure and boundary conditions.* ***(b)*** *Elastic strain energy and* ***(c)*** *applied force vs. displacement in the z-direction.* ***(d)*** *FEA-calculated deformation of the structure at four different stages through the loading/unloading process. Color denotes displacements in the z-*

direction. Solid arrow: loading process. Hollow arrow: unloading process.

Unlike most elastic systems, the strain energy in this system actually decreases during part of the loading process (shown as U_{out}, between II and III in **Fig. 1.6b-d**), and the corresponding applied force is below zero. When the applied force is retracted, the system only recovers to III, a local stable state, instead of fully recovering to I, the initial configuration and global stable state. Most parts of strain energy input U_{in} (during loading between I and II), $\Delta U = U_{in} - U_{out}$ gets "trapped", as this system gets locked in the local stable state. Recently, several bi-stable or multi-stable structures using the principle of strain energy trapping have been reported [11-13]. These structures can be applied in many elastic systems with multiple states of operation, including some of the soft actuators to be presented in **Chapter 4**.

1.1.2 Motivation for Rapid, Low Cost Fabrication

Many stretchable electronics devices adopt the "island-bridge" construct (**Figure 1.7a**), where rigid, functional components reside on "islands", which are linked through structurally compliant interconnects ("bridges"). The stretchable interconnects provides the mechanical deformability for the overall device, while the functional components remain almost strain-free. Using this scheme, materials for "hard" electronics (e.g., metal pads and interconnects, high-performance commercial chips and semiconductors, standard polymer insulators) can still be used, and devices can be fabricated in lithography-based processes (**Fig. 1.7b**). The typical fabrication processes requires at least two photomasks. The metal pads and interconnects (gold, copper or aluminum) are patterned with the first mask through a lift-off or standard wet etching process. Then the entire underlying structure layer made of insulating materials (e.g., polyimide or parylene) is defined by the second mask, via dry etching through the entire thickness. In many devices, there is also an insulating cover layer on top, patterned by a third mask through a dry etching process, to protect interconnects while exposing pads for connections with functional components. Additional photomasks will be needed for devices with multiple layers of metal traces and more complex structures.

While lithography-based fabrication is effective, high-yield and consistent in the industrial large scale manufacturing of MEMS and IC devices, it is hardly an ideal approach for stretchable electronics, especially when only a small batch of samples are needed in the research stage for university labs. Cleanroom and specialty equipment (mask aligners, reactive ion etch stations) accesses are expensive and often billed by the minute. The lithography-based processes may also be too time-consuming, due to the long turn-around time for photomask design, fabrication and shipping, and the prolonged dry etching steps for defining structure and cover layers. Worse still, stretchable electronics devices suffer from the yield issues during lithography-based fabrication. Because the typical sizes of these devices (~10 cm^2) are significantly larger than the typical MEMS or IC chips (~0.1 to 1 cm^2), much fewer samples can fit into one wafer. As shown in **Fig. 1.7c**, these large samples are much more likely to be compromised and hence the much lower yields, even when subject to the same amount and size of contaminated regions from multi-mask fabrication processes. Therefore, it will be very desirable to have an alternative, rapid, low-cost fabrication approach for stretchable electronics, satisfying the research needs in university labs.

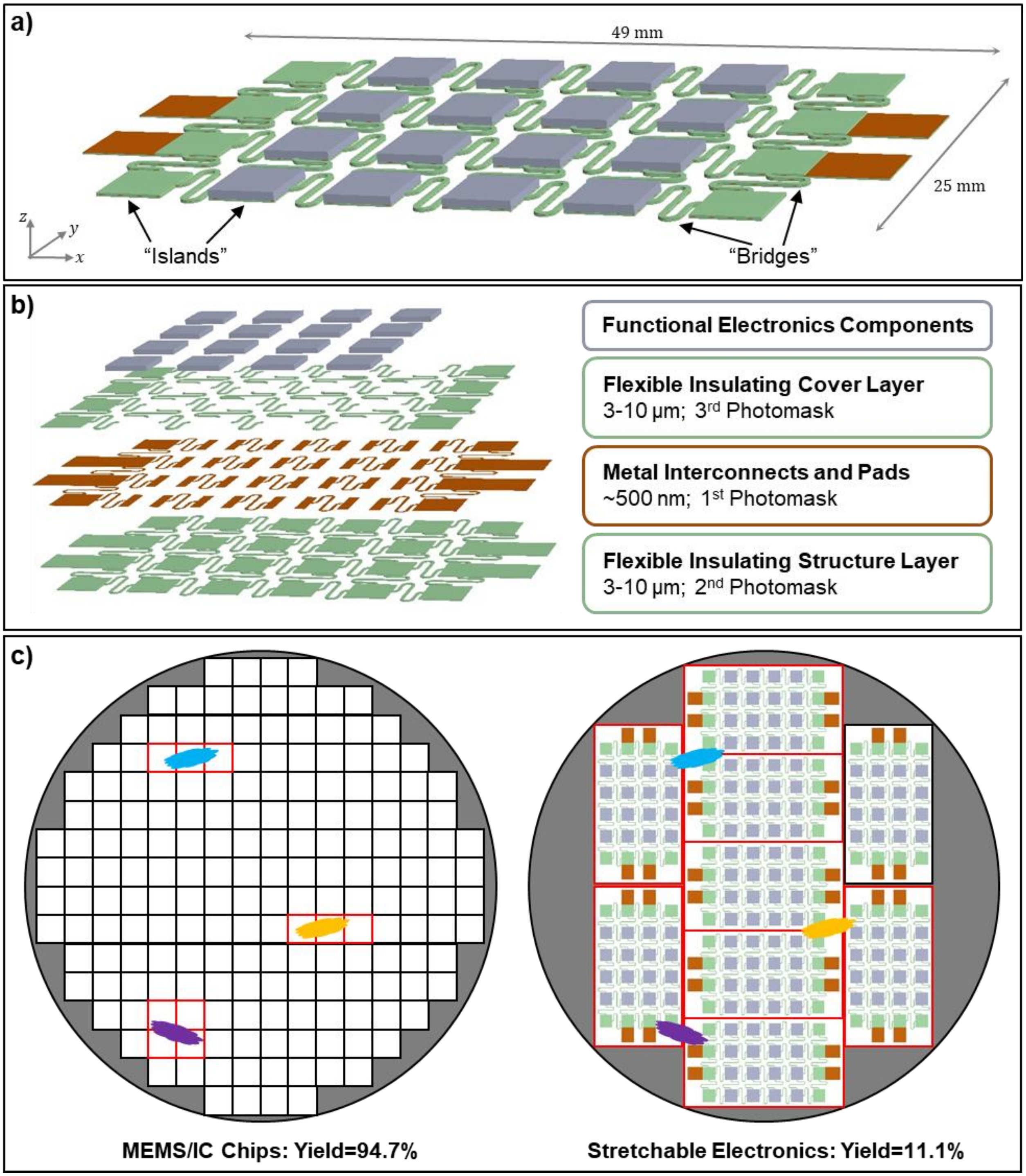

Figure 1.7 ***(a)*** *Illustration of a typical stretchable electronics device with "island-bridge" construct.* ***(b)*** *Layer-by-layer illustration of structure of the device in (a).* ***(c)*** *Comparison of yield between MEMS/IC chips and stretchable electronics devices using photolithography-based processes. The gray circles represent a 6-inch wafer. The stained areas denotes contaminated regions from the multi-mask process. White areas with red outlines denote compromised devices.*

In the last two years, magnetically powered untethered soft actuators have emerged as a new comer with great potentials (**Figure 1.8**) [14-16]. Unlike previous counterparts made of shape memory polymers, hydrogels, or liquid crystal elastomers driven by prolonged physical or chemical processes, the magnetically powered devices can complete an actuation cycle within a fraction of a second. However, the reported actuators require complex or highly-specialized equipment for fabrication, such as a direction-specific 3D printer with accurately timed magnetization function (for **Fig. 1.8a**), a special lithography platform with on-site magnetization (for **Fig. 1.8b**), or cleanroom equipment for electron beam lithography, metal evaporation and reactive ion etching (for **Fig. 1.8c**). In our study, we aim to explore effective fabrication options for building magnetically powered soft actuators, using only easily accessible experimental setups and low-cost, commercially available materials.

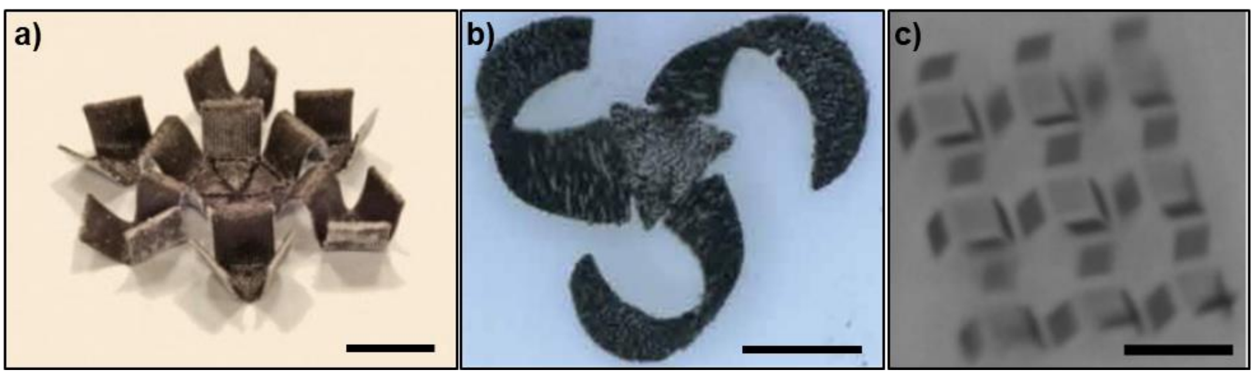

Figure 1.8 *Reported magnetically powered soft actuators with different length scales:* ***(a)*** *centimeter scale* [15], ***(b)*** *millimeter scale* [16], *and* ***(c)*** *micron scale* [14]. *Scale bars: 10 mm in (a), 1 mm in (b), and 30 μm in (c).*

1.2 Dissertation Overview

This dissertation has two common themes across different chapters, "rapid, low-cost fabrication" and "elastic instability". In the following three chapters, each chapter describes one fabrication approach for soft electronics or soft actuators, and all devices can sustain large deformation, due to the use of elastic instability.

Chapter 2 introduces a construct inspired by Kirigami for highly deformable micro-supercapacitor patches with high areal coverages of electrode and electrolyte materials. These patches are fabricated in simple and efficient steps by laser assisted graphitic conversion and cutting, using the different laser power and scanning speed settings on a commercially available laser cutter. Because the Kirigami cuts significantly increase structural compliance, segments in the patches can buckle, rotate, bend and twist to accommodate large overall deformations with only a small strain (<3%) in active electrode areas. Electrochemical testing results have proved that electrical and electrochemical performances are preserved under large deformations.

While the fabrication method in Chapter 2 applies to a specific material (laser-induced-graphene), **Chapter 3** provides a time- and cost-effective fabrication solution for general stretchable electronics devices with "island-bridge" constructs, without using photomasks. Instead of lithography-related equipment, a low-cost commercially available vinyl cutter is used for defining patterns. By adjusting the force on the blade, metal interconnects and pads can be patterned via the "tunnel cuts", and the flexible overall structure defined via the "through cuts". The capabilities of the proposed method is shown by two devices, a skin-mounted breath sensing module and a water-resistant, omni-directionally stretchable supercapacitor array. These devices can reversibly accommodate large deformations through buckling and post-buckling instability.

Chapter 4 reports a class of magnetically powered, untethered soft actuators with a bioinspired flesh-and-bone construct. This construct not only is the key for fast actuation and compliant impact-resistant mechanics, it also renders simple fabrication using only generic FDM 3D printers and commercial off-the-shelf neodymium magnets and silicone elastomers. Through diverse designs, some using the concept of elastic instability, actuators with various shapes of elastomeric "flesh" and different placements of magnetic "bones" can complete several distinct types of actuations, including auxetic expansion and shrinking, out-of-plane transformations, transition among multiple stable states, and manipulation of small objects.

Finally, **Chapter 5** summarizes the conclusions of this dissertation and proposes some future research directions and potential applications of the current study.

References of Chapter 1

[1] W. Gao, H. Ota, D. Kiriya, K. Takei, and A. Javey, "Flexible electronics toward wearable sensing," *Accounts of chemical research,* vol. 52, no. 3, pp. 523-533, 2019.

[2] Y. Liu, M. Pharr, and G. A. Salvatore, "Lab-on-skin: a review of flexible and stretchable electronics for wearable health monitoring," *ACS Nano,* vol. 11, no. 10, pp. 9614-9635, 2017.

[3] J. A. Rogers, T. Someya, and Y. Huang, "Materials and mechanics for stretchable electronics," *Science,* vol. 327, no. 5973, pp. 1603-1607, 2010.

[4] D. Rus and M. T. Tolley, "Design, fabrication and control of soft robots," *Nature,* vol. 521, no. 7553, pp. 467-475, 2015.

[5] Y. Su *et al.*, "Postbuckling analysis and its application to stretchable electronics," *Journal of the Mechanics and Physics of Solids,* vol. 60, no. 3, pp. 487-508, 2012.

[6] Y. Zhang *et al.*, "Buckling in serpentine microstructures and applications in elastomer-supported ultra-stretchable electronics with high areal coverage," *Soft Matter,* vol. 9, no. 33, pp. 8062-8070, 2013.

[7] T. Mullin, S. Deschanel, K. Bertoldi, and M. C. Boyce, "Pattern transformation triggered by deformation," *Physical Review Letters,* vol. 99, no. 8, p. 084301, 2007.

[8] K. Bertoldi, P. M. Reis, S. Willshaw, and T. Mullin, "Negative Poisson's ratio behavior induced by an elastic instability," *Advanced Materials,* vol. 22, no. 3, pp. 361-366, 2010.

[9] J. T. Overvelde, S. Shan, and K. Bertoldi, "Compaction through buckling in 2D periodic, soft and porous structures: effect of pore shape," *Advanced Materials,* vol. 24, no. 17, pp. 2337-2342, 2012.

[10] D. Yang *et al.*, "Buckling of elastomeric beams enables actuation of soft machines," *Advanced Materials,* vol. 27, no. 41, pp. 6323-6327, 2015.

[11] S. Shan *et al.*, "Multistable architected materials for trapping elastic strain energy," *Advanced Materials,* vol. 27, no. 29, pp. 4296-4301, 2015.

[12] J. Hua, H. Lei, Z. Zhang, C. Gao, and D. Fang, "Multistable cylindrical mechanical metastructures: theoretical and experimental studies," *Journal of Applied Mechanics,* vol. 86, no. 7, 2019.

[13] F. Pan, Y. Li, Z. Li, J. Yang, B. Liu, and Y. Chen, "3D pixel mechanical metamaterials," *Advanced Materials,* vol. 31, no. 25, p. 1900548, 2019.

[14] J. Cui *et al.*, "Nanomagnetic encoding of shape-morphing micromachines," *Nature,* vol. 575, no. 7781, pp. 164-168, 2019.

[15] Y. Kim, H. Yuk, R. Zhao, S. A. Chester, and X. Zhao, "Printing ferromagnetic domains for untethered fast-transforming soft materials," *Nature,* vol. 558, no. 7709, pp. 274-279, 2018.

[16] T. Xu, J. Zhang, M. Salehizadeh, O. Onaizah, and E. Diller, "Millimeter-scale flexible robots with programmable three-dimensional magnetization and motions," *Science Robotics,* vol. 4, no. 29, 2019.

Chapter 2: Kirigami-Inspired, Highly Stretchable Micro-Supercapacitor Patches Fabricated by Laser Conversion and Cutting

2.1 Introduction

In recent years, stretchable electronics systems have drawn widespread attentions in research and commercialization [1-5]. These systems are mechanically compliant to maintain their electronic performances even when subject to large twisting, bending, and stretching, in applications that require intimate and conformal contacts with curvilinear biological tissues and organs. Reported applications range from epidermal health monitors [6, 7] to implantable optoelectronics platforms [4], and from wearable energy harvesters [8, 9] to artificial skin-like electronics [10]. Although the aforementioned systems are soft and deformable in the system-level, the functional electronic components in many of these systems are made of hard (e.g., conductive metals) or even brittle materials (e.g., silicon or III-IV semiconductors and their oxides) [1]. As such, the overall desirable mechanics are results of rationally designed constructs, which can provide considerable structural deformability without adding high stresses on the functional parts. One commonly used construct is the “Island-Bridge” model (**Fig. 2.1a**), where rigid, functional electronic components (i.e., the “islands”) with side length L_i are separated by spacing L_s among them, and joined by compliant, deformable interconnects (i.e., the “bridges”) to sustain uniaxial stretching deformation by out-of-plane or in-plane unraveling [3, 6, 7, 10-15]. In this system, the areal coverage of functional components η can be calculated as $\eta = L_i/(L_i + L_s)$, and the system-level stretchability ε_{sys} (defined as the maximum elongation before electronic or mechanical failure) is related to the stretchability of interconnects ε_{int} by:

$$\varepsilon_{sys} = \varepsilon_{int} \cdot (1 - \eta) \quad \textbf{(2.1)}$$

Since the stretchability of the system ε_{sys} and areal coverage η are negatively correlated in the “Island-Bridge” model, stretchable electronic systems with this construct (shown as triangles in **Fig. 2.1b**) can only achieve high stretchability at the cost of relatively low areal coverage, or vice versa, high areal coverage but limited stretchability. Some other stretchable systems adopt the “Accordion” construct (**Fig. 2.1c**) [16-20]. In these systems, thin-film electronics are initially wrinkled due to the release of pre-strain in elastomeric substrates. As the system gets stretched within a limit, the wrinkled films can be flattened out without much axial deformation, therefore providing system-level stretchability. With good layouts, this construct (denoted by diamonds in **Fig. 2.1b**) can ideally boast 100% areal-coverage, yet the stretchability is limited by the (often quite small) failure strain of the electronics material to be below ~100% of the original length. For stretchable micro-supercapacitors, previously demonstrated works usually adopt one of the two constructs, and consequently show either insufficient stretchability [18, 20] or relatively low areal coverage[13]. Recently, a new class of construct, inspired by the traditional Japanese paper-cutting craftwork (or more commonly known as "Kirigami", **Fig. 2.1d**), has been proposed. In this construct, an intact patch is separated into several deformable segments by rationally designed cuts. Several Kirigami-inspired electronic systems have been reported, including solar cells with tracking functions [21], implantable bio probes [22], stretchable graphene transistors [23], diffraction gratings for LIDAR/LADAR [24], and piezoelectric strain sensors [25], etc. The Kirigami construct has also been adopted in stretchable supercapacitors, with reported stretchabilities ranging from less than fifty percent to over several hundred percent [26-28]. In this chapter, we present stretchable micro-supercapacitor patches adopting well-designed "Kirigami" constructs. As a result, they enjoy the benefits of both "Island-Bridge" and "Accordion" models: they have high areal coverage (76.2%, 62.8%, and 67.1% for three different designs) of functional components and can sustain more than 282.5% elongation with negligible changes in supercapacitor performances. The high areal coverages and high stretchability both come from the design of Kirigami constructs: the deformable segments in the construct, made of functional components themselves, can rotate, bend and twist out-of-plane to unravel and accommodate significant system-level uniaxial stretching. Although the total elongation of the system may be large, the strains in each segments are small to ensure almost unaffected electronic performances. Compared with previously reported Kirigami-inspired supercapacitors [26-28], our stretchable micro-supercapacitor patches can be conveniently fabricated in simple and efficient steps by well-controlled laser graphitic conversion and cutting, with the use of one single commercial CO_2 laser source. In addition, while other Kirigami-inspired supercapacitors can typically sustain a working voltage below ~1V [26-28], our stretchable micro-supercapacitor patches can support 10V or higher by flexibly engineering the layout of electrodes and Kirigami cuts to enable various electrical connections among the array of capacitors in one patch.

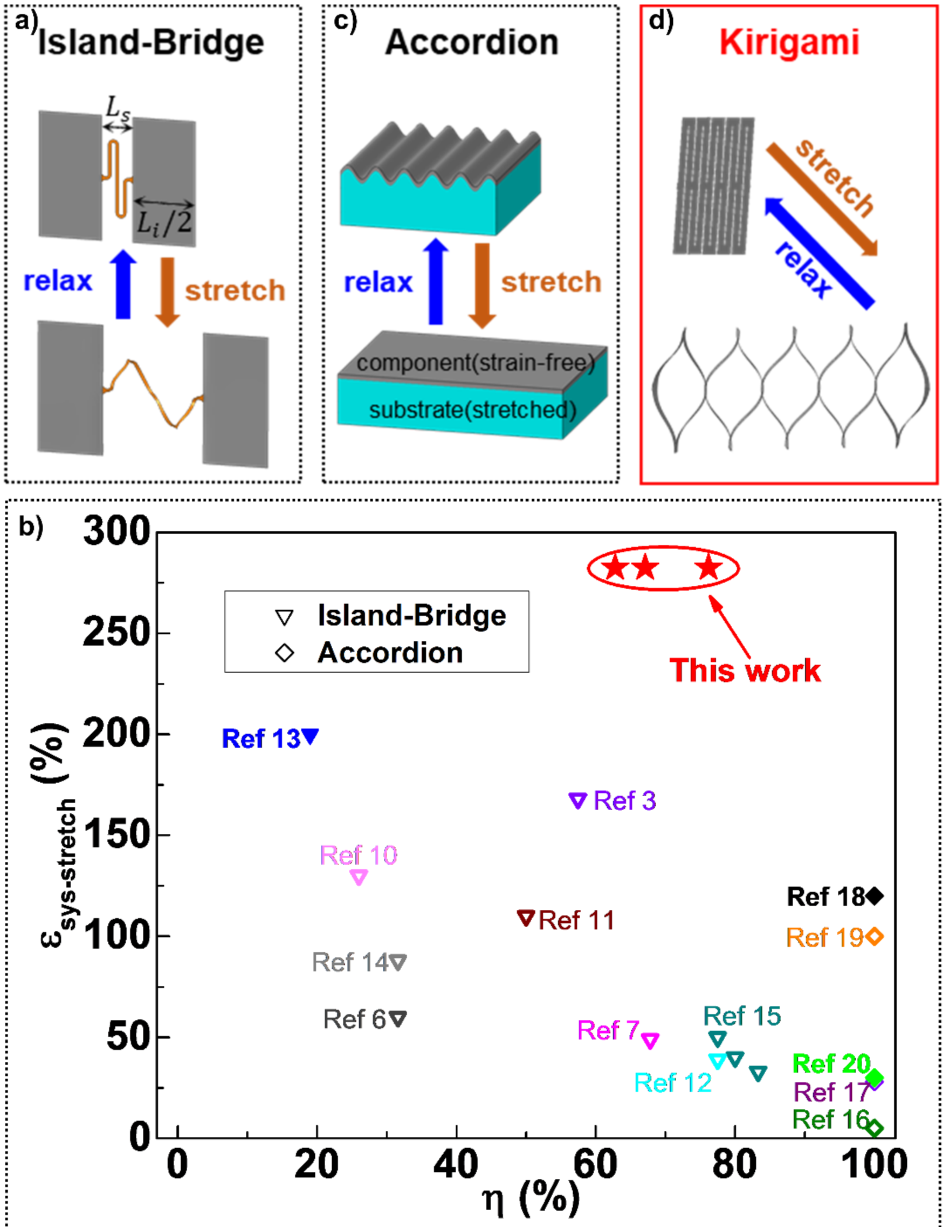

Figure 2.1 *Schematic illustrations of three classes of construct designs employed in stretchable electronics systems.* ***(a)*** *The Island-Bridge construct.* ***(b)*** *System-level stretchability vs. areal coverage of functional components for stretchable systems reported in this chapter (highlighted in red) and in other works. Solid markers denote stretchable supercapacitors. Hollow markers denote other electronic systems.* ***(c)*** *The Accordion construct.* ***(d)*** *The Kirigami-inspired construct used in this study.*

2.2 Results and Discussion

2.2.1 Graphitic Conversion and Cutting

Previous studies have shown that the heat generated from CO_2 laser can convert commercial polyimide films to conductive graphitic structures (laser-induced graphene, or "LIG") [29]. Here, we utilize different heating levels from the laser, in order to: 1) set up an appropriate range for the occurrence of graphitic conversion; and 2) explore the phenomena when the heating level is high enough to cut through the thin polymer films. For a commercial CO_2 laser source (*Universal Laser Systems*, wavelength = 10.6 μm), changing the heating level is done through tuning the power of the laser source (unit: W, or J/s) and the scanning speed of the laser head (unit: mm/s). The heating level can be quantified by the amount of heat injected into a unit length on the polyimide film along the scanning direction (often referred to as "linear heat density" or "LHD", unit: J/mm), which can be calculated from the laser power divided by the scanning speed. **Figure 2.2a** summarizes the reactions to a commercial polyimide film (Kapton, Dupont, thickness = 125 μm) when it is irradiated by the CO_2 laser, with different combinations of power and scanning speed. In this plot, points on the same straight line (with 0 intercept) correspond to combinations that produce equal linear heat densities, while lines of different inverse-slopes represent conditions with different heating levels from the laser source. When the injected heat is insufficient for the photothermal graphitic conversion process to take place (LHD less than roughly 0.05 J/mm, as shown by blue dots in **Fig. 2.2a** and in **Fig. 2.3a**), no obvious change on the polyimide film can be observed. Beyond this threshold, the heat generated from the scanning laser converts polyimide near the Kapton film surface to graphitic networks (**Fig. 2.2b** and **Figs. 2.3b-h**, green dots in **Fig. 2.2a**). If the heat output from the laser is even higher than a second threshold (LHD greater than ~ 0.37 J/mm), the polyimide film is carbonized throughout its thickness so that a continuous cutting slot can be formed (**Fig. 2.2c**, red dots in **Fig. 2.2a**). The generation of both graphitic patterns and cutting slots are necessary steps in the fabrication of our stretchable micro-supercapacitor patches, as elaborated on in following paragraphs. Scanning electron microscopy (SEM) images in **Figs. 2.2d** and **2.2e** reveal the microscale structures of the highly porous, interconnected graphitic patterns for porous graphitic networks (green dots in **Fig. 2.2a**), and an optical image of a laser-cut film is shown in **Fig. 2.2f** (red dots in **Fig. 2.2a**).

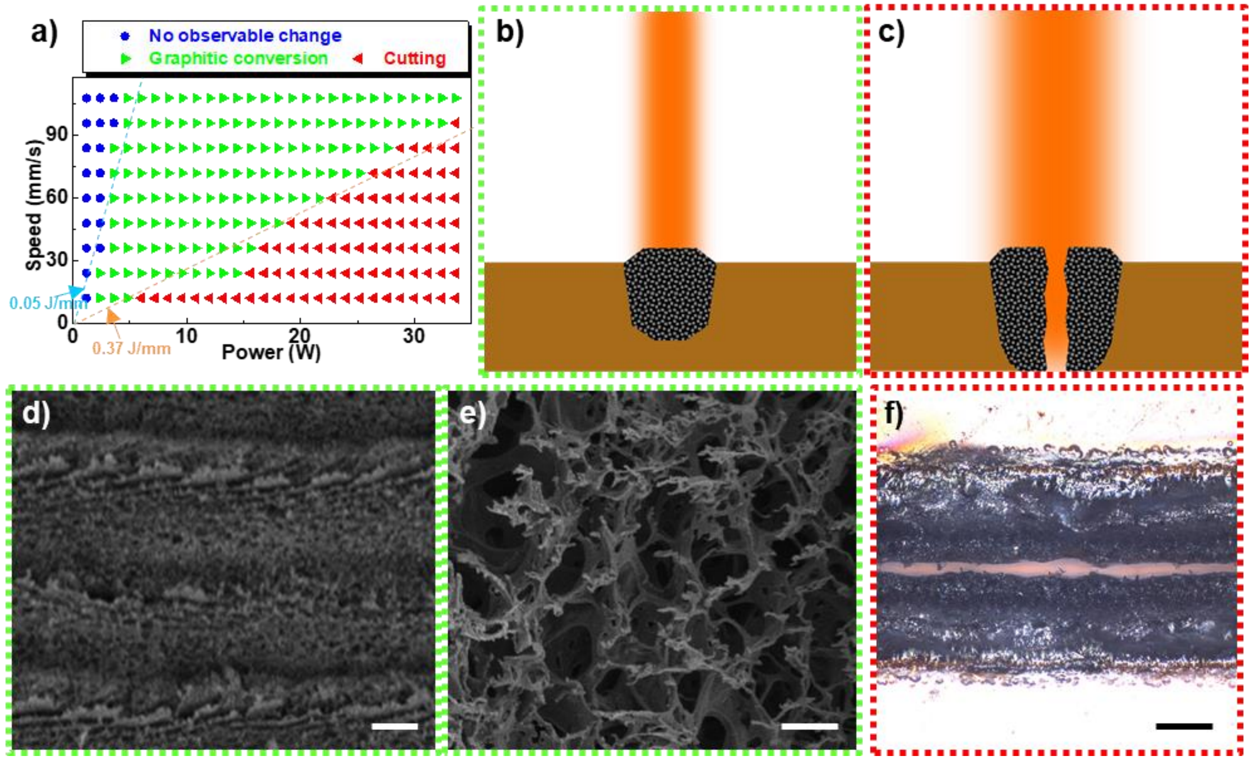

Figure 2.2 *Laser assisted graphitic conversion and cutting.* ***(a)*** *With different combinations of laser power and scanning speed, apparent change (blue dots), graphitic conversion (green dots) or cutting (red dots) can be observed in the polyimide film. The two dash lines denote two threshold linear heat densities.* ***(b)*** *Schematic illustration of graphitic conversion.* ***(c)*** *Schematic illustration of laser cutting.* ***(d-e)*** *SEM images featuring microscopic structures resulting from graphitic conversion.* ***(f)*** *Optical image of a cutting slot resulting from laser irradiation. Scale bars: 20 μm in (d); 2 μm in (e); 100 μm in (f).*

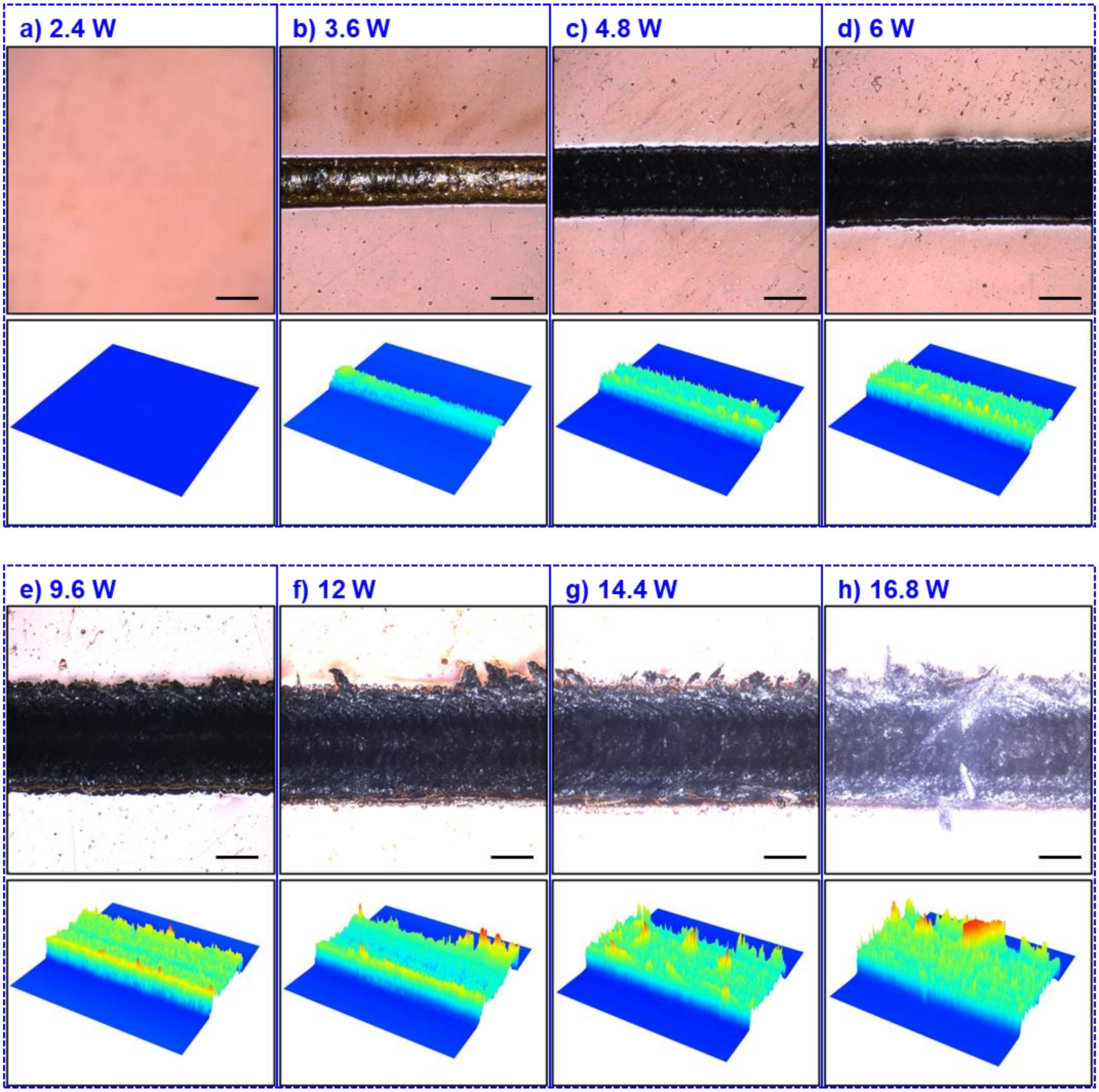

Figure 2.3 ***(a-h)*** *Top view optical (top) and 3D reconstruction images (bottom) of polyimide film surface after being irradiated by laser with different power levels. The scanning speed of laser head is fixed at 60 mm/s. Scale bars: 100 μm. The color in 3D reconstruction images denotes relative height above the top surface of the polyimide film.*

While experimenting different combinations of laser power and scanning speed exhaustively helps define the boundaries among the three "phases" (i.e., no observable change, graphitic conversion, and cutting), we need to obtain the optimal conditions for graphitic conversion and cutting before using them for device fabrication. In following experiments, we tune the linear heat density by changing laser power, while fixing the scanning speed as 60 mm/s, a reasonable value chosen for easy operation. First, we optimize the conditions of graphitic conversion towards obtaining high quality electrode materials for supercapacitors: graphitic patterns with abundant micro-scale pores, low electrical resistance and good mechanical stability. Optical and 3D reconstruction images in **Fig. 2.3b-h** show the traces made of graphitic networks resulting from ONE laser scan along a straight line at different powers. With laser power increased from 3.6 W to 9.6 W (LHD from 0.06 J/mm to 0.16 J/mm), larger volumes in the film are affected and converted by the heat, so that the resulting porous graphitic trace gets wider and thicker (**Fig. 2.3b-e**). The trace generated at 9.6 W features desirable width and height, and a relatively smooth surface on mesoscale. When the power of the laser is too high (e.g., ~14.4 W or higher), the resulting trace consists of many laminar pieces sticking outwards, likely due to sudden overheating from the intense laser irradiation (**Fig. 2.3f-i**). Because these laminae can be peeled off easily, the overall mechanical robustness of the graphitic pattern is undesirable. These qualitative observations from optical and 3D reconstruction images help us effectively narrow down the window of optimal graphitic conversion conditions.

For a more detailed and quantitative study, we produce many graphitic resistor samples with the same pattern design (6 mm by 60 mm, rectangular strip) at laser powers ranging from 3.6 W to 13.2 W, and measure the sheet resistance of each sample using a four-point probe. The top surface and cross-section of these samples are also characterized by SEM, as shown in **Figure 2.4**. When the laser power is less than optimal (e.g., at 4.8 W or 7.2 W), the sheet resistance of the generated pattern is relatively high. This is because the heat from laser is not sufficient to reach and convert enough depth of the polyimide film material (**Fig. 2.4b-c**). At the optimal laser power of 9.6 W (LHD = 0.16J/mm), the sheet resistance reaches a minimum at 9.1 Ω/square. Cross-section SEM (**Fig. 2.4d**) shows that the boundary between the converted graphitic region (thickness ~100 μm) and remaining polyimide is desirably smooth and uniform. It is noteworthy that sheet resistance does not further decrease at conditions with higher laser powers, despite that more materials in the polyimide film become converted (**Fig. 2.4a**). This is likely because the excessive heat from laser can both convert deeper regions in the polyimide film (therefore, decrease resistance) and burn out carbonized graphitic structures (therefore, increase resistance) at the same time. As a result, the overall resistance remains almost constant. However, the samples obtained at higher laser powers (e.g., 12 W and 13.2 W) have poor mechanical stability. SEM images show that the jagged boundary between converted graphitic region and remaining polyimide is vulnerable to fracture (**Fig. 2.4e**), and the graphitic networks are already cracked in some cases and peeled off with only tiny perturbation (**Fig. 2.4f**). Based on the above analyses, the combination of power ~9.6 W and speed ~60 mm/s (LHD = 0.16 J/mm) is used as the optimized condition for producing electrode materials.

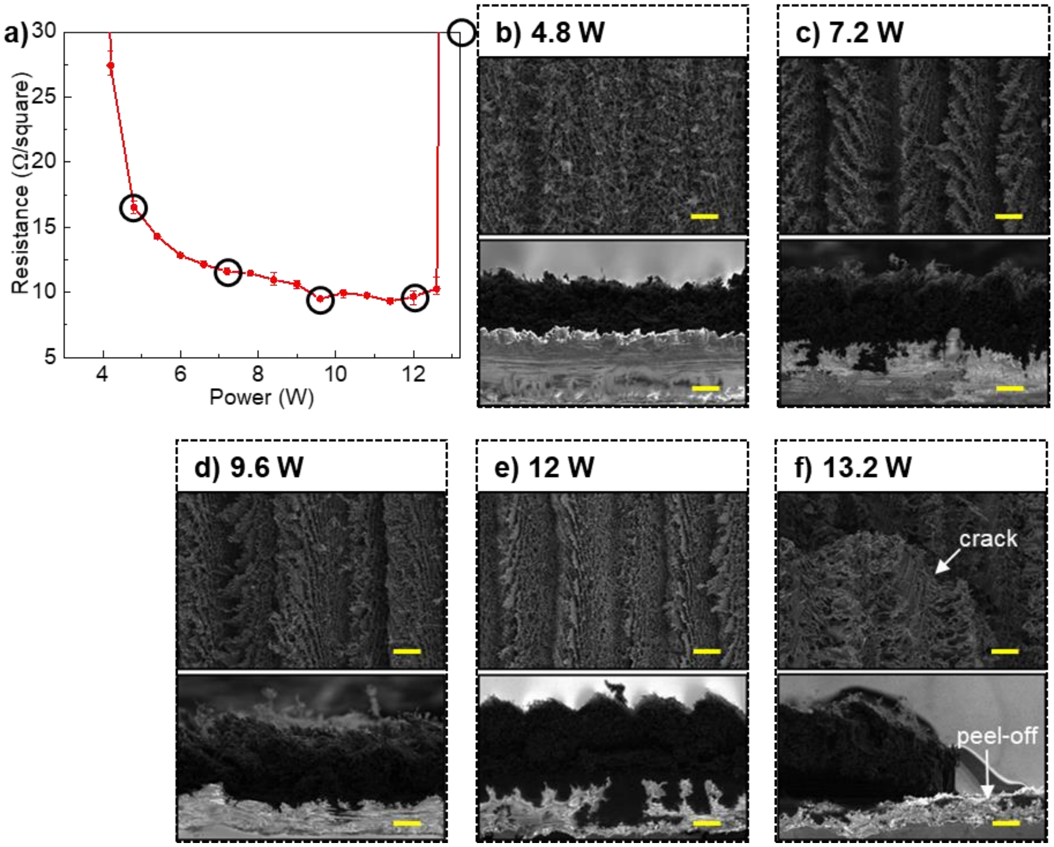

Figure 2.4 *(**a**) Sheet resistances and (**b-f**) SEM images (top: top view; bottom: cross-sectional view) of graphitic network structures obtained at different laser power levels. The scanning speed is fixed at 60 mm/s. Scale bars: 25 μm.*

Our goal for optimizing cutting is to find the condition that guarantees the formation of continuous cut slots while affecting the smallest possible neighboring regions (**Figure 2.5**). When the scanning speed is fixed at 60 mm/s, continuous cutting slots only start to form when laser power reaches 22.8 W (LHD = 0.38 J/mm). The widths of the cutting slot and the total carbonized regions are 25.2 μm and 362.1μm, respectively (**Fig. 2.5d**). Since further increasing the laser power (and consequently, heat output from laser) will undesirably increase the widths of total carbonized regions (**Fig. 2.5d-f**), we choose laser power 22.8 W (along with speed 60 mm/s) as the optimized condition for defining the Kirigami cutting slots.

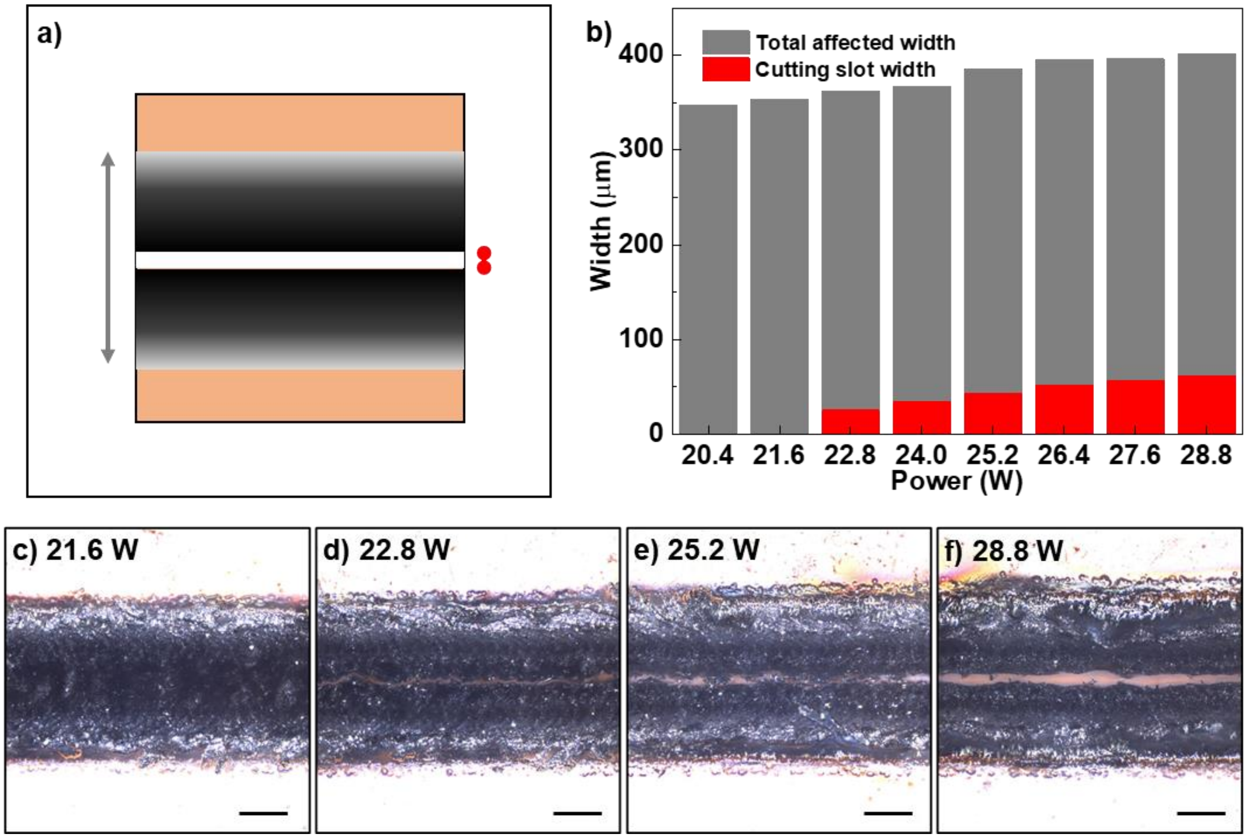

Figure 2.5 ***(a)*** *Schematic illustration of a typical cutting slot structure, featuring the total heat affected region (gray arrow) and the cutting slot (red arrow).* ***(b)*** *The widths of total heat affected region and cutting slot for different laser power levels.* ***(c-f)*** *Top view optical images of polyimide film surface after being irradiated by laser with different power levels. The scanning speed of laser head is fixed at 60 mm/s. Scale bars: 100 μm.*

2.2.2 Device Fabrication, Performance Testing and Demonstration

After the process optimization, graphitic conversion and cutting are adopted as key steps for the fabrication of our stretchable micro-supercapacitor patches (abbreviated as “SMSP” in following paragraphs). First, porous graphitic electrode patterns in the SMSP are generated by irradiating a commercial polyimide sheet (Kapton, Dupont, thickness = 125 μm) with power and scanning speed set as 9.6 W and 60 mm/s, respectively. Then, the laser power is increased to 22.8 W (while maintaining the same scanning speed) to define the Kirigami cutting slots. Some cutting slots constitute the external boundaries of a patch, so that the patch of pre-designed dimensions can be released from a larger Kapton sheet. Other slots (i.e., cutting slots inside the patch) can significantly increases the compliance of the overall patch structure. Finally, a polymer-based electrolyte solution (made from mixing 1 gram of polyvinyl alcohol, 1 gram of phosphoric acid, and 12 gram of deionized water) is applied to selected regions on the patch to make the patch a functional supercapacitor array. **Figures 2.6a-b** illustrate the geometric details of a representative SMSP in both exploded 3D view and top view, with the cutting slots (red), the porous graphitic electrodes (black), and the locations to apply electrolyte (semi-transparent blue) highlighted by different colors. The areal coverage of functional components (i.e., combined regions of electrodes and electrolyte) of this SMSP design is 76.2%. The overall size of the patch is 36.5 mm by 28 mm, which is only slightly larger than a US quarter (**Fig. 2.6e**). The pre-designed alternating, offset Kirigami cuts transforms the polyimide sheet into five deformable units that are mechanically (and electrically) joined together. Each deformable unit consists of two equivalent parallel plate-like capacitors joined in series. In total, the SMSP has ten equivalent capacitors of the same design in series connection.

We perform standard cyclic voltammetry (CV) and galvanostatic charge/discharge (GCD) tests on our SMSP with an electrochemical workstation (Gamry Reference 600), when the SMSP is in its initial, undeformed configuration (**Figs. 2.6c-d**). When the scan rate is set as 100 mV/s, the SMSP yields areal specific capacitance 2.273 mF/cm^2. As expected, this value is comparable to that reported in Ref. 29, where similar laser induced graphitic networks were also used as electrodes [29]. The energy density and power density are calculated as 0.32 μWh/cm^2 and 11.4 μW/cm^2, respectively. At other scan rates ranging from 20 mV/s to 500 mV/s, areal specific capacitances from 1.125 mF/cm^2 (at 500 mV/s) to 3.654 mF/cm^2 (at 20 mV/s) are obtained. The capacitance performance of the device can also be confirmed by the various GCD curves in **Fig. 2.6d**, corresponding to different charge/discharge current settings.

In order to visually demonstrate the very high deformability of our SMSP, we stretch and twist the SMSP (**Fig. 2.6g**) and an intact polyimide patch (with no cuts) of the same size (**Fig. 2.6f**). As we expect, the SMSP can be stretched to three times of its initial length and twisted by ~90 degrees easily, whereas the intact Kapton sheet can only be twisted by less than 30 degree with negligible increase in length, even when much higher force and torque are applied. This comparison qualitatively confirms our expectation that introducing pre-designed Kirigami cuts can increase the deformability of polyimide patches significantly.

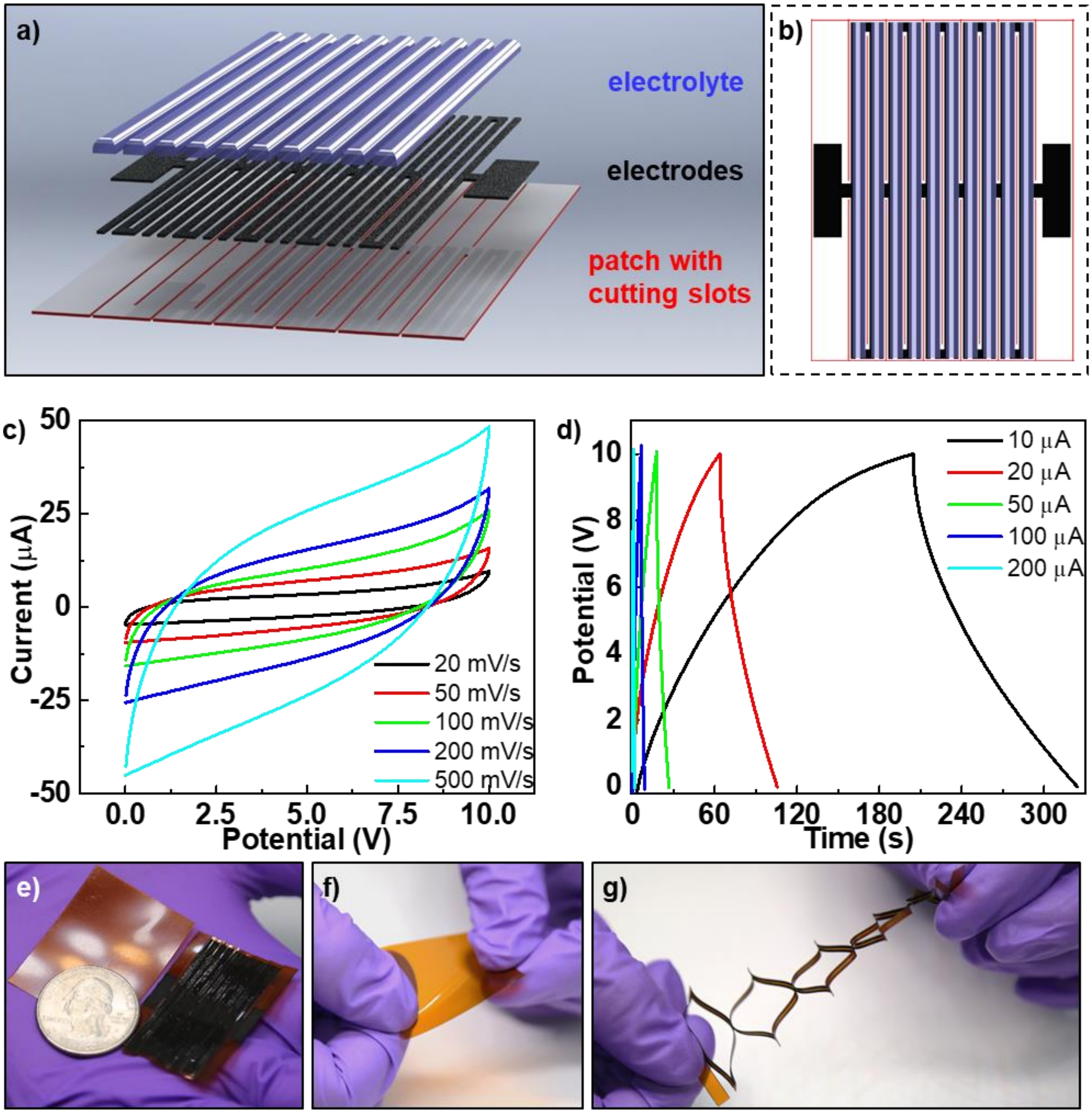

Figure 2.6 *Schematics, performances, and demonstration of a stretchable micro-supercapacitor patch (SMSP) with parallel, alternating offset Kirigami cuts.* ***(a)*** *3D exploded view and* ***(b)*** *top view illustrations of the layout in the SMSP. Different colors denote three key constituents: Kirigami cutting slots (red), graphitic electrodes (black), and polymer-based electrolyte (semi-transparent blue).* ***(c)*** *Cyclic voltammetry and* ***(d)*** *galvanostatic charge/discharge tests of the SMSP.* ***(e-g)*** *Optical image of (f) SMSP and (g) an intact polyimide sheet of the same size in initial and deformed configurations.*

2.2.3 Analysis of Buckling Determinism

As shown in **Fig. 2.6g**, the elongation of our SMSP is contributed by buckling-initiated out-of-plane deformation. Traditionally, structural buckling is associated with an unpredictable state of chaos, and is therefore, discouraged and circumvented by most engineers. In many cases across length scales, buckling was treated as the first route to failure, ranging from bridges [30] and pressure vessels [31], down to MEMS structures [32]. In recent years, many researchers have started to analyze buckling and to make use of controllable buckling instability, especially in developing exotic mechanical metamaterials, stretchable electronic systems, and unconventional soft sensors and actuators [33]. To utilize structural buckling for achieving stretchability, we need to confirm that the buckling in our SMSP is deterministic and predictable. In our study, we have performed finite element analysis (FEA) using the linear perturbation module of a commercial FEA package (ABAQUS) to calculate possible modes of buckling in our SMSP [3, 7, 34]. The Young's modulus of polyimide is set as 2.5 GPa, and effective modulus of the graphitic electrodes as 300 MPa, respectively in FEA. **Figure 2.7a** shows the computed buckling shapes corresponding to the first four buckling modes in top, side and 3D views, where the colors denote normalized out-of-plane displacements. The shape of Mode 1 is featured by all the five deformable units rotating in the same direction, and the cut slot in each unit opening slightly. This buckled shape is anti-symmetric about the central axis (denoted by dash-dot lines), as is apparent in the top and side views. In other words, if a point moves downward, its reflected point about the axis of symmetry moves upward by the same amount. Out of the first four modes, Mode 3 also has anti-symmetric buckling shape, whereas the buckling shapes of Mode 2 and 4 are symmetric about the central axis. The computed critical buckling strains ε_{crit} corresponding to the first four modes are shown in **Fig. 2.7b**. Because the critical buckling strain for Mode 1 ($\varepsilon_{crit} = 0.72\%$) is significantly lower than those of the other three modes (by 28% to 58%), the SMSP will buckle following the route of Mode 1 when it is elongated slightly (by 0.72%), before any other modes could possibly occur. **Figure 2.7c** shows the deformation energies of the SMSP as a function of elongation (from 0 to 100%) following the different routes defined by the four modes. Apparently, the deformation energy for Mode 1 is consistently smaller than that for other modes in ALL shown stages of elongation. Therefore, following the principle of minimum deformation energy, the SMSP should always deform along the route defined by Mode 1, and a snap-through to another mode is not expected to occur [35, 36]. Even if the deformation of the patch deviates from Mode 1 temporarily, it is expected to "snap back" to this mode quickly. As supported by both arguments (i.e., critical buckling strain and deformation energy) and later confirmed by experiments, Mode 1 is the only dominant mode expected to take place.

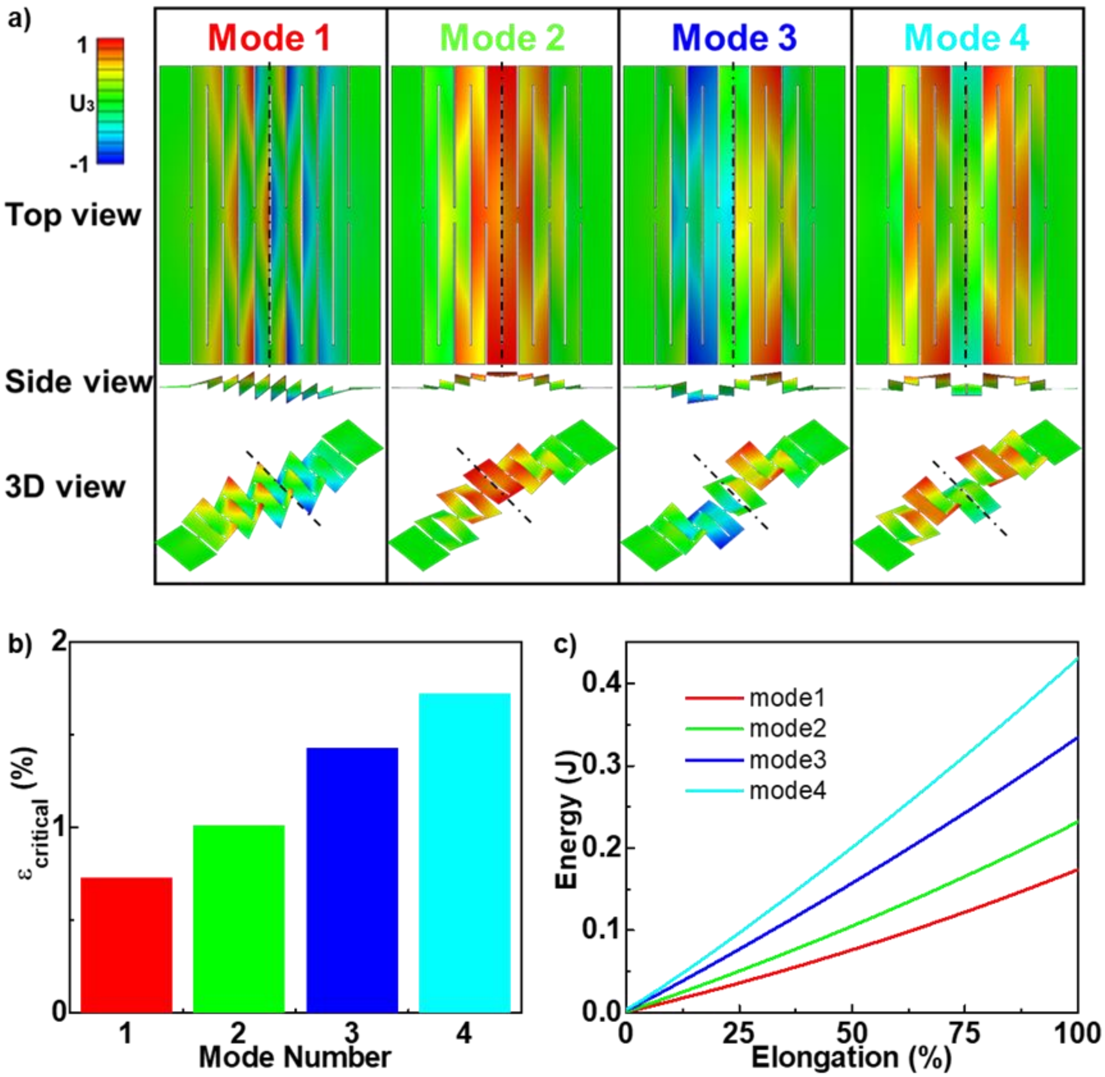

Figure 2.7 *Buckling determinism analysis of a representative SMSP. **(a)** The first four buckling modes of a SMSP shown in top view (top row), side view (middle row) and 3D view (bottom row). The color denotes out-of-plane displacement. **(b)** Critical buckling strain corresponding to the first four modes. **(c)** Deformation energy as a function of elongation for the first four modes. Mode 1 (shown in red) has both the smallest critical buckling strain and the lowest deformation energy.*

2.2.4 Post-Buckling Deformation

To systematically analyze the post-buckling deformation (i.e., elongation) of the SMSP samples, a failure criterion for the graphitic electrodes is required. Here, we designed an experiment and performed corresponding finite element analysis in order to set up a simple strain-based failure criterion, since well-recorded failure properties of this unconventional material are not readily available. **Figure 2.8a** illustrates the experiment setup, where a test sample with laser converted graphitic pattern is connected to a four-probe station. This station can characterize the resistance of the test sample (with the shape of a rectangular beam) clamped at two ends (in dash box). The initial length and resistance of the sample are L_0 and R_0, respectively. When the distance between the two ends is reduced by an amount $-\Delta L$, the sample bends upwards or downwards and results in a measured change in resistance ΔR. From the relationship between $\Delta R/R_0$ and $\Delta L/L_0$ plotted in **Fig. 2.8b**, we notice that the increase in resistance remains very small ($\Delta R/R_0$ < 2%) even when the end-to-end distance of the sample is shrunk by half ($\Delta L/L_0$ = -50%). However, further compressing the sample (either bent upwards or downwards) beyond $\Delta L/L_0$ = -50% will result in a significant, irreversible increase in resistance, most likely due to the microscale fracture within graphitic networks. **Figure 2.8c** shows the deformation (both upward and downward bending) of the sample with end-to-end distance reduced by 50%, as observed in experiment and predicted by FEA with very good agreement. At this level of deformation, the computed maximum absolute principal strain ε_{max} (via FEA) in the graphitic layer is 5.5%. Based on this result, we use "maximum absolute principal strain ε_{max} in the graphitic material reaching 5.5%" as the failure criterion in all following analyses.

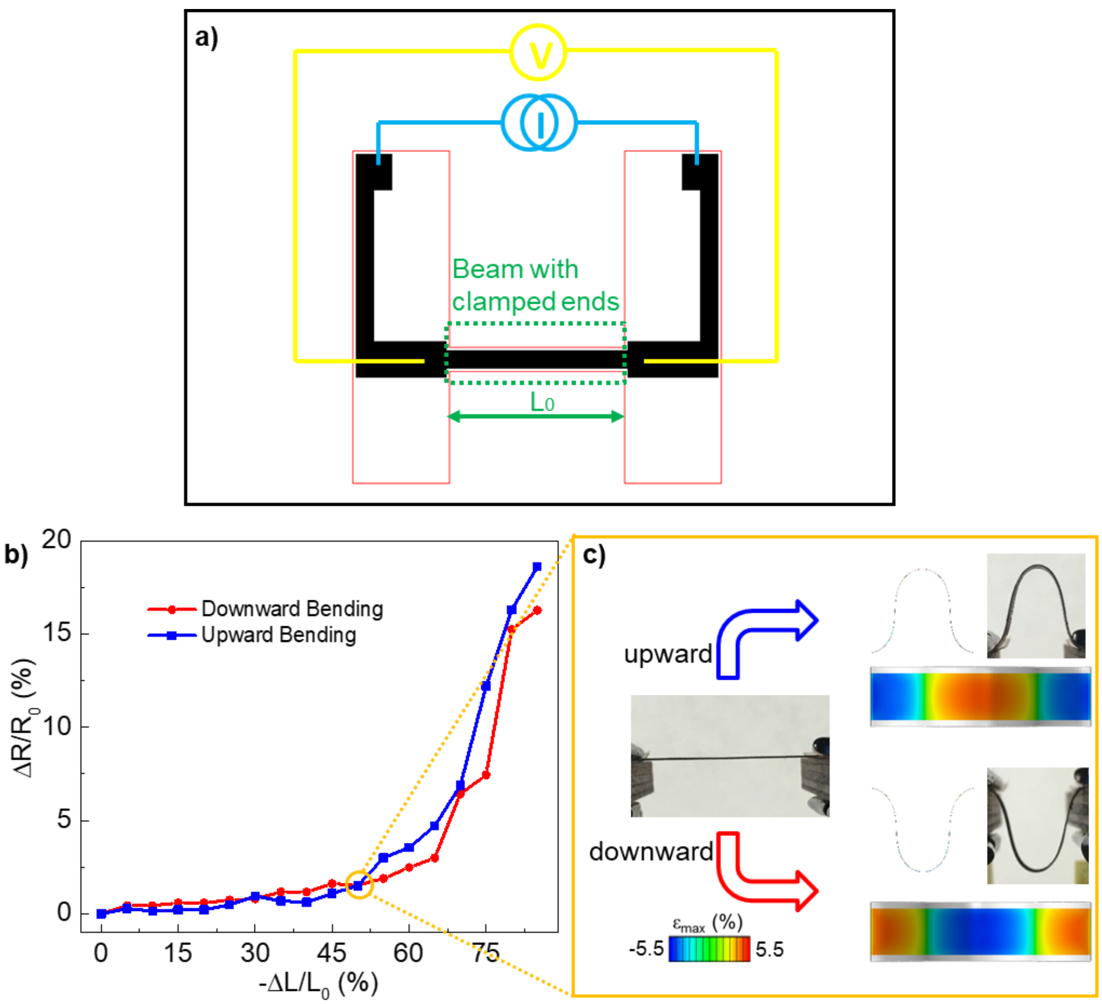

Figure 2.8 ***(a)*** *Schematic illustration of the experimental setup for measuring resistance of test sample during its bending deformation.* ***(b)*** *The relative change in resistance of the test sample as a function of the relative change in length, for both upward (blue) and downward (red) bending.* ***(c)*** *The FEA-predicted (top left in each group) and experimentally observed (top right in each group) deformation of the test sample at 50% compression. The color in the top view FEA image of the test sample denotes computed maximum absolute principal strain.*

Figure 2.9a shows the deformation of the SMSP at four different elongation stages (70.6%, 141.3%, 211.9% and 282.5%), as predicted by FEA (left column) and observed in experiments (right column). The modeling results agree very well with the optical images in almost all geometric details. As predicted, SMSP deforms following the route defined by Mode 1. When the SMSP is stretched beyond the onset of buckling (i.e., elongated by more than 0.72%), each deformable unit in the patch continues rotating, and the cut slots in each unit opens up further, such that the initially straight segments pop out of plane and bend considerably to accommodate the applied stretch. Both the rotation (and subsequent twisting) and the bending contribute to the overall stretchability of the SMSP. Because of this deformation mechanism, the actual elongation in the functional electrodes is quite small even when the SMSP is stretched by 282.5%, to almost four times of its initial length.

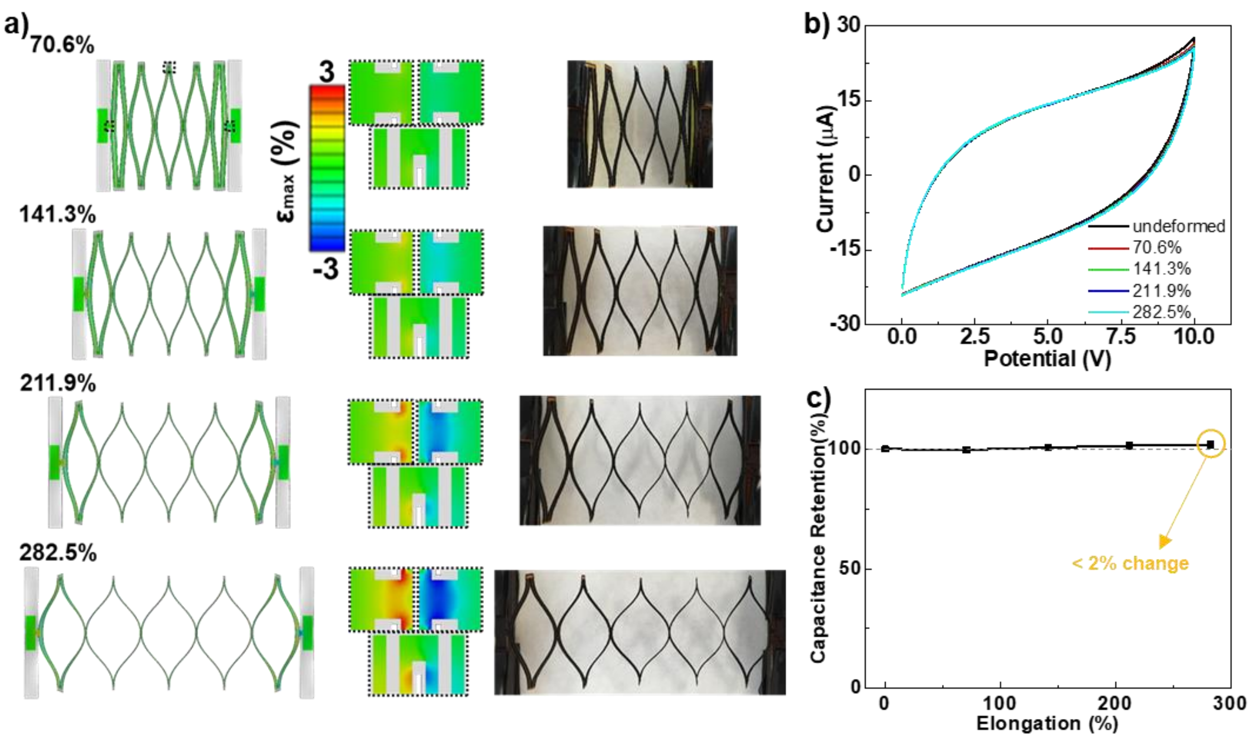

Figure 2.9 ***(a)*** *Post-buckling deformation of a representative SMSP, featuring FEA predictions (left column) and optical images (right column) of the SMSP at four deformation stages. The center*

column highlights strain distributions at selected sites with large deformation at each stage of deformation. Color in FEA images denotes computed maximum absolute principal strain. ***(b)*** *Cyclic voltammetry curves and* ***(c)*** *capacitance retentions of the SMSP under different elongations. The scan rate is 200 mV/s.*

In the center column of **Fig. 2.9a**, magnified views show the strain mapping at three representative regions that have the most significant strain concentration in the SMSP. Even in these regions, the maximum absolute principal strain (ε_{max} < 3.0%) in the graphitic electrodes is always lower than 3.7%, even for 282.5% of elongation. Because the strain in electrode material is quite small, we expect negligible degradation in electronic performance induced by the deformation of SMSP. In experiments, we find indeed that the five cyclic voltammetry curves corresponding to different elongation stages overlap very well (**Fig. 2.9b**). The change in capacitance retention is very small (less than 2%, **Fig. 2.9c**) even with significant overall stretching deformation (0% to 282.5%). Notably, this <2% change in capacitance is smaller than most reported stretchable supercapacitors, despite that our elongation of device is usually greater. Both the mechanical analyses and the electrochemical testing results above prove that our SMSP with this Kirigami construct can maintain full performances under extreme deformations.

While the elongation was limited by the range of our stretching platform at 282.5% in experiments, the FEA model predicts further deformation of SMSP up to 600% elongation, as shown in **Figure 2.10**. In the region with the most severe strain concentration (highlighted in magnified views), ε_{max} exceeds 5.5% when the overall elongation is greater than 510%. Therefore, we predict the stretchability of our SMSP to be ~510%, which is comparable to the value (500%) of the reported most stretchable supercapacitor [27]. Additionally, a rough stretching test by hand (**Figure 2.11**) demonstrates that mechanical integrity of the SMSP can be maintained at up to over 730% elongation, while rupture of the structure occurs at 775% elongation.

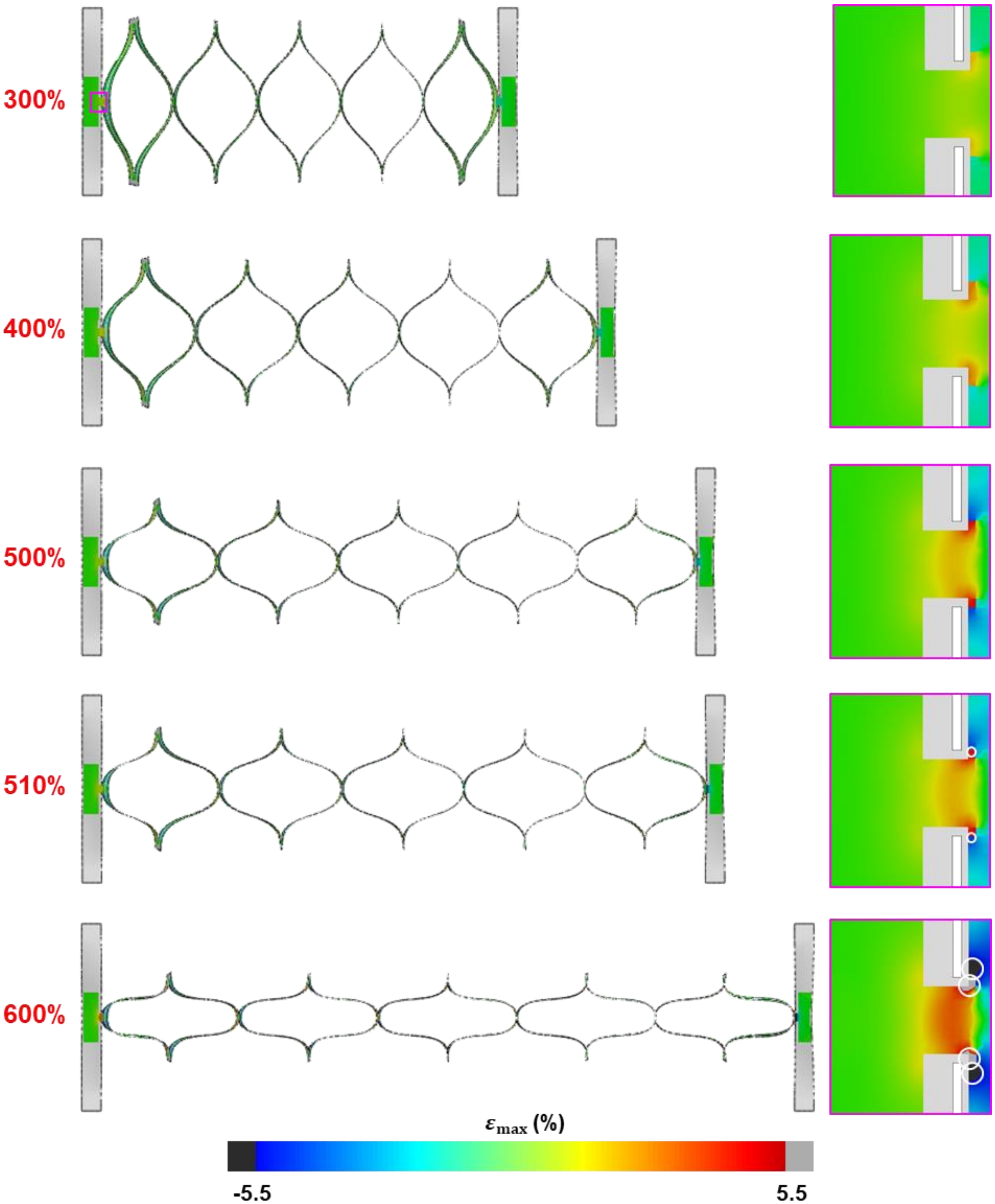

Figure 2.10 *Deformation of the SMSP with "alternating offset cuts" design at elongations beyond 282.5%, predicted by FEA. The magnified view shows the distribution of maximum absolute principal strain* ε_{max} *in the graphitic material, at the site with the largest deformation.* ε_{max} *reaches 5.5% when the overall elongation is 510%. The circles highlight local regions*

where ε_{max} is greater than 5.5% (with grey or black colors).

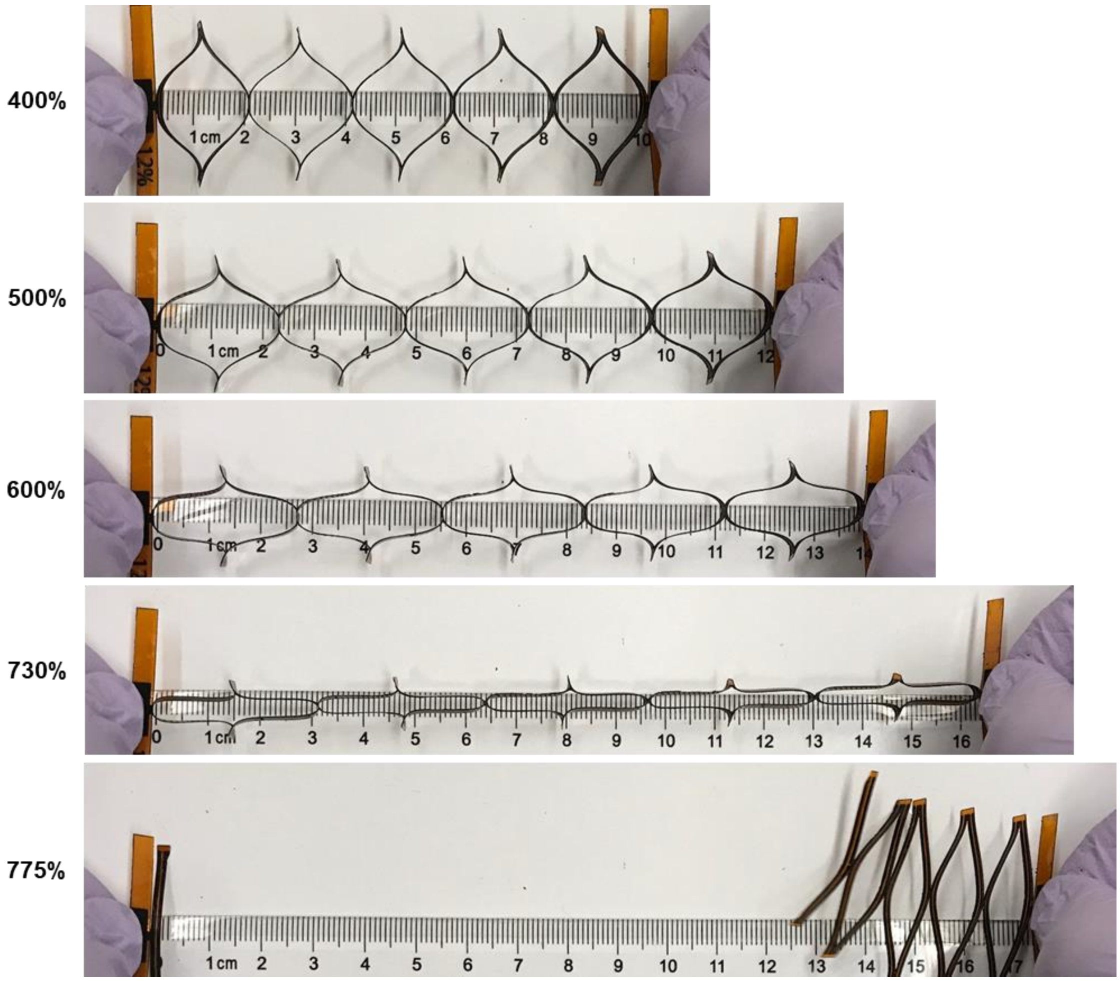

Figure 2.11 *Optical images of the SMSP at different stages of deformation in a stretching test by hand.*

2.2.5 SMSPs with Other Kirigami-inspired Designs

In the aforementioned SMSP with ten equivalent capacitors connected in series, we employed the most well-known Kirigami pattern, the "alternating offset cuts", to obtain high system-level stretchability. Inspired by the abundant existing Kirigami cut patterns, we have also designed equally stretchable micro-supercapacitor patches with various mechanical constructs and electrical connections. **Figure 2.12** illustrate examples of SMSPs with the same aforementioned overall size of patch (36.5 mm by 28 mm) but a distinct layout of cutting slots, electrodes and electrolyte.

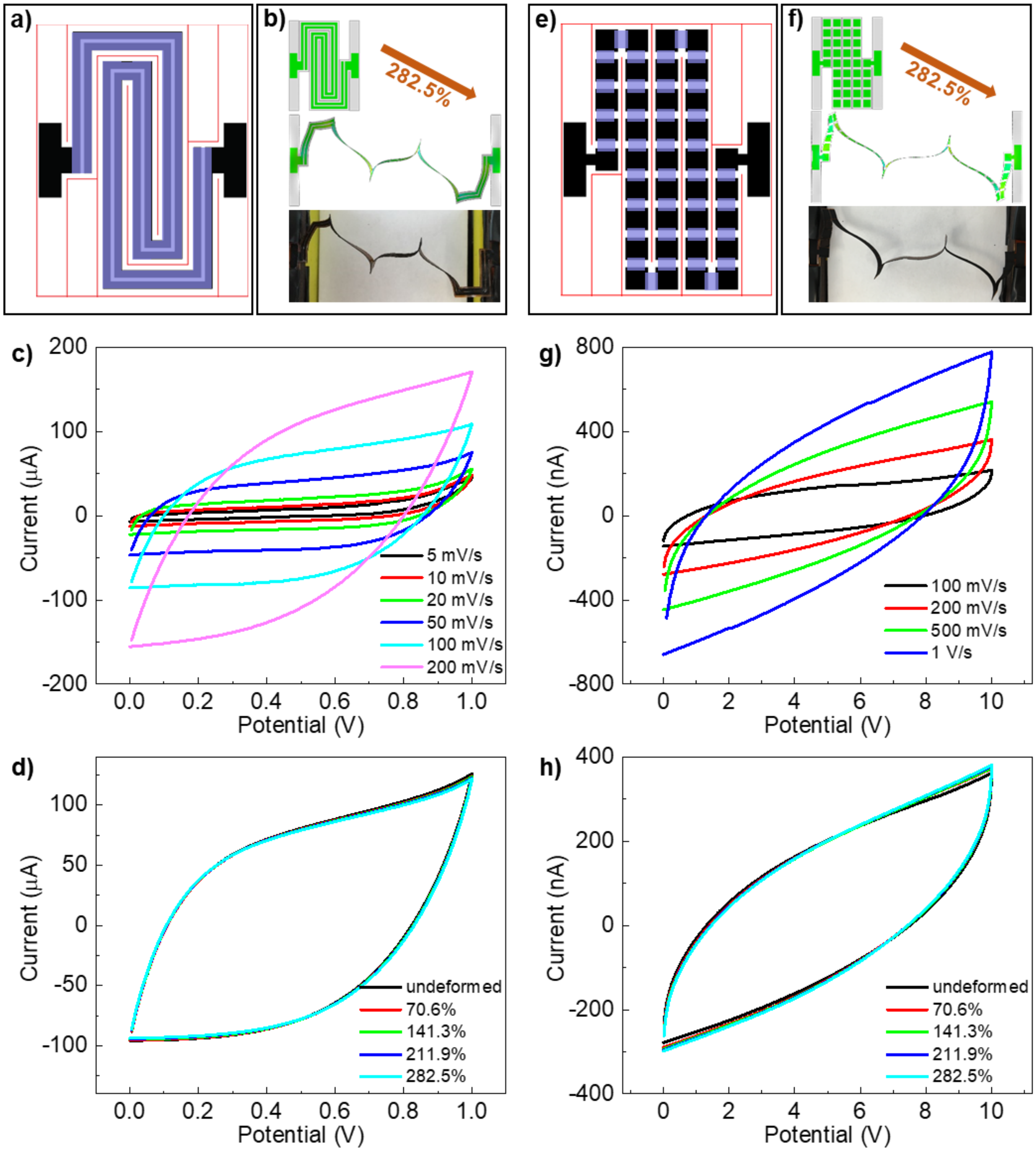

Figure 2.12 *Design, deformation and performances of SMSPs with two other Kirigami-inspired designs, namely,* ***(a-d)*** *the "double spiral" design and* ***(e-h)*** *the "zigzag serpentine" design. In (a) and (e), colors denote the layout of electrodes (black), Kirigami cuts (red) and electrolyte (semi-transparent blue) in each design. (b) and (f) show the deformations of SMSPs predicted by FEA (top: undeformed; middle: elongated by 282.5%) and observed in experiments (bottom: elongated by 282.5%). (c) and (d) show the cyclic voltammetry curves for the SMSP with "double spiral"*

design measured at (c) different scan rates and (d) different stages of deformation; (g) and (h) show the cyclic voltammetry curves for the SMSP with "zigzag serpentine" design measured at (g) different scan rates and (h) different stages of deformation.

The SMSP in **Figs. 2.12a-d** adopts a "double spiral" design. In this patch, the pair of parallel electrodes forms a path similar to two spirals joining together at the center. The areal coverage of functional components is 62.8%. This SMSP with two very long electrodes can be considered as one equivalent capacitor that can sustain 1 V. **Figure 2.12c** shows the cyclic voltammetry curves of this SMSP in its undeformed configuration. At a scan rate 10 mV/s, the specific capacitance is measured as 0.57 mF/cm^2. This lower value than that in **Fig. 2.6** is likely due to the much higher ionic resistance from the long electrode segments. When this SMSP is subject to a tensile load, the segments near the center buckle out of plane, and accommodate the stretch by rotating, bending and twisting in subsequent post-buckling deformations (**Figure 2.13a**). Similar to the SMSP in **Fig. 2.9**, this SMSP with double spiral design can maintain its full electrical performance (<0.9% change in capacitance retention) with up to 282.5% elongation (**Fig. 2.12b**), as justified by cyclic voltammetry tests performed at different stages of deformation (**Fig. 2.12d**).

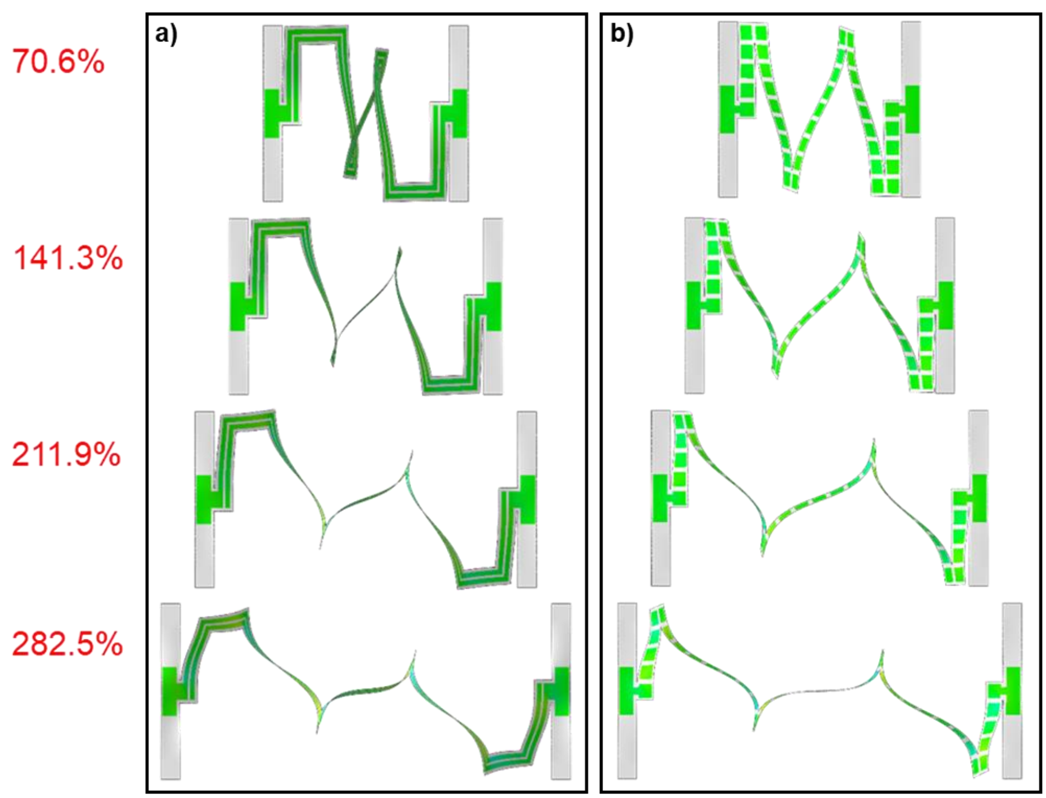

Figure 2.13 *Deformation at four stages of the SMSP with* ***(a)*** *the "double spiral" design and* ***(b)*** *the "zigzag serpentine" design, as predicted by FEA.*

In addition to the two SMSPs described here, the Kirigami concept can also be used in designing stretchable supercapacitor patches that can sustain higher voltage. **Figures 2.12e-h** feature an SMSP with “zigzag serpentine” design and areal coverage 67.1%. The thirty-seven square-shaped electrodes in this patch constitute a chain of thirty-six equivalent capacitors connected in series, and arranged in a path resembling a zigzagged serpentine. When the patch is stretched uniaxially, the Kirigami cutting slots in it allow different segments of the “serpentine” to buckle, rotate, bend and twist (**Figure 2.13b**). The cyclic voltammetry results in **Fig. 12g** yield a specific capacitance 0.531 mF/cm^2 at a scan rate 200 mV/s, when the scanning range is 0 to 10 V. We expect that this SMSP can potentially sustain a much higher voltage range (up to ~36 V), yet tests to validate this exceed the limit of our electrochemical workstation. Like the other two SMSPs described in previous paragraphs, the performance of this SMSP is also not affected by large uniaxial stretching. The change in capacitance retention is less than 1.8% throughout different stages of elongation up to 282.5% (**Fig. 2.12h**).

2.3 Materials and Methods

2.3.1 Device Fabrication and Testing

The graphitic electrodes and Kirigami cuts in the micro-supercapacitor patches were generated by irradiating commercial a polyimide sheet (*Kapton, Dupont*, thickness = 125 μm) with CO_2 laser (*Universal Laser Systems*, wavelength = 10.6 μm) at different optimized power and speed settings (9.6 W, 60 mm/s for forming graphitic electrodes, and 22.8 W and 60 mm/s for cutting, respectively). The electrolyte (mixture of 1 gram of polyvinyl alcohol + 1 gram of phosphoric acid + 12 gram of deionized water) is applied manually to selected regions on the patch. The performances of supercapacitors were measured on an electrochemical workstation (*Gamry Reference 600*).

2.3.2 Finite Element Analyses

3D FEA simulations were performed using a commercial simulation software (ABAQUS) to analyze the buckling behaviors and the post-buckling deformation of the SMSPs. The SMSPs composed of unconverted Kapton (polyimide, Young’s Modulus E = 2.5 GPa, Poisson’s ratio ν = 0.34) and graphitic electrodes (E = 300 MPa, ν = 0.3, estimated values.) were modeled with quadrilateral shell elements (S4R) [3, 7]. The overall deformations of the graphite/Kapton bilayer are mostly determined by the mechanical properties of polyimide. For different regions in the SMSP, the “Composite Layup” function was used to correctly define the thicknesses and properties of materials of each constituting layers. Since the solution-based electrolyte has almost no influence to the mechanical properties of the SMSP, it was neglected in the FEA modeling.

2.4 Conclusions of Chapter 2

This chapter presents a series of stretchable micro-supercapacitor patches with constructs inspired by the traditional Japanese craftwork, Kirigami. By adopting this design concept, we have achieved simultaneously high system-level stretchability and high areal coverage of functional components in the patches. These stretchable patches can be fabricated in simple steps by graphitic conversion and laser cutting, using the same commercial laser cutter with different heating level settings. Because the compliant Kirigami-inspired structure can easily sustain large deformation with very small strain in electrodes, the electrical performances of the patches are uncompromised even under extreme elongation. Various electrical connections among supercapacitors in one patch can be obtained by using different Kirigami designs, with different layouts of electrodes and cuts. In addition to micro-supercapacitors, we believe the proposed Kirigami-inspired designs can also provide a new way in the development of many other stretchable electronics and bioelectronics systems, especially for those requiring both high deformability and high functional areas.

References of Chapter 2

[1] J. A. Rogers, T. Someya, and Y. Huang, "Materials and mechanics for stretchable electronics," *Science,* vol. 327, no. 5973, pp. 1603-1607, 2010.

[2] J. Xu *et al.*, "Highly stretchable polymer semiconductor films through the nanoconfinement effect," *Science,* vol. 355, no. 6320, pp. 59-64, 2017.

[3] S. Xu *et al.*, "Stretchable batteries with self-similar serpentine interconnects and integrated wireless recharging systems," *Nature Communications,* vol. 4, p. ncomms2553, 2013.

[4] S. I. Park *et al.*, "Soft, stretchable, fully implantable miniaturized optoelectronic systems for wireless optogenetics," *Nature Biotechnology,* vol. 33, no. 12, pp. 1280-1286, 2015.

[5] D. Son *et al.*, "Multifunctional wearable devices for diagnosis and therapy of movement disorders," *Nature Nanotechnology,* vol. 9, no. 5, pp. 397-404, 2014.

[6] K.-I. Jang *et al.*, "Rugged and breathable forms of stretchable electronics with adherent composite substrates for transcutaneous monitoring," *Nature Communications,* vol. 5, p. 4779, 2014.

[7] S. Xu *et al.*, "Soft microfluidic assemblies of sensors, circuits, and radios for the skin," *Science,* vol. 344, no. 6179, pp. 70-74, 2014.

[8] S. Hong *et al.*, "Stretchable Electrode Based on Laterally Combed Carbon Nanotubes for Wearable Energy Harvesting and Storage Devices," *Advanced Functional Materials,* vol. 27, no. 48, 2017.

[9] X. Pu *et al.*, "Ultrastretchable, transparent triboelectric nanogenerator as electronic skin for biomechanical energy harvesting and tactile sensing," *Science Advances,* vol. 3, no. 5, p. e1700015, 2017.

[10] Q. Hua *et al.*, "Skin-inspired highly stretchable and conformable matrix networks for multifunctional sensing," *Nature Communications*, vol. 9, no. 1, p. 244, 2018.

[11] K.-I. Jang *et al.*, "Self-assembled three dimensional network designs for soft electronics," *Nature Communications,* vol. 8, p. 15894, 2017.

[12] J. W. Lee *et al.*, "Soft, thin skin-mounted power management systems and their use in wireless thermography," *Proceedings of the National Academy of Sciences,* vol. 113, no. 22, pp. 6131-6136, 2016.

[13] J. Pu, X. Wang, R. Xu, and K. Komvopoulos, "Highly Stretchable Microsupercapacitor Arrays with Honeycomb Structures for Integrated Wearable Electronic Systems," *ACS Nano*, vol. 10, no. 10, pp. 9306-9315, 2016.

[14] R. Xu *et al.*, "Fabric-based stretchable electronics with mechanically optimized designs and prestrained composite substrates," *Extreme Mechanics Letters,* vol. 1, pp. 120-126, 2014.

[15] R. Xu *et al.*, "Designing Thin, Ultrastretchable Electronics with Stacked Circuits and Elastomeric Encapsulation Materials," *Advanced Functional Materials,* vol. 27, no. 4, 2017.

[16] D.-Y. Khang, H. Jiang, Y. Huang, and J. A. Rogers, "A stretchable form of single-crystal silicon for high-performance electronics on rubber substrates," *Science*, vol. 311, no. 5758,

pp. 208-212, 2006.
[17] H. Jiang, D.-Y. Khang, J. Song, Y. Sun, Y. Huang, and J. A. Rogers, "Finite deformation mechanics in buckled thin films on compliant supports," *Proceedings of the National Academy of Sciences,* vol. 104, no. 40, pp. 15607-15612, 2007.
[18] Z. Niu *et al.*, "Highly Stretchable, Integrated Supercapacitors Based on Single-Walled Carbon Nanotube Films with Continuous Reticulate Architecture," *Advanced Materials,* vol. 25, no. 7, pp. 1058-1064, 2013.
[19] M. S. White *et al.*, "Ultrathin, highly flexible and stretchable PLEDs," *Nature Photonics,* vol. 7, no. 10, pp. 811-816, 2013.
[20] C. Yu, C. Masarapu, J. Rong, B. Wei, and H. Jiang, "Stretchable supercapacitors based on buckled single-walled carbon-nanotube macrofilms," *Advanced Materials,* vol. 21, no. 47, pp. 4793-4797, 2009.
[21] A. Lamoureux, K. Lee, M. Shlian, S. R. Forrest, and M. Shtein, "Dynamic kirigami structures for integrated solar tracking," *Nature Communications,* vol. 6, p. 8092, 2015.
[22] Y. Morikawa *et al.*, "Ultrastretchable Kirigami Bioprobes," *Advanced Healthcare Materials,* vol. 7, no. 3, p. 1701100, 2018.
[23] M. K. Blees *et al.*, "Graphene kirigami," *Nature,* vol. 524, no. 7564, pp. 204-207, 2015.
[24] L. Xu, X. Wang, Y. Kim, T. C. Shyu, J. Lyu, and N. A. Kotov, "Kirigami nanocomposites as wide-angle diffraction gratings," *ACS Nano,* vol. 10, no. 6, pp. 6156-6162, 2016.
[25] R. Sun *et al.*, "Kirigami stretchable strain sensors with enhanced piezoelectricity induced by topological electrodes," *Applied Physics Letters,* vol. 112, no. 25, p. 251904, 2018.
[26] H. Guo *et al.*, "All-in-one shape-adaptive self-charging power package for wearable electronics," *ACS Nano,* vol. 10, no. 11, pp. 10580-10588, 2016.
[27] Z. Lv *et al.*, "Editable supercapacitors with customizable stretchability based on mechanically strengthened ultralong MnO2 nanowire composite," *Advanced Materials,* vol. 30, no. 2, p. 1704531, 2018.
[28] D. Shin, C. Shen, M. Sanghadasa, and L. Lin, "Semi-transparent foldable supercapacitor for 3D structured energy storage devices," in *Micro Electro Mechanical Systems (MEMS), 2018 IEEE*, 2018, pp. 653-656: IEEE.
[29] J. Lin *et al.*, "Laser-induced porous graphene films from commercial polymers," *Nature Communications,* vol. 5, p. 5714, 2014.
[30] A. Nazmy, "Stability and load-carrying capacity of three-dimensional long-span steel arch bridges," *Computers Structures,* vol. 65, no. 6, pp. 857-868, 1997.
[31] S. Kyriakides and P. Shaw, "Inelastic buckling of tubes under cyclic bending," *ASME J. Pressure Vessel Technol,* vol. 109, no. 2, pp. 169-178, 1987.
[32] H. Guckel, T. Randazzo, and D. Burns, "A simple technique for the determination of mechanical strain in thin films with applications to polysilicon," *Journal of Applied Physics,* vol. 57, no. 5, pp. 1671-1675, 1985.
[33] P. M. Reis, "A perspective on the revival of structural (in) stability with novel opportunities

for function: From buckliphobia to buckliphilia," *Journal of Applied Mechanics,* vol. 82, no. 11, p. 111001, 2015.
[34] Y. Zhang *et al.,* "Buckling in serpentine microstructures and applications in elastomer-supported ultra-stretchable electronics with high areal coverage," *Soft Matter,* vol. 9, no. 33, pp. 8062-8070, 2013.
[35] J. T. Overvelde, D. M. Dykstra, R. de Rooij, J. Weaver, and K. Bertoldi, "Tensile instability in a thick elastic body," *Physical review letters,* vol. 117, no. 9, p. 094301, 2016.
[36] S. Shan *et al.*, "Multistable architected materials for trapping elastic strain energy," *Advanced Materials,* vol. 27, no. 29, pp. 4296-4301, 2015.

Chapter 3: Multilayer Stretchable Electronics by a Two-mode Mechanical Cutting Process

3.1 Introduction

Over the last decade, stretchable electronics have drawn widespread research attentions [1-4] with multiple electrical functionalities during and after repeated mechanical deformations of flexing, twisting, and stretching [5-9]. The compliant mechanics is comparable to biological tissues with the capabilities of conformally adapting to the curvilinear surfaces of skin and organs for epidermal or implanted biomedical applications [5-8, 10-15]. While some of these systems are made of intrinsically soft functional materials [11, 12], many of them obtain their deformability through structural innovations. One example is the "island-bridge" construct [5, 7-10, 14], where functional electronic components reside on rigid "islands" connected by meandering interconnect "bridges" for the purpose of both electrical conduction and structural connection. When the entire system is deformed, the functional electronic components have low strain and structurally compliant, serpentine-shaped interconnects provide all the mechanical deformability. As such, traditional non-ductile electronic materials (e.g., metal conductors, silicon-based semiconductors, commercial surface-mount chips and polymeric insulating layers) can be fully employed in the stretchable electronics devices, typically through photolithography-based processes.

Figure 3.1a shows the representative major processing steps of a typical stretchable electronics device consisting of an insulating foundation layer, a metallization layer, and an insulating cover layer, from bottom to top. Each layer has a unique pattern and would require a separate patterning step (i.e., Step 2, 3, and 4 in **Fig. 3.1a**). For a photolithography-based process, at least *three* photomasks would be required. Specifically, after depositing the insulation foundation layer (e.g., polyimide or parylene) on the wafer surface, a metal layer is deposited (Step #1) and the metal pads and interconnects are patterned with the *first* photomask through a lift-off or standard wet etching process (Step # 2). A cover layer (e.g., polyimide or parylene) is spin-coated and cured or vapor deposited on top, and patterned with the *second* photomask via reactive ion etching (RIE) to protect interconnects while exposing pads for vertical electrical connections (Step #3). Finally, the entire trilayer is defined by the *third* photomask, via etching (RIE) through the entire thickness (Step #4), before the bonding with functional electronic components and released from the wafer (Step #5).

While lithography-based fabrication is effective, high-yield and consistent in the industrial large scale manufacturing, it is hardly an ideal approach for stretchable electronics when only a small batch of samples are needed during research and prototyping stages. For many researchers in universities or small institutes, accesses to cleanroom environment and lithography-related specialty equipment (spin coater, mask aligner/stepper, sink for development and resist stripping, oxide deposition chambers, and reactive ion etcher, etc.) are expensive and the cost of highly specific photomasks may also be a burden to limited research budgets. The lithography-based processes are also time-consuming, especially in the long dry etching steps to define foundation and cover layers, and during the design, fabrication and shipping of photomasks. Furthermore, while photolithography could produce excellent pattern resolutions (down to micron or nanometer scale), this level of resolution may not be necessary for many stretchable electronics systems with typical size ~10 cm^2 and smallest feature size of ~100-500 μm.

Researchers have been exploring alternative fabrication processes, such as the use of a commercial vinyl cutter for defining one layer of stretchable interconnects, antennas or structured electrodes [16-18]. These studies are often limited to simple structures, where the metallization and underlying foundation layer share the same pattern. In this chapter, we aim at providing a solution for photolithography-free fabrication of stretchable electronics systems with multiple layers of patterned materials as illustrated in **Fig. 3.1a**, by using two modes of mechanical cutting processes using a vinyl cutter.

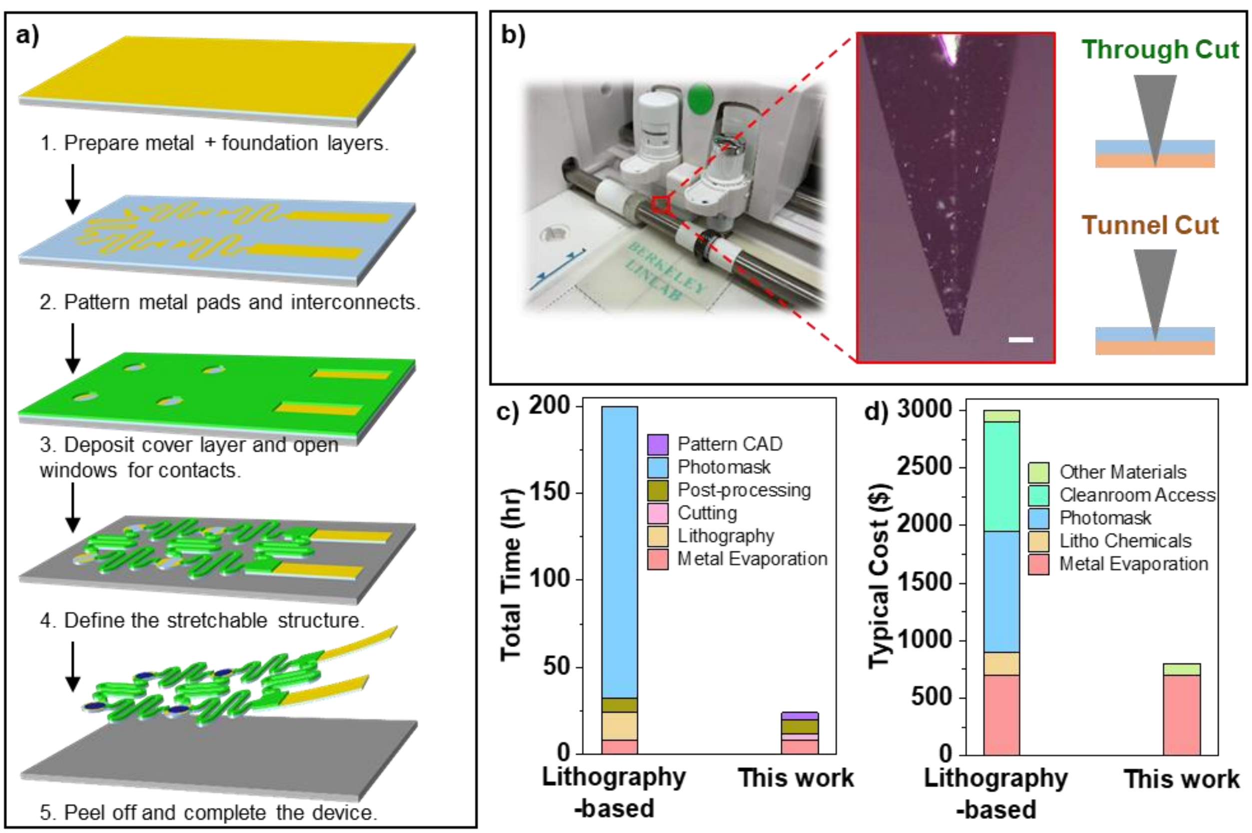

Figure 3.1 ***(a)*** *Schematics of a typical fabrication process for stretchable electronics. Steps 2, 3, and 4 are pattern-defining steps.* ***(b)*** *Experimental setup (left column) and the two modes of mechanical cutting: through cut and tunnel cut (right column). Center column: optical microscopy image of a cutting blade. Scale bar: 100 μm.* ***(c-d)*** *Comparisons of (c) total time and (d) typical cost between a photolightography-based process and the two-mode cutting process in this work.*

3.2 Results and Discussion

3.2.1 Fabrication based on the Two-mode Mechanical Cutting Process

Figure 3.1b shows a desktop-sized commercial vinyl cutter used for the patterning of material layers (CAMEO 3, *Silhouette Inc*.) and an optical microscopy image highlighting the tip of a cutting blade. For a flexible bilayer film with two layers of different materials, this setup can achieve two useful modes of mechanical cutting, namely "through cut" and "tunnel cut", along programed straight or curvilinear routes by tuning the applied vertical force and the cutting depth shape of the blade. The commonly used "through cut" results from high force and sufficient blade cutting depth shape, where the generated cut slots penetrate through both material layers. The "through cut" process can be used to define the outlines of the entire deformable structure (shown in Step #4 of **Fig. 3.1a**), therefore serving as a comparable function to the patterning step plus the subsequent long RIE in lithography-based processes. By lowering the applied force and if applicable, reducing the blade cutting depth shape, the "tunnel cut" mode can be achieved by only extending the cutting depth shape to the interface between the upper and lower layer to create a "tunnel" in the upper layer, while the lower layer remains structurally intact. This "tunnel cut" process is particularly intriguing, as it is the foundation for patterning the metallization and the insulating cover layers (i.e., Steps #2 and #3 in **Fig. 3.1**) without the need of photomasks or etching steps.

Figure 3.2 shows the details to construct the metal and cover layers for stretchable electronics using the "tunnel cut" process. For the bilayer film, the upper layer is an insulating single-sided flexible tape with the adhesive side facing down to seamlessly connect to the top surface of the lower layer, a non-sticky flexible film. The fabrication of the metal layer in the stretchable electronics can accomplished (**Fig. 3.2a**) by: (1) using a "tunnel cut" process first and peeling off selected regions on the top layer; (2) utilizing the remaining features on the upper layer as a physical mask during the metal evaporation process; and (3) peeling off the remaining parts of upper layer to complete the metal patterning process. We refer to this metal patterning approach as the "mechanical lift-off" process, because of its resemblance to the widely used lift-off process in traditional micromachining. The fabrication of the opening areas in the stretchable electronics can be conducted (**Fig. 3.2b**) by: (1) using a "tunnel cut" process along the contours of the opening areas to separate them from the main portions of the upper layer; and (2) peeling off the main structure of the upper layer and transfer-pasting it to an insulating foundation film. For devices requiring multilayer cutting/patterning, geometric alignment marks are included in the patterns of each layer, similar to the practice in a multi-mask lithography process in the traditional microfabrication schemes to control the layer-to-layer alignment error within an acceptable range of about 30 μm.

With the inclusion of both the "tunnel cut" and "through cut" processing modes, a five-stage stretchable electronics fabrication process can be achieved. Compared with lithography-bases processes, this two-mode mechanical cutting process can save up to ~88% of processing time, and ~73% of cost for a small-batch production (~20 samples, four runs in total) of a stretchable electronics module with three layers of patterns and resolution of 400 μm (**Fig. 3.1c, d**). The key reductions in time (~82%) and cost (~35%) are from the elimination of photomasks to avoid the long fabrication and shipping cycles (days) and costs (hundreds of US dollars). Defining the outlines of insulating layers can be accomplished within a few minutes per sample by the cutting blade, rather than a few hours or more by RIE. Furthermore, the cutting-based fabrication does not require the accesses to lithography-related specialty tools or cleanroom, therefore saving the overall cost. While the pattern resolution in the range of 100 μm is not as high as those fabricated by the photolithography processes, it is adequate for many stretchable electronics systems [7-9, 13, 14]. The remarkably shorter process cycles makes the process particularly suitable for fast and rapid prototyping of skin-mountable or implantable electronics systems and early-stage developments of stretchable electronics in university and institute labs.

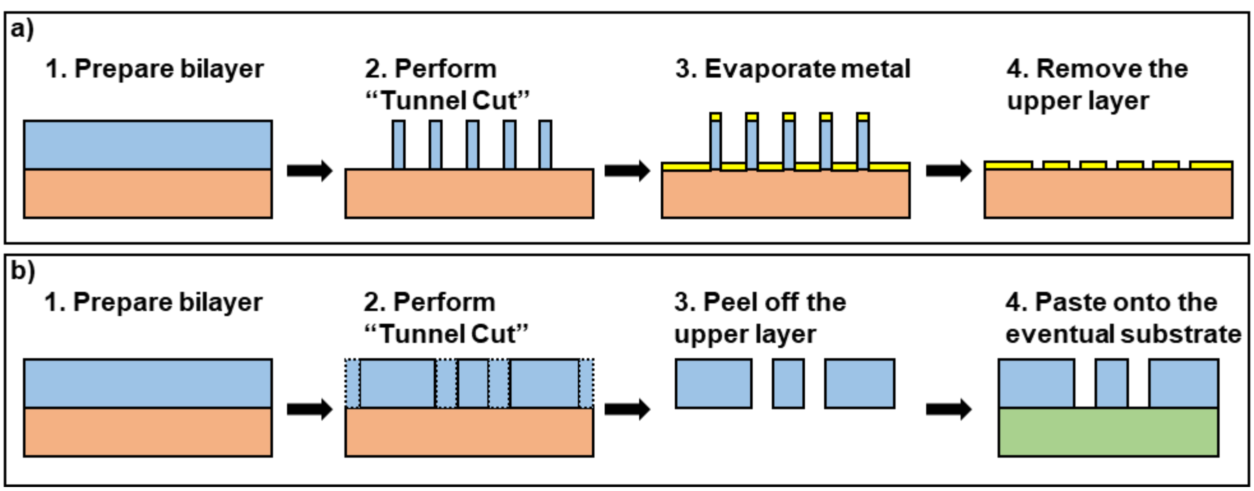

Figure 3.2 *Process flow using the "Tunnel Cut" mode for:* ***(a)*** *patterning the metal layer and* ***(b)*** *defining the insulating cover layer.*

A systematic characterization on the parameters of the cutting process has been conducted by changing the applied force and the cutting depth shape of the blade on a PET/adhesive/Mylar film of 25/15/40 μm in thickness, respectively, as shown in **Figure 3.3a**. The applied force can be tuned among 33 levels set by the commercial cutter (from Level 1 to 33, a greater number represents a higher force), and the effective blade depth can be set at 10 locations (from Location 1 to 10, a greater number represents deeper cuts). With the blade depth fixed at depth 1 (the shallowest depth), "tunnel cuts" on this film can be achieved by setting the applied force equal or below Level 9 but above Level 4, and "through cuts" are demonstrated by setting the applied force equal for above Level 10 (**Fig. 3.3b**). It is difficult to have clear photos on the cross-sections for the film, a commercial elastomer is utilized and the flipped structural morphologies are examined in SEM images (**Fig. 3.3c-h**). A slot angle, θ, is defined as the angle at any point along the side wall of the cut and the horizontal line. This slot angle changes drastically when the blade penetrates through the interface between PET and adhesive, and between adhesive and Mylar film (also one form of PET), because of the considerable differences in their Young's moduli (by more than two orders of magnitude). The slot angle is acute in the harder material (i.e., PET), yet becomes obtuse in the much softer adhesive.

The slot angle helps explaining the SEM images corresponding to results from different force levels and material interfaces (i.e., locations with sudden changes in the slot angle, marked by yellow arrows). It is found that that the blade-shape remains in the PET portion of tape when the force is at Level 1 (**Fig. 3.3c**), and the blade digs into the adhesive part at Level 3 (**Fig. 3.3d**), and penetrates through adhesive to marginally reach the Mylar film at Level 4 (**Fig. 3.3e**). From many cutting experiments, Level 4 is found to be the desirable force setting for the "tunnel cut", as it provides consistent cuts through the upper layer (PET tape), without significant marks or scratches to the lower layer (Mylar film). When the applied force is further increased, the blade cuts deeper into the lower layer (**Fig. 3.3f, g**), until this layer is also penetrated at Level 10 or beyond (**Fig. 3.3h**). We pick Level 11 for the "through cut" mode to guarantee consistency in defining the outlines of the stretchable structures and set the force (Level 4 for "tunnel cut", Level 10 for "through cut") and blade depth (depth 1) for the patterning processes in this work for stretchable electronics with multilayer structures.

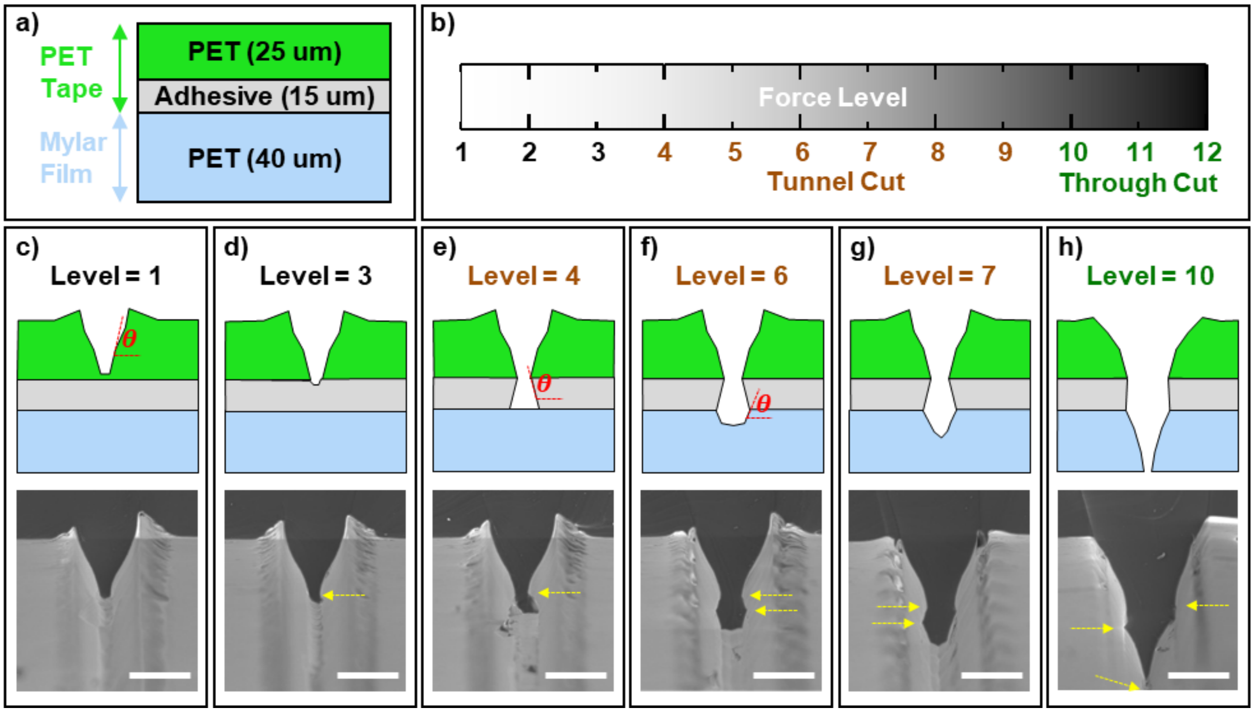

Figure 3.3 ***(a)*** *Cross-sectional profile of a PET/Adhesive/Mylar film.* ***(b)*** *Force level vs. the mode of cutting for the film in (a).* ***(c-h)*** *Schematic illustrations (top row) and SEM images (bottom row) showing the effect of mechanical cutting process at different force levels. Scale bars: 50 µm. Yellow arrows in SEM images correspond to interfaces between two materials, with the drastic changes in the slot angle.*

To explore the vinyl cutter's capacity for cutting through thick materials, such as a Kapton film with the thickness of ~125 µm, experiments have been conducted by exploiting all 33 force levels of the cutting machine, at two blade depth settings of 1 and 2 (**Fig. 3.4a**) and measure the obtained depths of cuts through SEM images (**Fig. 3.4b**). When the applied force is at or below Level 15, the shorter (depth 1) and longer blade (depth 2) give nearly identical results, and the resulting cutting depth in both cases depends solely on the force level (**Fig. 3.4b-f**). The two curves diverge beyond Level 15, where the depth of the cuts from the longer blade continues to increase with applied force, yet stagnant increment and plateauing eventually, likely due to the bottom-out of the blade length, is observed for the shorter blade (**Fig. 3.4b, g, h**). Therefore, adjusting blade depth is necessary for performing "through cut" on relatively thick films. With the blade depth set at depth 2, "through cut" is achieved for the Kapton film when the force level is at or beyond Level 27 (**Fig. 3.4b, i, j**).

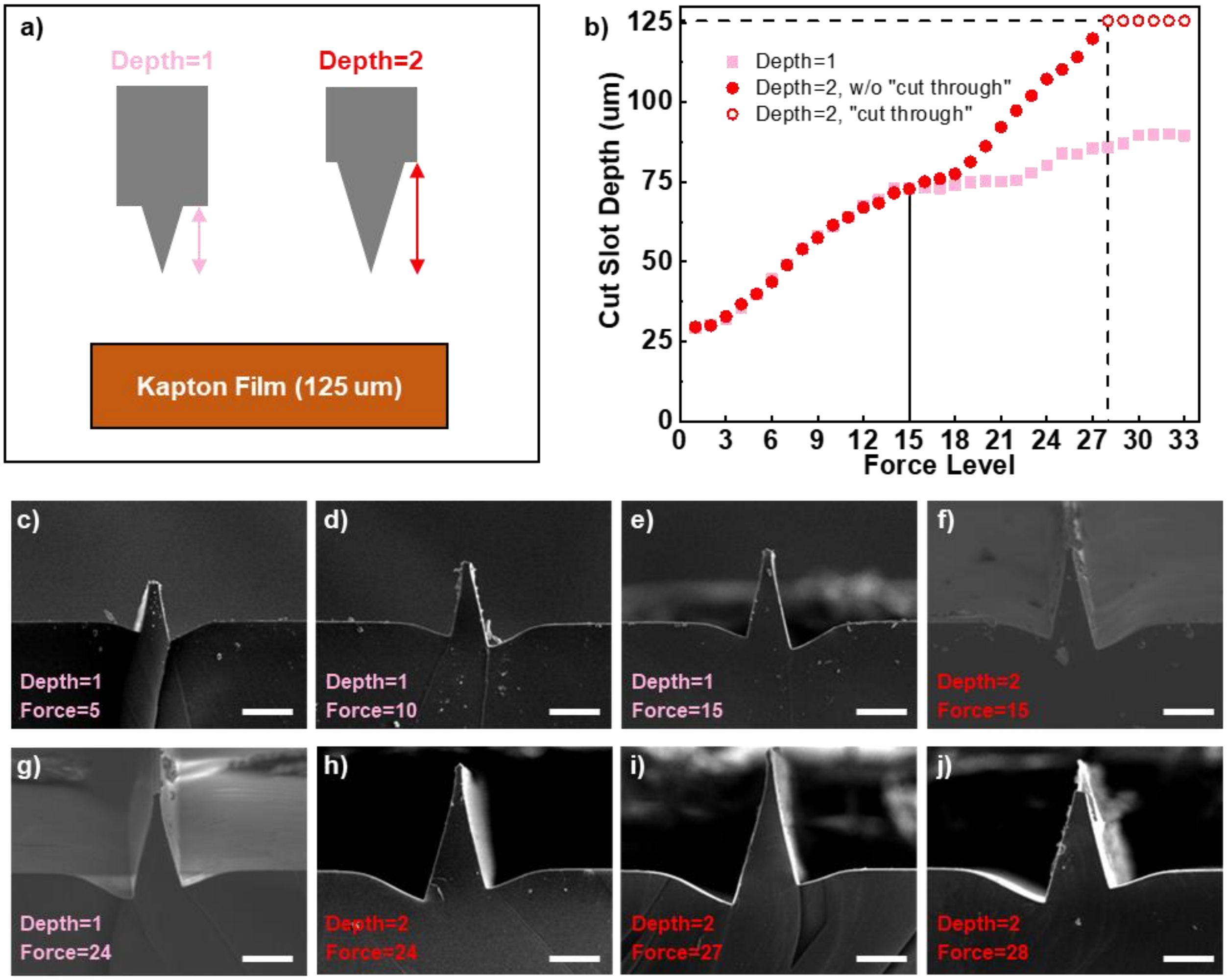

Figure 3.4 *(**a**) Illustration of the blade with two cutting depth shape settings and a thick Kapton film sample. (**b**) Depth of cut vs. force level measured in experiments. (**c**) SEM images of elastomeric features representative of the shape of the cuts, produced from different blade depth settings and force levels. Scale bars: 50 μm.*

With the convenient tuning of applied force and blade depth shape on the cutter, the cutting-based fabrication scheme can accommodate various flexible film materials with different thicknesses, and is therefore applicable to the fabrication of many stretchable electronics systems. In this work, we report two representative devices to show the capabilities of this rapid, low-cost fabrication approach. The first example is a water-resistant, stretchable supercapacitor patch to demonstrate the successful patterning of multiple layers with excellent deformability. The second device is a skin-mountable breathing monitoring module for biomedical applications with the integration of commercial electronic components.

3.2.2 Water-Resistant Stretchable Supercapacitor Patch

Figure 3.5a illustrates the structure of a water-resistant, stretchable supercapacitor patch (WSSC) in the exploded view, featuring four patterned layers made of PET tape, laser-induced graphene (LIG), gold, and Mylar film, respectively. The LIG (thickness ~10 μm) active electrodes are soaked with PVA-based electrolyte and reside on a layer of gold current collectors and electrical interconnects. LIG electrodes, gold current collectors, and electrolyte form the functional components of each supercapacitor units. The six supercapacitor units and the gold interconnects among them are sandwiched by two insulating layers: a Mylar film (thickness ~40 μm) as the foundation layer on the bottom side, and a PET tape (thickness: PET 25 μm + adhesive 15 μm) as the cover layer on the top side. The adhesive on the PET tape seals intimately with the Mylar film to provide a reliable protection for the functional components against harsh external environment (e.g., contaminants, water or humidity, and mechanical wear and impact). The functional components are also placed near the mechanical neutral surface to prevent excessive strain, thanks to the comparable thicknesses of the foundation and cover layers, and the similar mechanical properties of PET and Mylar (Young's modulus ~4 GPa). While six supercapacitor units and all interconnects are fully encapsulated from both sides, the small hexagonal "island" in the center is opened from the top-side (i.e., cover layer). The exposed metal patterns serve as the contact pads to power consumption devices, and as outlets for the charging and discharging of the entire WSSC. The entire WSSC can easily fit in the palm of a human hand (**Fig. 3.5b**). **Figure 3.5c** visually demonstrates the water-resistance capabilities of the WSSC. While all six of the supercapacitor units are immersed in water, the WSSC can still maintain its performance and light up a commercial LED mounted on the contact pads, placed above water. SEM images in **Fig. 3.5d** and **Fig. 3.5e** show the representative cross-sectional profile of a supercapacitor unit in WSSC, featuring the four intimately stacked constituent layers.

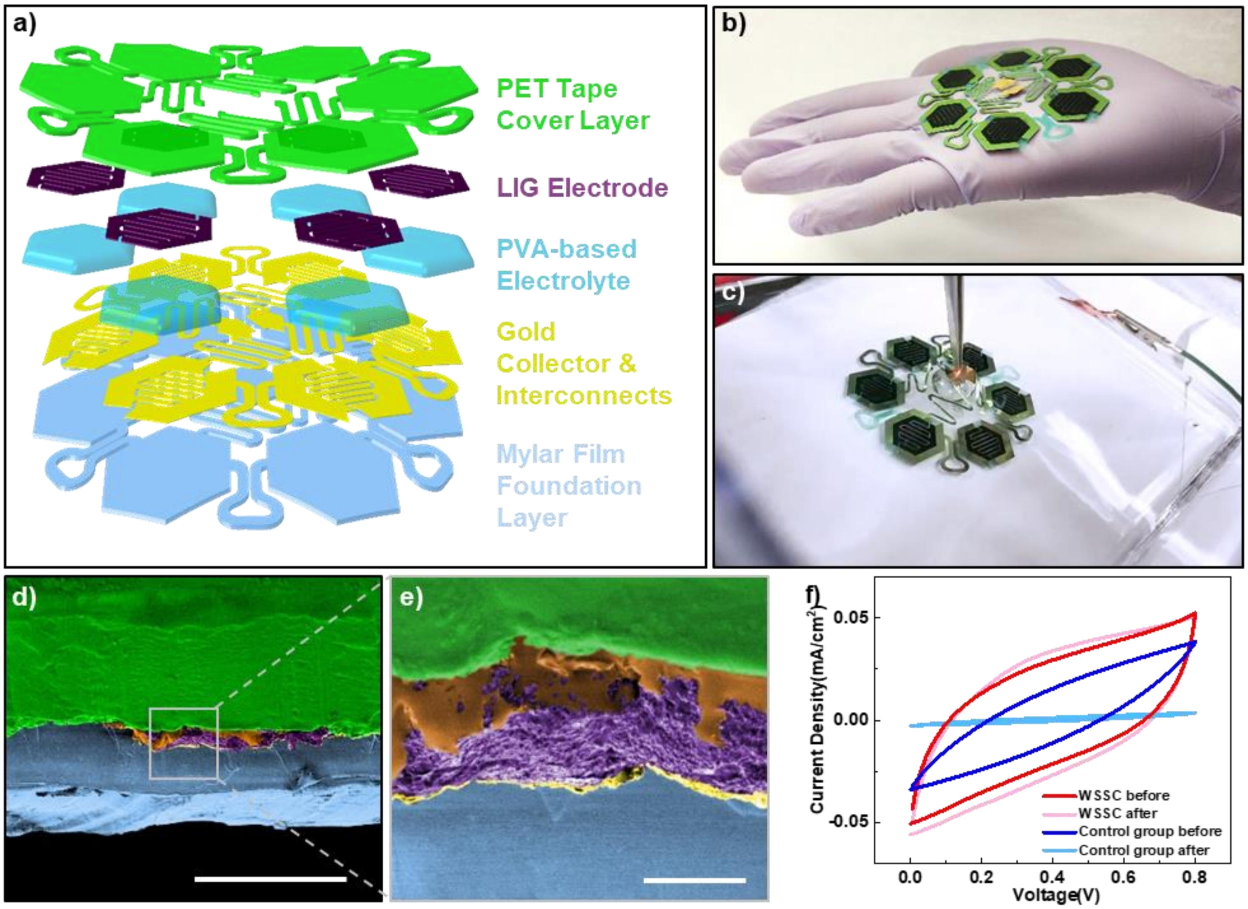

Figure 3.5 ***(a)*** *Schematic illustration of a water-resistant stretchable supercapacitor patch (WSSC) in exploded, layer-by-layer view.* ***(b)*** *An as-fabricated WSSC device compared to a human hand.* ***(c)*** *Optical image of WSSC providing power for an LED, with all WSSC units under water.* ***(d-e)*** *False-colored SEM images of a cross-sectional profile of WSSC electrodes. (e) is a magnified local site of (d). Color codes: green and orange for the structural and adhesive part on PET tape respectively, purple for LIG soaked with PVA-based electrolyte, yellow for gold collectors, and blue for the Mylar film. Scale bars: 50 μm in (d), 5 μm in (e).* ***(f)*** *Cyclic Voltammetry of one WSSC unit and a control group sample before and after 16-hour water immersion.*

Figure 3.6a illustrates the fabrication procedures of WSSC by both the "tunnel cut" and the "through cut" modes. In the first step (Step A1), active LIG electrode patterns are generated by irradiating selected regions of a Kapton film, using a commercial CO_2 laser cutter. Next (Step A2), a PET tape is applied with the adhesive side onto the Kapton film surface to form a PET tape/Kapton film bilayer. Because the bonding between LIG and adhesive is much stronger than that between LIG and Kapton film, patterned electrodes can be transferred to the PET tape during a separation process in a later step. The "tunnel cut" mode of the vinyl cutter is used to open a window in the PET tape to expose the contact pads (Step A3), before the PET tape is peeled off (Step A4) with LIG electrodes attached to it from the Kapton film. This PET tape will serve as the cover layer in WSSC. On the other side, a PET tape/Mylar film bilayer is prepared and fixed to the cutting platform on the vinyl cutter (Step B1). The vinyl cutter reads the CAD file corresponding to gold patterns and performs “tunnel cuts” through the PET tape, along predesigned paths (Step B2). After these cuts, some parts of PET tape are removed to prepare the bilayer for gold evaporation. With the remaining PET tape removed after evaporation, the gold current collectors and interconnects patterns are ready (Step B3). A PVA-based electrolyte in liquid form (mixture of 1 gram of polyvinyl alcohol + 0.42 gram of lithium chloride + 10 gram of deionized water) is then applied to the top surface in selected regions (Step B4). In Step 5, the PET tape with LIG (from Step A4) and the Mylar film with gold patterns and electrolyte (from Step B4) are carefully aligned with alignment masks on both layers as visual aid, and pressed together as the adhesive on PET tape bonds to the surfaces on gold and Mylar. The LIG electrodes are now transferred onto current collectors, soaked with electrolyte, and encapsulated from both sides. All six supercapacitor units are functionalized in this step. Finally, the vinyl cutter performs deep “through-cuts” along programmed routes and defines the outlines of the entire device (Step 6). This procedure facilitates rapid, low-cost fabrication of a multilayer device with several different patterned layers. In a timed experiment (**Fig. 3.6b**), we fabricated a batch of five devices in ~250 minutes, with about half of the time (~120 minutes) spent in the metal evaporation step involving long pumping/evacuating cycles. While the time budget is already low at ~50 minutes per device, this number could potentially be further reduced with steps A1-A4 and B1-B4 are performed in parallel. Since no cleanroom photolithography procedures (i.e., photomask making, photoresist coating, exposure and development, growth of oxide hard mask, reactive ion etching, etc.) are required, the cost of this fabrication process is remarkably lower than that of a comparable, small-batch lithography-based process.

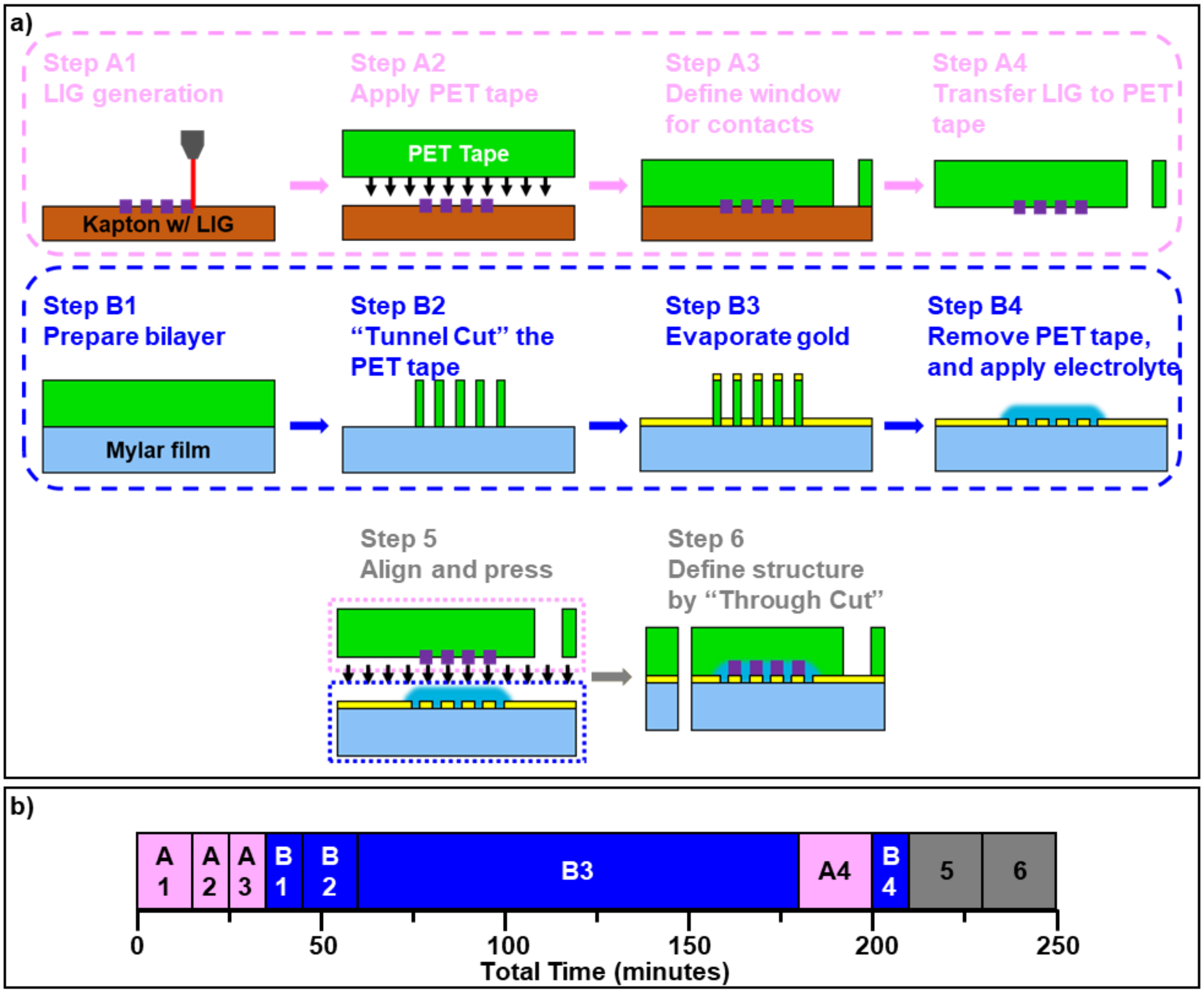

Figure 3.6 *(a) Fabrication processes for WSSC using the two-mode mechanical cutting process. (b) A time break-up for each fabrication steps shown in (a). Five samples are fabricated simultaneously.*

We first evaluate the electrochemical performances of one supercapacitor unit in WSSC, by performing cyclic voltammetry (CV), Galvanostatic charge-discharge (GCD), and electrochemical impedance spectroscopy (EIS) tests and comparing the results with a control group sample: the same LIG supercapacitor on its intrinsic Kapton film substrate, without gold collectors or cover layer (**Fig. 3.7a**). The tests were performed on devices as fabricated and after immersion in deionized water for sixteen hours for evaluating the water-resistance properties of WSSC units (**Fig. 3.7b**). Before immersion in water, the WSSC unit yields specific capacitance between 330 and 670 $\mu F/cm^2$, at discharge current densities between 200 and 10 $\mu A/cm^2$. These values are significantly higher (by several times) than the control group throughout the range of testing (**Fig. 3.7c**). A cyclic voltammetry scan at 100 mV/s suggests that the WSSC unit yields the more desirable rectangular-shaped CV curve (red) with much larger enclosed area, while the curve for the control group (blue) shows a thin, spindle-shape (**Fig. 3.5f**). Additionally, the WSSC unit has much lower equivalent series resistance (red, ~60 Ω) than the sample in control group (blue, ~2000 Ω), as shown by the Nyquist plot in **Fig. 3.7d** and **Fig. 3.7e**. The superior performances of the WSSC unit over the control group can be attributed to the gold current collector, whose much lower internal resistance (~0.3 Ω/square) than LIG (~10Ω/square) effectively enhances the charge transports in the device.

After extensive immersion in DI water for sixteen hours, the control group lost its electrochemical performance almost completely, as its CV loop almost collapsed to a line with negligible enclosed area (**Fig. 3.5f**, light blue), and the chaotic scatterings in the Nyquist plot (**Fig. 3.5d**, light blue). In comparison, the WSSC is capable of maintaining almost unaffected electrochemical performances: the CV curve for after immersion (**Fig. 3.5f**, light red) does not change much from that before immersion, and the equivalent series resistance remains desirably low (light red in **Fig. 3.7d** and **Fig. 3.7e**, ~75 Ω). The good water resistance capabilities can be the reliable sealing through adhesive between the PET cover and the Mylar foundation layers. Such encapsulation condition serves as an effective barrier for both inward water permeation and outward electrolyte diffusion. All the above testing results proves that the supercapacitor units in WSSC has better electrochemical performances over regular LIG-based micro-supercapacitors, as well as quite reliable water resistance capabilities.

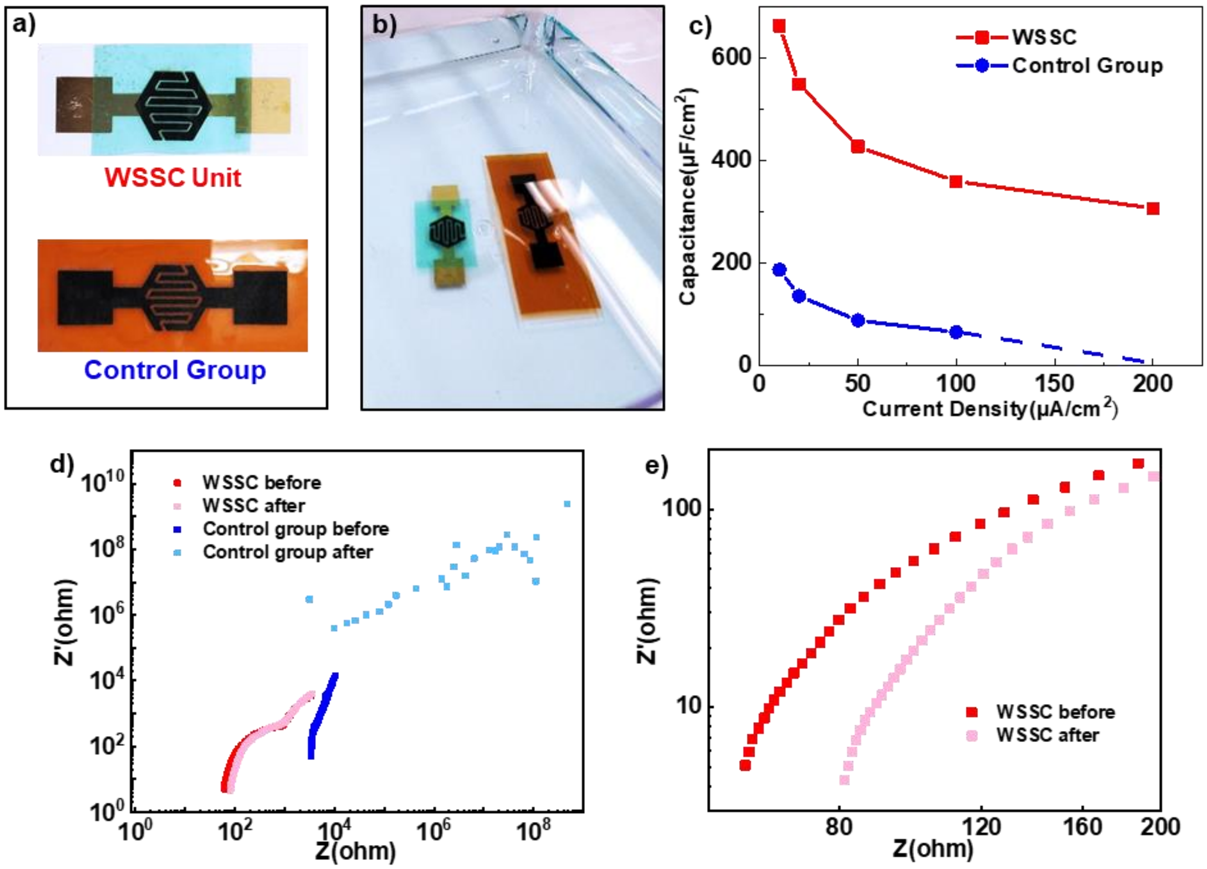

Figure 3.7 *Electrochemical and water resistivity evaluations of one WSSC unit.* ***(a-b)*** *Optical images of one WSSC unit and a control group sample (a) in top views and (b) immersed in water.* ***(c)*** *Areal capacitance vs. discharge current density for one WSSC unit and the control group sample.* ***(d-e)*** *Nyquist plots of one WSSC unit and the control group sample before and after 16-hour water immersion.*

While the stacking of multiple material layers is the key to WSSC's good electrochemical performances and desirable water resistance features, the overall thickness of our WSSC remains small (~9 μm). This small-thickness and rationally designed planar geometries provide the overall compliant mechanics to achieve remarkable deformability. **Figures 3.8a-c** demonstrate that the WSSC can be folded reversibly to half (**Fig. 3.8b**) or to one-sixth (**Fig. 3.8c**) of its initial nominal area (**Fig. 3.8a**), in a similar manner to the closing of a paper fan. The WSSC can also be stretched equi-biaxially in-plane (**Fig. 3.8d, e**) to 2.1 times of its initial area (or equivalently, 46% elongation in length), which is 1179% increase in area from its most compact configuration (**Fig. 3.8c**). Finite element analysis (FEA) predicts that the maximum principal strain in gold interconnects remains lower than the elastic limit (~0.3%) until reaching the stage in **Fig. 3.8d, e**, indicating that all these deformations are elastic and recoverable. There is remarkable agreement between the deformed geometric details predicted by FEA (**Fig. 3.8e**) and those observed in experiments (**Fig. 3.8d**). As an additional justification, the CV loop measured at equi-biaxially stretched state (red curve in **Fig. 3.8f**) overlaps very well with that recorded in the initial state (black). These results validate that the electrochemical performances of the WSSC remain unaffected under extreme deformations. This easy and reversible transformation between 1/6 and 2.1x of its initial area may have potential applications as a convenient retraction/expansion mechanism for deployable systems requiring large changes in nominal area.

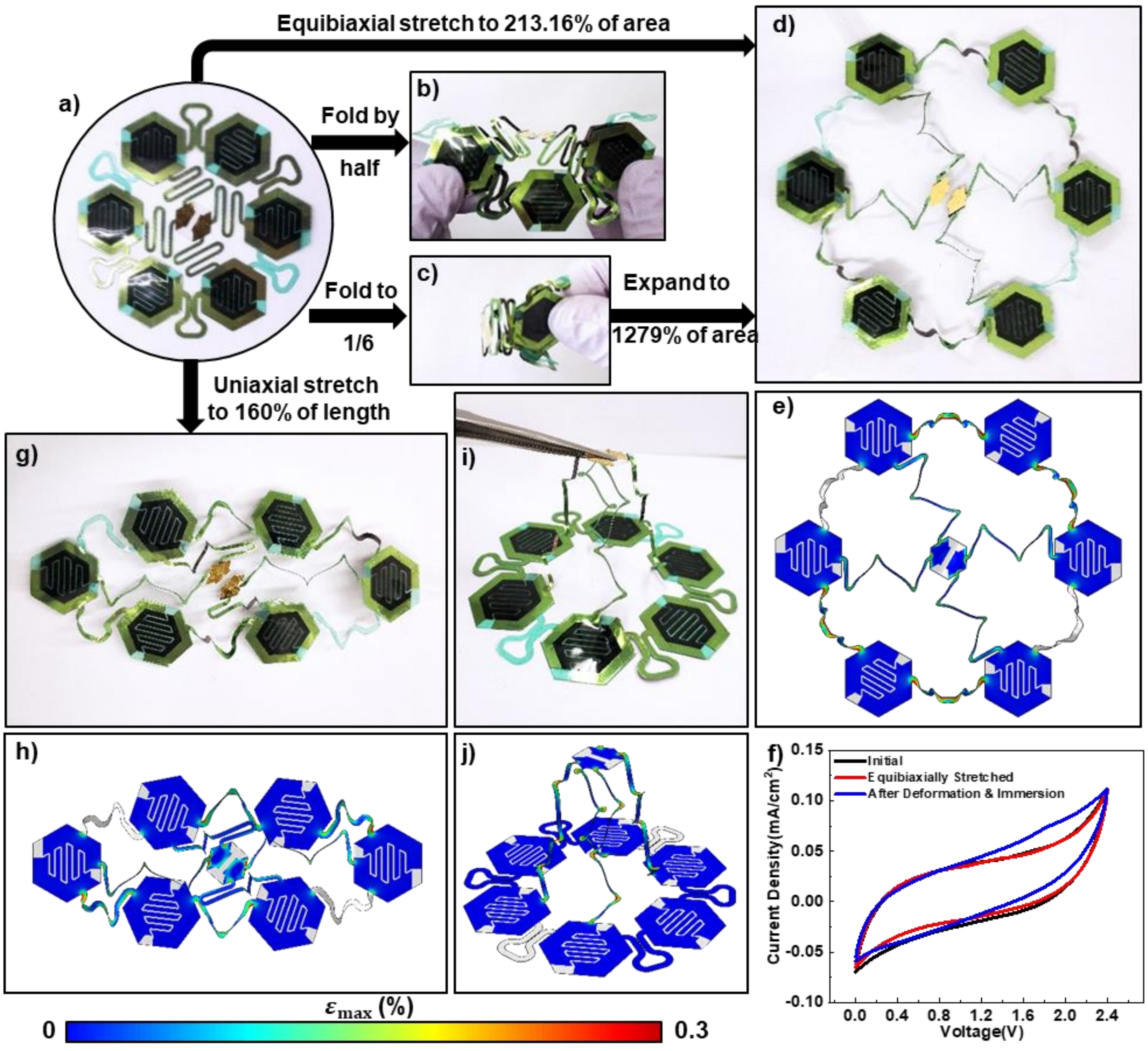

Figure 3.8 ***(a-c)*** *Optical images of WSSC (a) in its initial configuration, (b) folded by hand to half and (c) folded to 1/6 of its initial nominal area.* ***(d-e)*** *Equi-biaxial stretching of WSSC, as (d) recorded in experiments and (e) predicted by FEA.* ***(f)*** *Cyclic Voltammetry measurement of the entire device. The measurement was performed before and after repetitive deformation and extensive water immersion.* ***(g-j)*** *Uniaxial elongation (left column) and out-of-plane stretching (center column) of WSSC, as (g,i) recorded in experiments and (h,j) predicted by FEA. Color in*

FEA results denotes maximum principal strain in the layer of gold collectors and interconnects.

In addition to the aforementioned types of deformation, the WSSC can also reversibly accommodate up to 60% uniaxial elongation in the planar direction (**Fig. 3.8g, h**). Most interestingly, the hexagonal region in the center with contact electrodes can be lifted upwards (or vice versa, pressed downwards) out-of-plane to facilitate elongation in the third spatial dimension (**Fig. 3.8i, j**). Without inducing plasticity in metal, this elongation can be as high as 35.5 mm, or almost 400 times of the WSSC's initial thickness (~90 μm). In both scenarios, FEA (**Fig. 3.8h, j**) again predicts matching deformation details to experiments (**Fig. 3.8g, i**), and confirms that the strain in gold interconnects are below the elastic limit. Since the WSSC are stretchable in-plane and out-of-plane, it can be identified as an "omni-directionally stretchable" device. Notably, after a series of repeated mechanical deformations, as well as extensive water immersion experiments, the WSSC can still maintain its electrochemical performances, as indicated by the blue curve in **Fig. 3.8f**. All these results validate the mechanical and electrical stability of the WSSC.

3.2.3 Skin-Mounted Human Breathing Monitor Module

While the former device uses LIG as the active material, the fabrication scheme based on two-mode cutting process can also easily incorporate commercial off-the-shelf electronic components. **Figure 3.9a** shows the structures of a stretchable skin-mountable module for monitoring human breathing, where the circuit is encapsulated by an elastomeric substrate and superstrate. In the circuit, five small surface-mount temperature sensors (nominal area ~1.3 mm^2, TFPT0603, *Vishay Intertechnology*) are connected in series, by gold interconnects (thickness ~100 nm) on a Mylar film (thickness ~40 μm). The thin, nontoxic substrate and superstrate (thickness ~300 μm for superstrae, ~600 μm for substrate; effective modulus ~60 kPa, Ecoflex 00-30, *Smooth-On*) is softer than that of human skin (effective modulus ~130 kPa) to facilitate as an intimate, comfortable device-to-skin interface when the entire module (~50 mm by 13 mm) is applied on the face of a volunteer (**Fig. 3.9b**). While most portions of the circuit are insulated and protected from the environment by the elastomeric encapsulations, the top surfaces of temperature sensors are deliberately exposed for detecting temperature changes resulting from inhalation/exhalation conditions through the two nostrils. The sensors are spaced at 7.5 mm from each other to capture signals from the left nostril (sensors 1 and 2), right nostril (sensors 4 and 5), and from below the nasal septum (sensor 3). **Figure 3.9c** shows one periodic unit in the entire module, featuring the four serpentine-shaped interconnects (line width ~350 μm) that provide mechanical stretchabilities. Interconnect 1 is an electrical trace that joins two sensors in series, while interconnects 2 and 3 are leads to terminals for electric potential measurements. Interconnect 4 (almost invisible due to the transparent nature of Mylar films) is a wire without metal conductors for balancing mechanical loads and offering deformability.

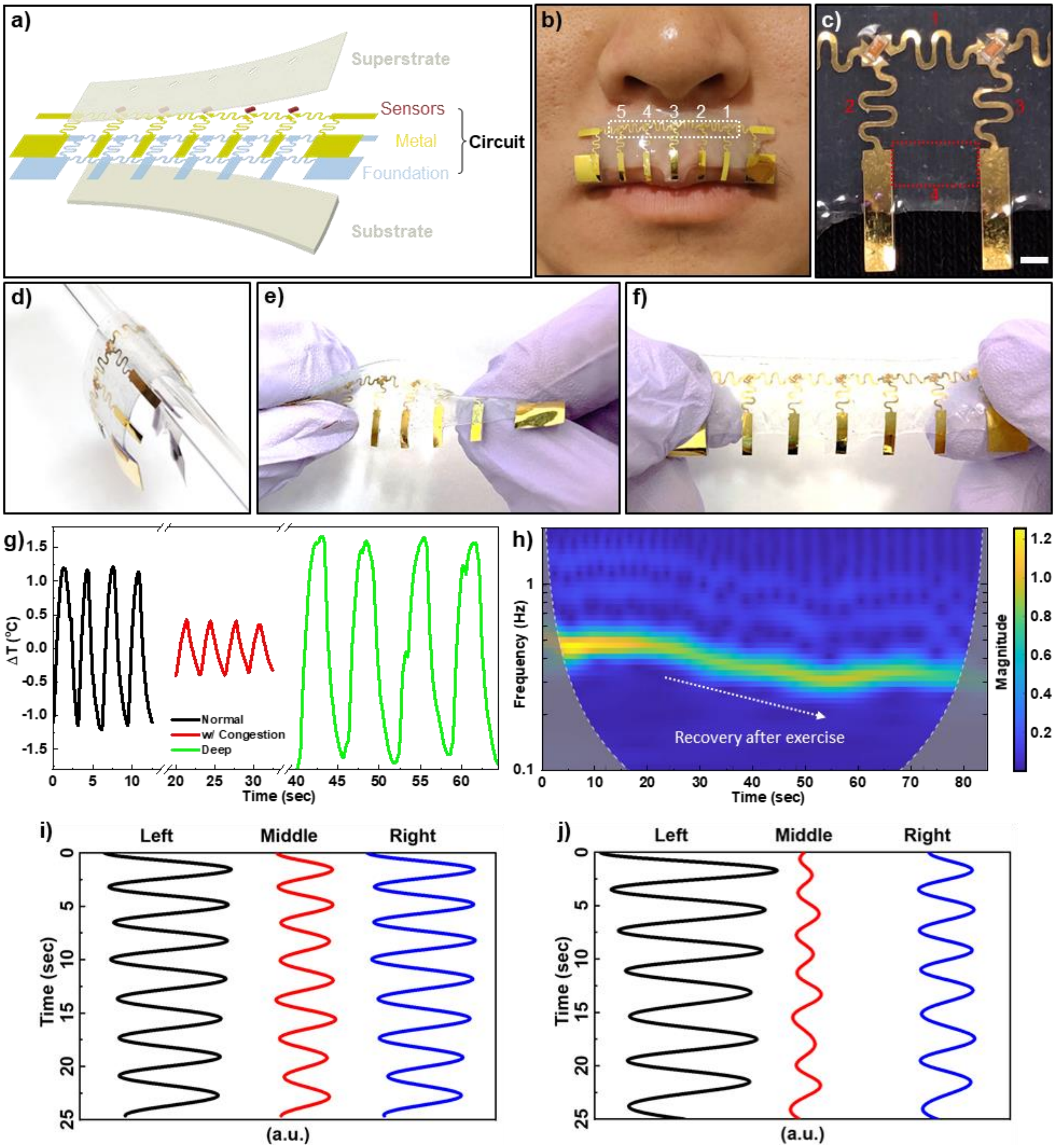

Figure 3.9 *Stretchable skin-mounted human breath monitor module.* ***(a)*** *Schematic illustration of the device.* ***(b)*** *Optical image of the device mounted on a volunteer's face.* ***(c)*** *Magnified optical image featuring one unit-cell in the device. Scale bar: 2 mm.* ***(d-f)*** *Demonstration of the device's mechanical compliance and deformability. The device can be (d) wrapped on a stirring rod, (e) twisted, and (f) stretched by hands.* ***(g)*** *The breathing patterns of a volunteer in three different scenarios.* ***(h)*** *Magnitude scalogram representation of a volunteers' breathing patterns for post-*

exercise recovery. ***(i-j)*** *Breathing signals from (i) a volunteer with symmetric nose and (j) a volunteer with nasal septum deviation, as captured by sensors at different locations.*

The module is soft and deformable overall, as it can be spontaneously wrapped on a glass stirring rod with a diameter of ~5 mm (**Fig. 3.9d**), and be reversibly twisted (**Fig. 3.9e**) and stretched (**Fig. 3.9f**) by hand. The low-modulus elastomeric encapsulations, the small overall thickness (less than 1 mm), and the serpentine-shaped interconnects design all contribute to the desirable compliant and deformable mechanics of the module. The fabrication process is illustrated in **Figure 3.10**, where "tunnel cuts" and "through cuts" are used respectively for patterning gold pads and interconnects, and for defining the outlines of the overall structure, in a similar way to the previous device (Step 1 to 5). Afterwards, the Mylar foundation layer with gold patterns is transferred to a 0.6 mm-thick Ecoflex substrate (1:1 mix ratio of liquid A and B, cured; Step 6) and bonded with five temperature sensors with conductive adhesive (8331, *MG Chemicals*; Step7). Finally, liquidous Ecoflex (1:1 mix ratio of liquid A and B, uncured) is carefully applied and cured to form the substrate, with only the top surfaces of sensors exposed (Step 8) to complete the device.

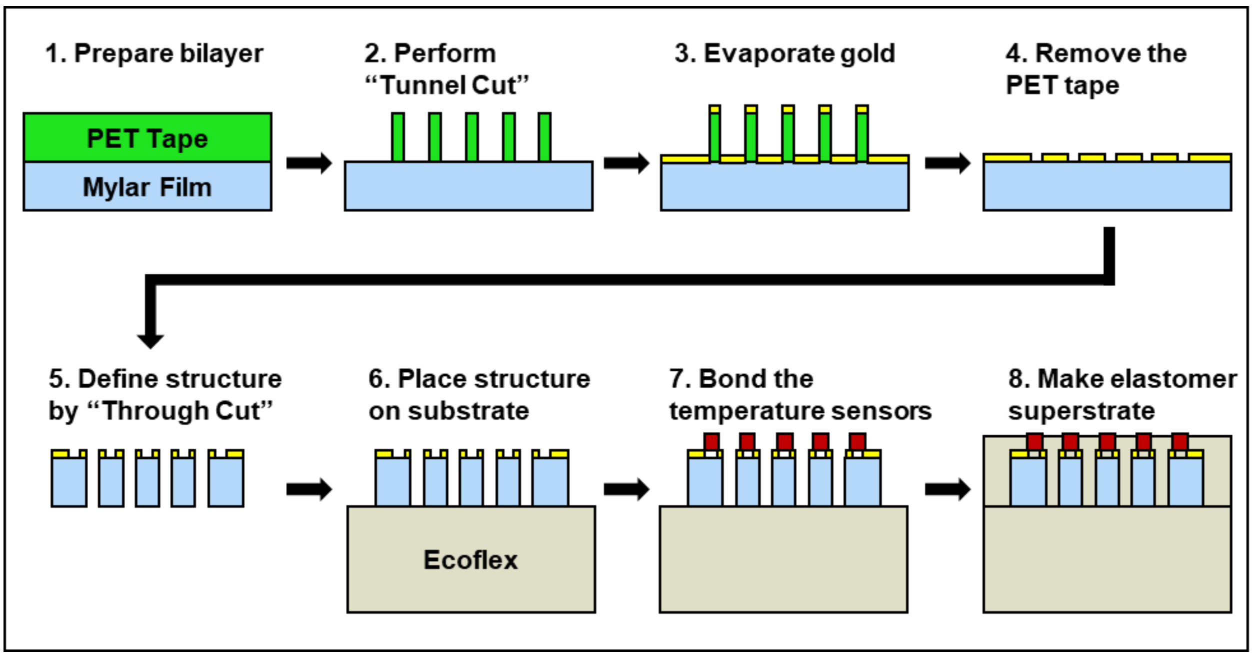

Figure 3.10 *Fabrication processes for the stretchable skin-mounted breath monitor module using two-mode mechanical cutting.*

This time-saving and cost-effective fabrication approach is especially suitable for the research and prototyping of the wearable breathing monitoring module, and many other time-sensitive electronics devices for biomedical applications. Monitoring breathing patterns is helpful for the diagnoses and treatments of many diseases, including asthma, obstructive sleep apnea (OSA), and pneumonia, etc [19-23]. In the current year with the COVID-19 pandemic, nasal congestions, shortness of breath and sudden change in breathing patterns are common symptoms to watch for suspected infections [24-26]. Apart from biomedical applications, tracking of breathing can also be used in the training of athletes [27]. Many features in human breathing can be captured by this wearable monitoring module.

Figure 3.9g shows the breathing patterns (reflected by temperature changes) from the right nostril of a healthy 26 year-old male volunteer, as recorded by Sensor 5 in the module. In a normal condition (black curve), the volunteer completes four cycles of nasal breathing in 12.5 seconds, corresponding to a respiratory frequency of 0.32 Hz. In each cycle, the temperature on the sensor increases during exhalation (because of the heat coming with the exhaled airflow) and decreases during inhalation (because of enhanced convection of ambient air on the sensor surface). The amplitude of temperature variation is ~2.4 ℃. When this nostril is pressed moderately by finger to represent single-side nasal congestion, the exhalation/inhalation events through this nostril are notably reduced, and volunteer has to breathe mainly through the other (i.e., left) side. Results (red curve) show that the amplitude of temperature variation is reduced to only one-third (~0.8 ℃), while the changes in respiratory frequency is not significant. The recorded temperature variation is likely contributed mostly by the airflow from/into the other nostril. Finally, the volunteer is requested to perform long, deep breathing (green curve), as characterized by the almost twice as long cycles (6.1 second per cycle, frequency ~0.16 Hz), and larger temperature variation (~3.6 ℃) in each cycle. In another experiment, we track on Sensor 5 the breathing pattern of the same volunteer during his recovery from a mild physical exercise session, and convert the results to a magnitude scalogram in **Fig. 3.9h**. During the eighty-five-second recovery process, the volunteer's breathing gradually changes from rapid and heavy to peaceful and steady, as evidenced by the shifting of respiratory frequency from ~0.5 Hz to ~0.3 Hz, and the dimming colors representing the magnitude of breathing.

By connecting the five sensors in series and reading signals from each sensor, we can evaluate the symmetry (or asymmetry) of breathing patterns. Asymmetric breathing, as characterized by one nostril having much stronger airflow than the other, is a common symptom related to nasal septum deviation, common cold, sinusitis, or nasal polyposis, etc. In our experiments, we record on the breathing monitor module the breathing patterns from two volunteers, one (27 year-old male, Volunteer A) breathing symmetrically (**Fig. 3.9i**), and another (24 year-old male, Volunteer B) with nasal septum deviation (**Fig. 3.9j**). The signals corresponding to the left and right nostrils are computed as the average of data recorded on Sensor 1 and 2, and Sensor 4 and 5, respectively, while Sensor 3 right below the volunteer's nasal septum yields results for the "middle" location in **Fig. 3.9i, j**. We can clearly observe the differences between the two volunteers: while the breathing signals from left and right nostrils have comparable amplitudes for Volunteer A, Volunteer B has stronger airflows through his left nostril (evidenced by higher amplitude) than those from his right nostril. On the "middle" sensor, Volunteer B has smaller breathing amplitude than Volunteer A, likely because the airflow dominantly from one nostril results in weaker convection on the sensor's top surface, when compared with symmetrical airflows. In addition to the aforementioned measurements, the skin-mountable breathing monitor module can also be used for mapping airflow velocity and estimating thoracic pressure changes over breathing cycles, as well as for identifying apnea, hypopnea, and polypnea during sleep, following recently reported studies [28].

3.3 Materials and Methods

3.3.1 Electrochemical Testing of WSSC

The electrochemical performances of WSSC and control group samples were measured on an electrochemical workstation (*Gamry Reference 600*) via CV, GCD, and EIS tests. For CV tests, the potential window was chosen as 0.8 V for one unit, and 2.4 V for the entire device. The areal capacitance C_A is calculated from the GCD test as $C_A = I\Delta t/\Delta VA$, where I is the discharge current, Δt is the discharge time, A is the nominal area of electrodes, and ΔV is the potential window during the discharge, excluding the voltage drop. The real and imaginary parts of impedance (Z and Z') were recorded during EIS tests, over a frequency range between 0.1 Hz and 10^5 Hz.

3.3.2 Testing of Breath Monitor Module

Measurements using a single sensor were conducted on an electrochemical workstation (*Gamry Reference 600*), in constant current mode (100 μA). Measurements requiring five sensors in series were performed by using a multi-channel data acquisition module (*National Instruments USB-6341*), with each channel capturing the electric potential drop across one sensor. A precision current source (*Keithley 6220*) was used to provide a constant current (1 mA).

3.3.3 Finite Element Analyses

3D FEA simulations were performed using a commercial simulation software (ABAQUS). As an example, FEA simulations are used for the study of WSSC, in both predicting deformed geometric details and reversible stretchability values. Implicit static analyses with displacement control are used in all analyses. The WSSC was modeled with quadrilateral shell elements (S4R) with laminate composite properties. For different regions in the device, the "Composite Layup" function was used to correctly define the thicknesses and properties of materials of each constituting layers. The most complex region is defined by five layers, from bottom to top as:

Mylar (40 μm), gold (100 nm), PVA electrolyte + LIG (10 μm), adhesive (15 μm), and PET (25 μm). Gold (E = 78 GPa, ν = 0.44, elastic limit = 0.3%) is modeled as an elastic-perfectly-plastic material to predict reversible stretchability. Reversible stretchability is defined as the overall elongation of the structure when the maximum principal strain in metal reaches elastic limit for no less than one-half of the width of interconnects. PET (E = 4 GPa, ν = 0.4), adhesive (E = 20 MPa, ν = 0.475) and PVA electrolyte + LIG (E = 20 MPa, ν = 0.475) are modeled as linear elastic materials to account for their contributions to the overall structural stiffness. Because "Mylar" is a type of PET, the Mylar film is modeled with the mechanical properties of PET.

3.4 Conclusions of Chapter 3

This chapter presents a low-cost, time-saving fabrication scheme for stretchable electronics systems with multiple patterned layers and complex geometric details, without the need of photolithography-based processes or access to cleanroom environment. The two cutting modes used for patterning of each material layer, namely "tunnel cut" and "through cut", are the core of this fabrication process. This desirable effect of two-mode mechanical cutting is achieved by tuning the level of force and depth of blade on an affordable, desktop-sized vinyl cutter. Two devices have been fabricated to demonstrate the capabilities of the proposed methods: a water resistant, omni-directionally stretchable supercapacitor patch, and a compliant, skin-mounted human breath monitoring module. Both devices enjoy compliant mechanics, and can maintain stable electrical functionalities after large deformations. Apart from the two devices reported here, we believe this fabrication method based on two-mode mechanical cutting can provide the cost-effective and time-effective way for many other stretchable electronics and bioelectronics systems, especially in the design iteration and prototyping stages.

References of Chapter 3

[1] J. A. Rogers, T. Someya, and Y. Huang, "Materials and mechanics for stretchable electronics," *Science,* vol. 327, no. 5973, pp. 1603-1607, 2010.

[2] M. L. Hammock, A. Chortos, B. C. K. Tee, J. B. H. Tok, and Z. Bao, "25th anniversary article: the evolution of electronic skin (e-skin): a brief history, design considerations, and recent progress," *Advanced Materials,* vol. 25, no. 42, pp. 5997-6038, 2013.

[3] Y. Liu, M. Pharr, and G. A. Salvatore, "Lab-on-skin: a review of flexible and stretchable electronics for wearable health monitoring," *ACS Nano,* vol. 11, no. 10, pp. 9614-9635, 2017.

[4] W. Gao, H. Ota, D. Kiriya, K. Takei, and A. Javey, "Flexible electronics toward wearable sensing," *Accounts of chemical research,* vol. 52, no. 3, pp. 523-533, 2019.

[5] K.-I. Jang *et al.*, "Rugged and breathable forms of stretchable electronics with adherent composite substrates for transcutaneous monitoring," *Nature Communications,* vol. 5, no. 1, pp. 1-10, 2014.

[6] D. Son *et al.*, "Multifunctional wearable devices for diagnosis and therapy of movement disorders," *Nature Nanotechnology,* vol. 9, no. 5, p. 397, 2014.

[7] S. Xu *et al.*, "Soft microfluidic assemblies of sensors, circuits, and radios for the skin," *Science,* vol. 344, no. 6179, pp. 70-74, 2014.

[8] J. W. Lee *et al.*, "Soft, thin skin-mounted power management systems and their use in wireless thermography," *Proceedings of the National Academy of Sciences,* vol. 113, no. 22, pp. 6131-6136, 2016.

[9] R. Xu *et al.*, "Designing thin, ultrastretchable electronics with stacked circuits and elastomeric encapsulation materials," *Advanced Functional Materials,* vol. 27, no. 4, p. 1604545, 2017.

[10] S. I. Park *et al.*, "Soft, stretchable, fully implantable miniaturized optoelectronic systems for wireless optogenetics," *Nature Biotechnology,* vol. 33, no. 12, pp. 1280-1286, 2015.

[11] S. Wang *et al.*, "Skin electronics from scalable fabrication of an intrinsically stretchable transistor array," *Nature,* vol. 555, no. 7694, pp. 83-88, 2018.

[12] Y. Liu *et al.*, "Soft and elastic hydrogel-based microelectronics for localized low-voltage neuromodulation," *Nature Biomedical Engineering,* vol. 3, no. 1, pp. 58-68, 2019.

[13] L. Tian *et al.*, "Large-area MRI-compatible epidermal electronic interfaces for prosthetic control and cognitive monitoring," *Nature Biomedical Engineering,* vol. 3, no. 3, pp. 194-205, 2019.

[14] K. Lee *et al.*, "Mechano-acoustic sensing of physiological processes and body motions via a soft wireless device placed at the suprasternal notch," *Nature Biomedical Engineering,* vol. 4, no. 2, pp. 148-158, 2020.

[15] J. Liu *et al.*, "Intrinsically stretchable electrode array enabled in vivo electrophysiological mapping of atrial fibrillation at cellular resolution," *Proceedings of the National Academy of Sciences,* vol. 117, no. 26, pp. 14769-14778, 2020.

[16] S. Yang *et al.*, "“Cut-and-paste” manufacture of multiparametric epidermal sensor systems," *Advanced Materials*, vol. 27, no. 41, pp. 6423-6430, 2015.

[17] S. Kabiri Ameri *et al.*, "Graphene electronic tattoo sensors," *ACS Nano,* vol. 11, no. 8, pp. 7634-7641, 2017.

[18] B. Sadri, D. Goswami, and R. V. Martinez, "Rapid fabrication of epidermal paper-based electronic devices using razor printing," *Micromachines*, vol. 9, no. 9, p. 420, 2018.

[19] R. R. Watkins and T. L. Lemonovich, "Diagnosis and management of community-acquired pneumonia in adults," *American Family Physician,* vol. 83, no. 11, pp. 1299-1306, 2011.

[20] P. Jiang, S. Zhao, and R. Zhu, "Smart sensing strip using monolithically integrated flexible flow sensor for noninvasively monitoring respiratory flow," *Sensors,* vol. 15, no. 12, pp. 31738-31750, 2015.

[21] T. J. Vaessen, S. Overeem, and M. M. Sitskoorn, "Cognitive complaints in obstructive sleep apnea," *Sleep Medicine Reviews,* vol. 19, pp. 51-58, 2015.

[22] K. Meng *et al.*, "A Wireless Textile-Based Sensor System for Self-Powered Personalized Health Care," *Matter,* 2020.

[23] Z. Zhou *et al.*, "Single-layered ultra-soft washable smart textiles for all-around ballistocardiograph, respiration, and posture monitoring during sleep," *Biosensors and Bioelectronics*, vol. 155, p. 112064, 2020.

[24] T. Greenhalgh, G. C. H. Koh, and J. Car, "Covid-19: a remote assessment in primary care," *BMJ,* vol. 368, 2020.

[25] G.-u. Kim *et al.*, "Clinical characteristics of asymptomatic and symptomatic patients with mild COVID-19," *Clinical Microbiology Infection,* 2020.

[26] A. Lovato and C. de Filippis, "Clinical presentation of COVID-19: a systematic review focusing on upper airway symptoms," *Ear, Nose and Throat Journal,* p. 0145561320920762, 2020.

[27] A. Nicolò, C. Massaroni, and L. Passfield, "Respiratory frequency during exercise: the neglected physiological measure," *Frontiers in Physiology,* vol. 8, p. 922, 2017.

[28] T. Jiang *et al.*, "Wearable breath monitoring via a hot-film/calorimetric airflow sensing system," *Biosensors and Bioelectronics,* p. 112288, 2020.

Chapter 4: Soft Actuators with Bioinspired Flesh-and-Bone Constructs

4.1 Introduction

Studies in soft actuators have drawn widespread attentions in recent years [1-3]. Compared with hard-bodied actuators using rigid links and joints, soft and compliant systems can change their shapes to adapt to the external environment, and offer harmless mechanical interfaces between human and machine. These unique features make them desirable candidates for applications ranging from wearable devices, to *in-vivo* biomedical systems, to the dexterous manipulation of delicate objects. Many application scenarios requires the actuator to operate remotely without wires (thus, untethered) in order to accommodate the twists and turns of its surroundings. Reported untethered soft actuators are made of active polymeric materials, including hydrogels, liquid crystal elastomers (LCE), and shape memory polymers (SMP), with their motions stimulated by light, heat, or chemical changes [4-14]. These polymers have the desirable soft and compliant mechanics but they usually need a long time to actuate with limited precision when compared to their traditional hard-bodied counterparts. These two drawbacks are attributed to the nature of their actuation mechanisms: Specifically, the swelling/shrinking mechanism for hydrogels, the heat-induced thermal expansions and deformations for shape memory polymer, and the responses of liquid crystal elastomers to external stimuli, are all based on physical or chemical processes that require substantial amount of time (typically several seconds to hundreds of seconds). The precision of actuation in these processes are also compromised due to fluctuations of the external stimuli and changes in the surrounding environment.

Magnetic actuators, on the other hand, have fast responses with excellent precisions and good untethered controllability in a confined space, but most of the previous studies have focused on actuators with rigid structures [15, 16]. In the recent two years, researchers have reported soft and magnetically controlled actuators across various length scales by embedding ferromagnetic particles with controlled directional magnetization in elastomeric matrices [17, 18]. These actuators have achieved the desirable fast actuation with compliant mechanics but their fabrication processes have been rather complex, including highly-specialized equipment such as a direction-specific 3D printer with accurately timed magnetization function or a special lithography platform with on-site magnetization. In this work, we propose and build high performance magnetically powered soft actuators through structural innovations using easily accessible experimental setups and low-cost, commercially available materials to accomplish the simple and fast fabrication process.

4.2 Results and Discussion

4.2.1 A Bioinspired Flesh-and-Bone Construct

Biology provides the good inspiration for solving challenging design problems and a human arm is a good example. Specifically, the rotation of “bones” in the arm facilitate the accurate motions such as flexion and extension, while the “flesh” (including muscles, fat, tendons and skins) encapsulates the bones to protect the brittle bones from mechanical impacts. Moreover, the soft mechanics of flesh also offers a compliant interface when interacting with the surrounding environment (**Fig. 4.1a**). Here, our soft actuators are constructed by integrating two off-the-shelf materials of very different mechanical properties: (1) rigid NdFeB magnets (cylindrical shape, millimeter scale), and (2) highly deformable elastomers (Ecoflex 00-35). When the actuator is placed in an external magnetic field with a field strength, $\mathbf{B}$, (**Fig. 4.1b**), an aligning torque $\boldsymbol{\tau} = \mathbf{m} \times \mathbf{B}$ is generated on the magnetic “bones” with a magnetic moment, $\mathbf{m}$, the entire flesh-and-bone structure actuates in a similar way to the flexion of a human arm. **Figures 4.1c,** and **4.1d** show the resemblances of mechanical properties between the human arm and our actuator. In both cases, the “bones” have high moduli (Effective Modulus ~18 GPa for real bones, ~100 GPa for NdFeB bones) yet brittle mechanics (elongation at break ~1.43% for real bones, 0.15% for NdFeB bones), while the “flesh” is soft and resilient (for real flesh: Modulus ~20 kPa, elongation at break ~30%; for Ecoflex flesh: Modulus ~166 kPa, elongation at break ~500%) [19-23]. The flesh-and-bone construct facilitates an effective separation of tasks based on the distinct mechanics of components, where the hard “bones” enable quick and precise motions and the soft “flesh” accommodates the large strains during actuation and alleviates mechanical impacts away from the brittle “bones”.

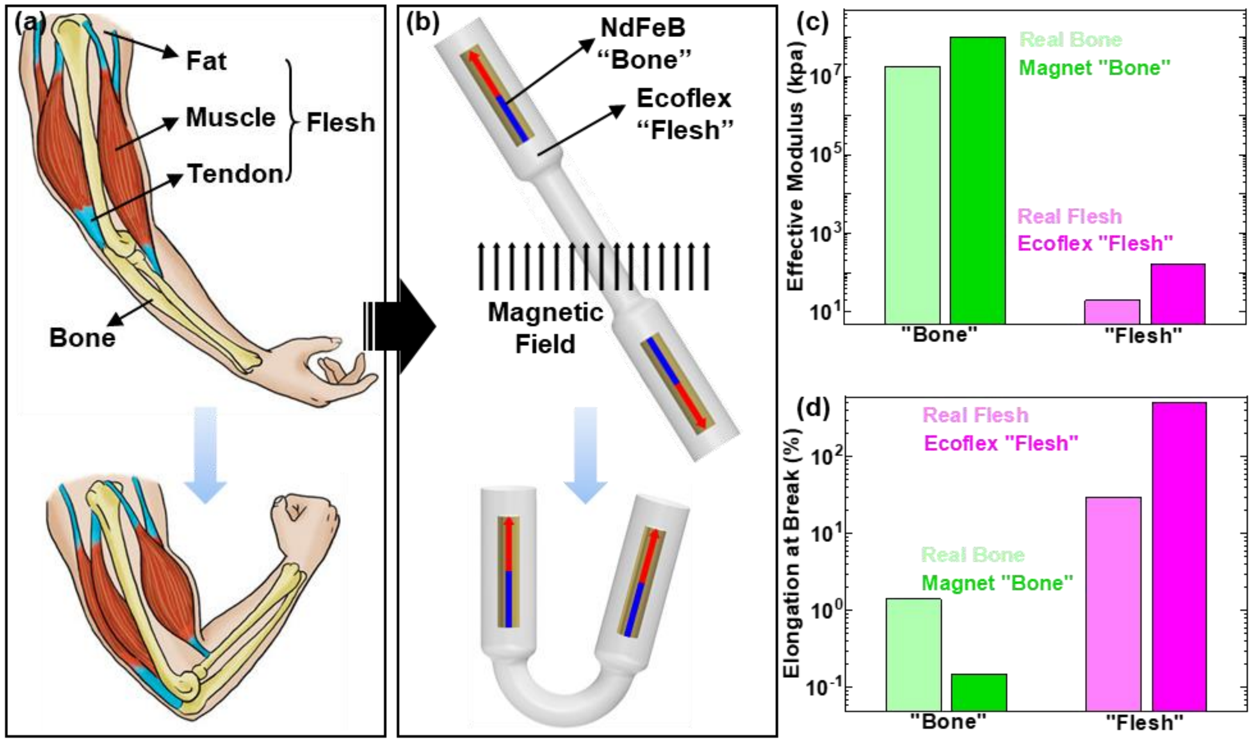

Figure 4.1 *(a) The flexing of a human arm, featuring the bones and flesh components. **(b)** Schematics of the working mechanism of a bioinspired bone-and-flesh actuator, with magnets as “bones” and elastomers as “flesh”. **(c)** Effective modulus, and **(d)** deformability (evaluated by the amount of elongation at break) of “bone” and “flesh” components in human body and in the proposed actuators.*

To evaluate the agility of the flesh-and-bone actuators, a prototype sample is placed in an alternating magnetic field (**Fig. 4.2a**). The magnet as the “bone” will align its polarity with the alternating field, leading the entire structure to deform periodically, as recorded by a video camera at 240 frames per second. As shown in **Fig. 4.2b**, the actuator can catch up with the alternating field as the driving frequency increases to 50 Hz, indicating that the typical response time is less than 0.02 seconds. Above 50 Hz, this measurement is limited by the frame rate of the video camera. The full actuation time (defined as the duration for switching between the initial and the fully deformed configurations) of the flesh-and-bone actuators is between 0.1 and 0.6 seconds, under a constant magnetic field. This actuation time is comparable to reported magnetic soft actuators fabricated by complex procedures, and about 10 to 1,000 times shorter than representative untethered bending-type soft actuators of similar length scales (centimeters in span, smallest thickness ~1 millimeter) that are made of liquid crystal elastomers, hydrogels, and shape memory polymers (**Fig. 4.2c**) [4-14, 17].

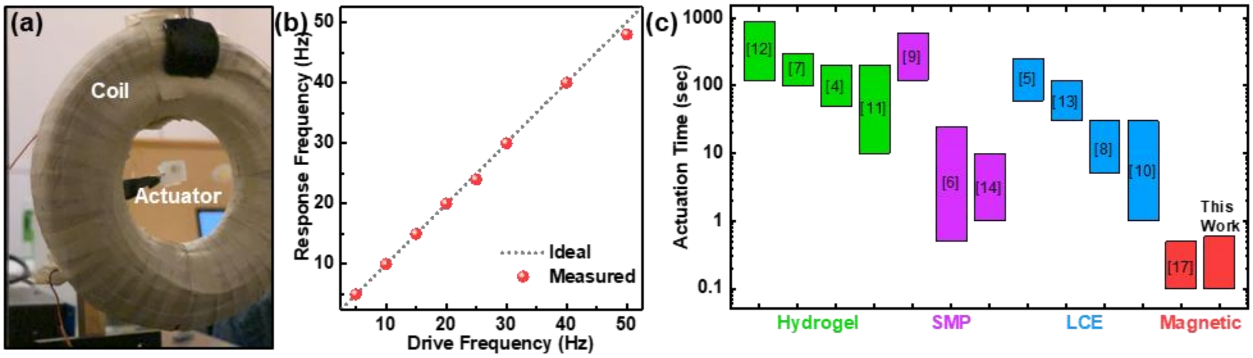

Figure 4.2 ***(a)*** *Experimental setup for testing an actuator's response under an alternating magnetic field.* ***(b)*** *Response vs. drive frequency of an actuator, as read from video images at 240 frames/sec.* ***(c)*** *Comparison in actuation time between magnetically powered soft actuators and actuators of similar length scale but using other working mechanisms. The numbers in the square brackets denote the corresponding references.*

A drop-shock test to characterize the survivability of the system upon impact has been designed. Samples of one column-shaped magnetic "bone" with and without the encapsulated Ecoflex "flesh" have been tested with free falls from a height of 1.3 meters on to a rigid ground made of quartz. **Figures 4.3a** and **4.3b** show the time sequence images recorded by a video camera at 240 frames per second, with the first image in each series corresponding to the initial (first) impact between the sample and the ground. Since both samples collide with the ground with an initial angle, the sample will rotate about its center of mass with accelerated angular velocity to have a second impact with the ground. The brittle magnetic "bone" is most susceptible to failure during these two major impacts, especially the second impact with potentially even higher velocity than the first. The bare magnet in the control group is found to easily crack into two pieces immediately during the initial impact (**Fig. 4.3b**). The magnetic "bone" encapsulated by Ecoflex "flesh" survives both the first and second impacts (**Fig. 4.3a**) and remains intact when all events come to rest, as shown by the inset of **Fig. 4.3a**.

Dynamic finite element analyses (FEA) help us interpret the results of the above experiments, and quantitatively show how the elastomeric "flesh" accommodates mechanical impact and prevents failure. These FEA studies follow the initial velocity and angle of collision to closely match experimental setups (**Fig. 4.4a, b**) in order to closely capture the details and characteristics of the two major impact events (**Fig. 4.4c**). In the case with the "flesh" encapsulation, FEA results indicate that the peak force on the magnetic "bone" is only ~1.1 N during both impacts, and that the elastic strain energy in the "bone" is ~0.8 μJ and ~1.17 μJ during the first and second impact, respectively (**Fig. 4.3c, d**). This is a remarkable reduction by ~98.5% in force, and ~99.7% and ~99.6% in strain energy, when compared to those of the control group without the "flesh", during the first impact (~72 N and ~0.27 mJ). FEA also predicts that even if the bare magnet survived the initial impact, it could still crack during the second impact with even higher force (~95 N) and strain energy (~0.533 mJ). **Figure 4.3e** shows the maximum principal strain on the magnet after impact(s). As expected, the strain on the magnetic "bone" remains low after both impacts when protected by the elastomeric "flesh", while the strain in the control group without the "flesh" does exceed the fracture limit (~0.15%) considerably after the first impact, hence failure is expected to occur. To further understand how the elastomeric "flesh" protects the brittle "bone" against the mechanical impact, the distribution of force and energy is plotted in **Figs. 4.4d** and **4.4e**, respectively. During impacts, only ~1/4 of the total force in a flesh-and-bone sample is endured by the "bone", and less than ~0.018% of the initial kinetic energy is converted to the strain energy on the "bone". The elastomeric "flesh", on the other hand, accommodates up to ~41% of the initial kinetic energy by its internal elastic deformation, which is more than 2,200 times higher than that of the "bone" structure to effectively protect the "bone" (and the entire structure) against failure due to mechanical impacts.

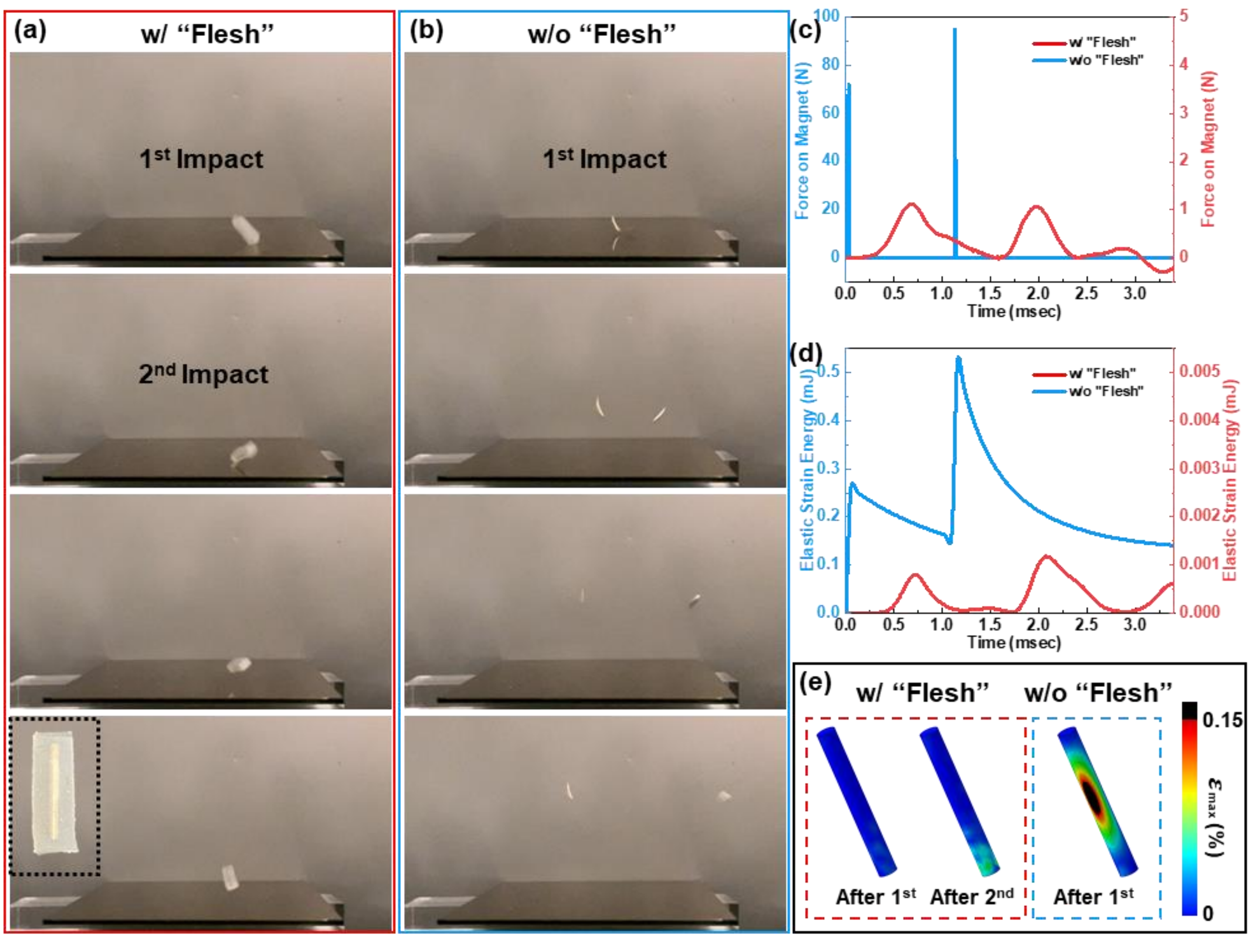

Figure 4.3 *(a-b) Recorded sequence images during a free-fall drop test, for a column-shaped magnet (a) with and (b) without the encapsulating elastomeric "flesh". The inset in (a) shows the intact structure after the test. **(c)** Force on magnet and **(d)** elastic strain energy in the magnet*

during the impact with the ground, as computed by FEA. ***(e)*** *Maximum principal strain distribution on the magnet (with or without "flesh") after impact(s), as computed by FEA.*

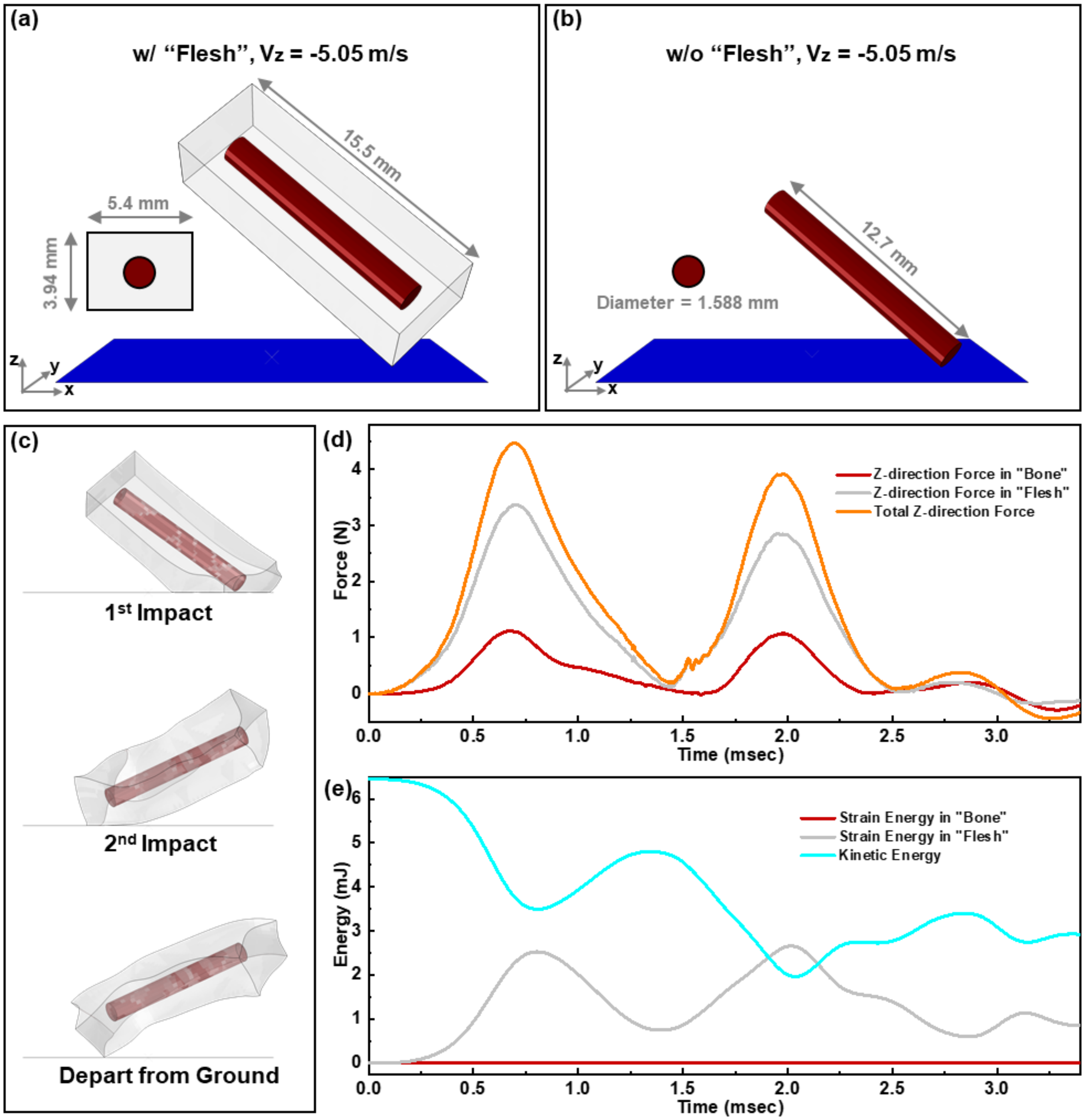

Figure 4.4 ***(a-b)*** *Schematics of the free-fall drop test and FEA simulations, for a column-shaped magnet (a) encapsulated with elastomeric "flesh" and (b) without "flesh".* ***(c)*** *Sequence images from FEA, showing the bone-and-flesh structure's 1st and 2nd impact, and eventual departure from the ground.* ***(d)*** *Force and* ***(e)*** *kinetic and elastic strain energy during the impacts with ground, as calculated from FEA.*

The flesh-and-bone construct also uses a much simpler fabrication process. This process does not need specialty tools for patterning with directional magnetization. Instead, only a standard FDM 3D printer (*Stratasys Dimension*) and affordable, off-the-shelf materials (ABS filaments, Ecoflex 00-35, and neodymium magnets of various sizes and grades) are used throughout the fabrication process. First, an ABS part is printed on the 3D printer, and serves as the mold (**Fig. 4.5a**). The protrusions in the mold will form the slots for magnet insertions in a later step. Then, Ecoflex is poured into the mold in the liquid state, and cured at room temperature to form the "flesh" part of the actuator (**Fig. 4.5b**). Finally, several cylindrical NdFeB magnets with chosen polarities are inserted into the predesigned slots to act as "bones", and sealed by Ecoflex (**Fig. 4.5c**). This completes the fabrication before the tests under an external magnetic field (**Fig. 4.5d**). Interestingly, this strategy of integrating soft and hard materials for achieving simultaneously high performance, deformable mechanics and simplified fabrication is also analogous to the popular constructs in stretchable electronics, where rigid electronics components are combined with structurally compliant interconnects and soft encapsulation materials [24, 25].

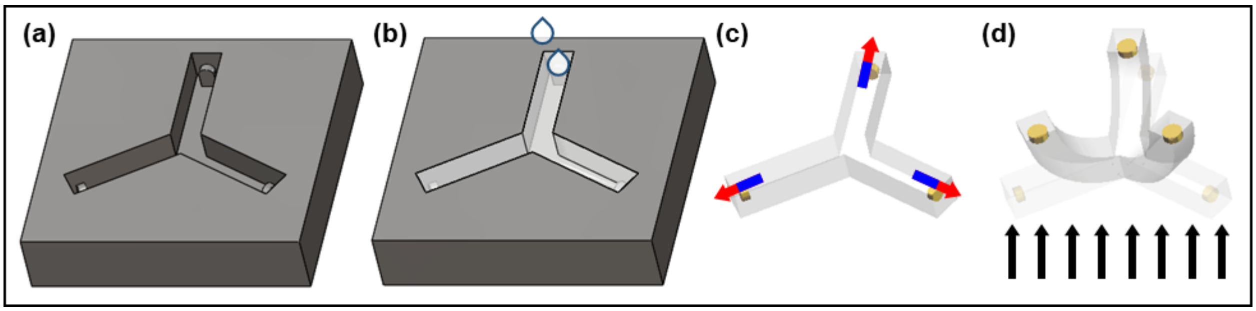

Figure 4.5 *Fabrication procedures of bone-and-flesh soft actuators.* ***(a)*** *3D print ABS molds.* ***(b)*** *Fill the printed mold with Ecoflex and cure in room temperature.* ***(c)*** *Place and seal NdFeB magnets into selected sites.* ***(d)*** *Test and actuate the device under an external magnetic field.*

In the following sections, four classes of actuators all with flesh-and-bone constructs have been designed for various tasks. In these actuators, the rotation of "bones" in the magnetic field initiates and powers the actuation, while the compliant "flesh" with carefully engineered structures changes shape accordingly and completes the tasks involving large overall deformations. The first three classes of actuators utilize recent advances in mechanics and metamaterials, including auxeticity, 2D-to-3D transformation, and bistable/multistable structures, while the last actuator (a soft gripper) targets practical applications.

4.2.2 Actuators for Auxetic Contraction and Expansion

Auxeticity, or the property of having a negative Poisson's ratio, is a hot research topic in mechanical metamaterials. Reported auxetic structures are usually connected by tubes or adhesives to mechanical stimuli such as pneumatic pressure changes or uniaxial loading to achieve large changes in their nominal area or volume during their actuations [26-29]. Here, we present devices for auxetic actuation in an untethered manner with fast responses.

Figures 4.6a and **4.6d** show the structures of two actuators with "flesh" (semitransparent) and "bones" (in golden metallic color) for two-dimensional (2D) auxetic actuations, in top and side views, with the highlighted blue and red arrows pointing from the south to the north pole inside each magnetic "bone". Both actuators have width and length of 3 cm, and a thickness of ~ 1 cm. In the structured, elastomeric "flesh", the device for the contraction motion (**Fig. 4.6a**) has four large circular holes near the center and several peripheral semi- and quarter- circular features, while the device for expansion motion (**Fig. 4.6d**) has alternating horizontal and vertical slots through its thickness. When an external magnetic field (~200 mT, denoted by black arrows) is applied, the magnetic "bones" with polarities offset from the applied field will rotate by 45 degrees under the aligning torque, causing the deformation of the structured "flesh". In the actuator for contraction, the four circular holes are gradually squeezed into alternately arranged ovals, and later dumbbell shapes, letting the entire structure reduce its nominal area within 0.2 seconds (**Fig. 4.6b**). Over the actuation process, the lengths in both planar directions (X and Y) shrink simultaneously by 18.5%, hence yielding a negative Poisson's ratio of around -1 (**Fig. 4.6c**). The total reduction in the nominal area is ~33%. In another device driven by the 45-degree rotation of magnetic "bones", the slender slots in the elastomeric "flesh" are stretched into alternately arranged rhombic voids within 0.3 seconds, such that the nominal area of the actuator is enlarged by ~53% (**Fig. 4.6e, f**). The lengths in both X and Y are increased by ~24%, again indicating the 2D auxetic nature of this actuation process. For both actuators, the deformations predicted by FEA match those observed in experiments, not only in visual features (**Fig. 4.6b, e**), but also in the quantitative quantities (**Fig. 4.6c, f**). This good agreement validates the FEA models, and establishes their utility in the design and analysis of other, more complex flesh-and-bone actuators.

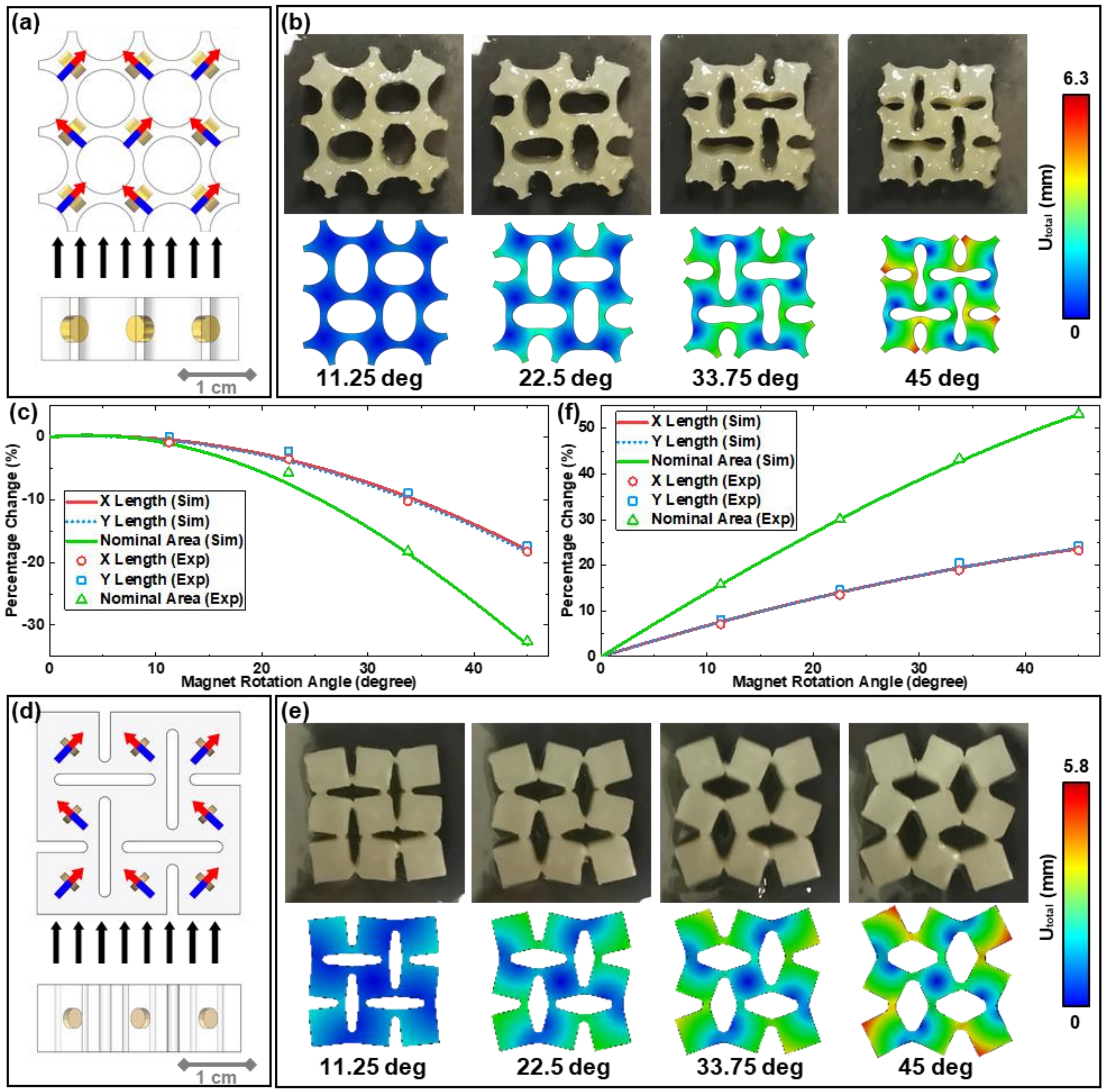

Figure 4.6 ***(a)*** *Schematics of a soft actuator for 2D auxetic contraction, in top and side views. The red/blue arrows denote the polarity of magnets, and the 1cm scale bar shows the overall dimensions of the actuator.* ***(b)*** *Recorded (top row) and computed (bottom row) deformation of the actuator, during four representative stages.* ***(c)*** *Percentage decrease in lengths and nominal area vs. the rotation angle of magnets during the contraction actuation, as predicted by FEA (lines) and measured in experiments (dots).* ***(d)*** *Schematics of a soft actuator for 2D auxetic expansion, in top and side views.* ***(e)*** *Recorded (top row) and computed (bottom row) deformation of the actuator, during four representative stages.* ***(f)*** *Percentage increase in lengths and nominal area vs. the rotation angle of magnets during the contraction actuation, as predicted by FEA (lines) and measured in experiments (dots). For panels (b) and (e), colors in FEA results denote total*

displacement.

Periodic repetition of the structures in the aforementioned two actuators can be done on a plane to for much larger 2D actuators. This repetition can also be performed on an open cylindrical surface to achieve three-dimensional (3D) auxetic actuation. **Figures 4.7a** and **4.7d** illustrate the structures of such actuators, each involving 36 magnetic “bones”. The circular holes are slightly modified into alternating elliptical shapes for smoother transformation. **Figures 4.7b-f** demonstrate the shapes of the actuators in their initial configurations (left column), and in the deformed shapes after ~0.4 seconds in constant magnetic field (right column). From both experimental images (**Figs. 4.7b, e**) and FEA models (**Figs. 4.7c, f**), we observe the apparent simultaneous decrease (or likewise increase) in length in the expected axial and hoop directions (i.e., height and circumference), as well as in the third, radial direction. Such results show that these two devices indeed actuate in a 3D auxetic way. Notably, the amount of rotation for magnetic “bones” is less than 45 degrees in these 3D actuators, as the features near the inner surface will eventually come into physical contact among themselves and prevent further deformation. Such effect is both considered in FEA models and recorded in experiments.

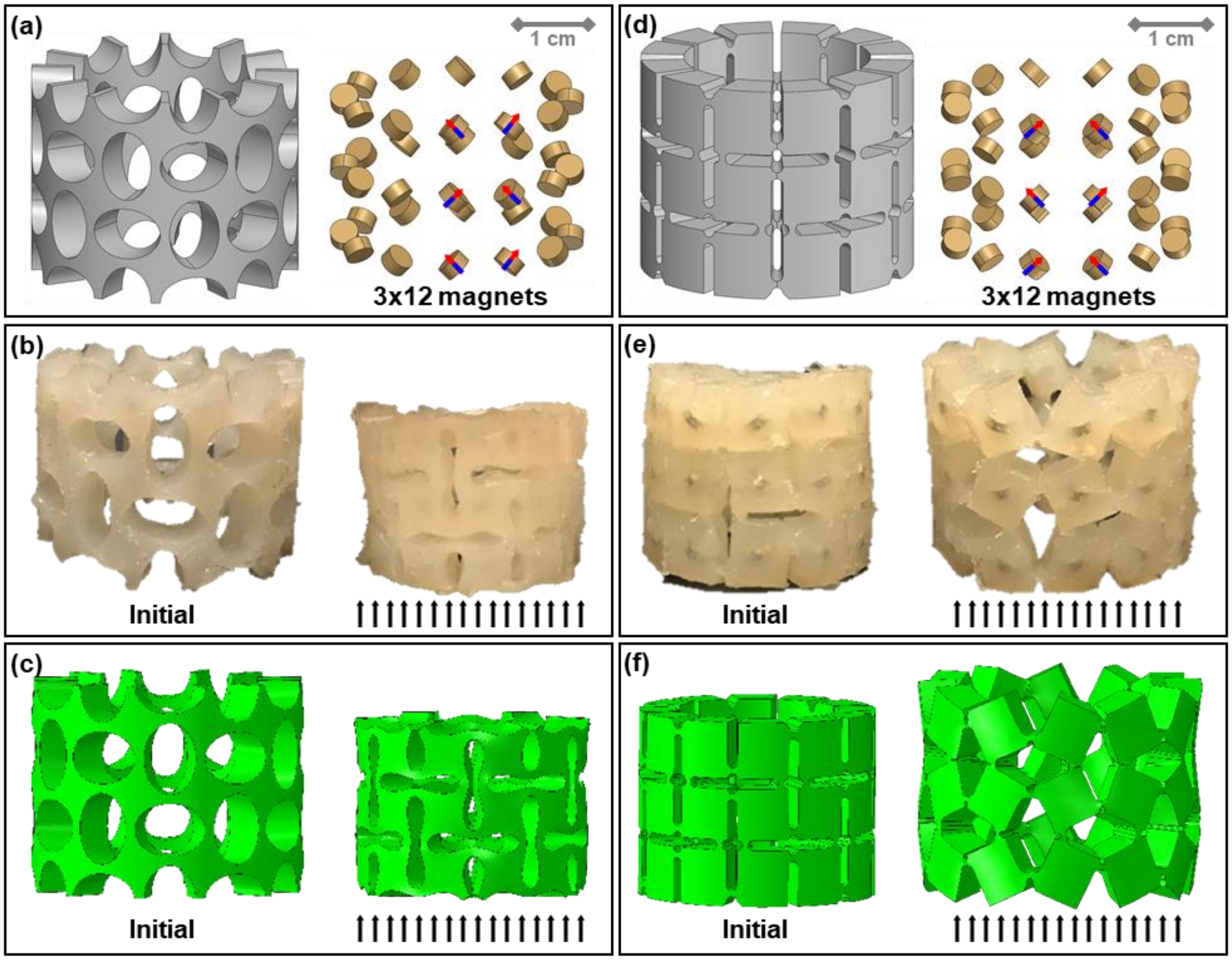

Figure 4.7 ***(a)*** *Schematics of a soft actuator for 3D auxetic contraction, featuring the "flesh" (left column) and the 36 "bones" (right column). The red/blue arrows denote the representative polarity of magnets.* ***(b)*** *Recorded and* ***(c)*** *computed shape of the actuator in (a), without (left) and with (right) external magnetic field.* ***(d)*** *Schematics of a soft actuator for 3D auxetic expansion, featuring the "flesh" (left column) and the 36 "bones" (right column).* ***(e)*** *Recorded and* ***(f)*** *computed shape of the actuator in (d), without (left) and with (right) external magnetic field.*

4.2.3 Actuators for 2D-to-3D Shape Transformation

The assembly of 2D planar patterns into complex 3D shapes is another trending research theme. Two most popular approaches for the 2D-to-3D transition across multiple length scales are: (1) utilizing the compressive buckling of thin films partially adhered to elastomeric substrates upon releasing substrate pre-stretch [30-32], and (2) applying the folding of thin films along predesigned traces (also known as "Origami") upon mechanical force and other physical/chemical stimuli [15, 30, 33-35]. Here we present three flesh-and-bone actuators for magnetically powered 2D-to-3D shape transformation, each representative of a unique strategy.

The first actuator achieves the transformation through the bending of selective "flesh" parts due to differences in stiffness. As illustrated in **Fig. 4.8a**, the structured "flesh" are composed of nine blocks, connected by thinner and narrower segments among them. Four magnetic "bones" are embedded with chosen polarities to results in the four blocks with bones at the corners. Upon an applied magnetic field (~200 mT) and due to the large difference in the bending stiffness (~10 times) between segments and blocks, a considerable overall out-of-plane displacement is achieved, forming a three-dimensional shape in ~0.17 seconds. Depending on the direction of the magnetic field, the actuator can transform between two different 3D gestures: (1) a state resembling a "butterfly" featuring high left/right and low front/back blocks under an upward magnetic field, and (2) a "saddle" state characterized by low sides and high front and back blocks under a downward magnetic field (**Fig. 4.8b**). The recorded deformation agrees with FEA calculations excellently to subtle details. From FEA results, it is found that the actuator reaches up to ~2.6 times of its height during the 2D-to-3D transformation, with the in-plane diagonal length reduced by 28.5% (**Fig. 4.8c**).

With more pronounced differences in thickness (hence bending stiffness) within the structure, an event similar to paper-folding, or "Origami", can occur [30]. **Figure 4.8d** illustrates a device actuating by the concept of Origami, where the elastomeric "flesh" is structured into a thin (~0.25 mm) membrane and thick (additional ~1.4mm) triangular or rectangular mesas above it. When a magnetic field is applied, the rectangular mesas with embedded "bones" quickly (within ~0.5 seconds) rotate to render almost perpendicular sidewalls, while the thin regions of "flesh" serve as the creases for reversible folding (**Fig. 4.8e**). Under an upward magnetic field (1^{st} column in **Fig. 4.8e**), one set of triangular mesas lifts up (marked as red in **Figs. 4.8d, e**) to form the ceiling in the generated three-dimensional structure, while the other set (marked as blue) stays low to form the ground. By reversing the applied magnetic field (3^{rd} column in **Fig. 4.8e**), the set marked as blue moves up instead and a reversed structure is shaped. Through incorporating mesas with diverse shapes and sizes in the "flesh", and placing various magnetic "bones" at different sites, these soft actuators could potentially assemble into numerous intriguing 3D Origamis, with the desirable rapid responses, easily reversed shapes, and recoverable nature.

The third actuator for 2D-to-3D transformation involves the idea of bundling two or three parallel magnetic "bones" (**Fig. 4.8f**), with some geometric similarities to the parallel radius and ulna in human's forearm. In the actuator, these "bone" bundles reside in the thicker and wider segments of "flesh", to facilitate bending in these stiffer regions by providing doubled or tripled aligning torque. In this actuator, six single "bones", six two-bone bundles, and six three-bone bundles constitute the entire skeleton. **Figure 4.8g** shows the transformation process of this actuator, from an almost flat shape into a three-dimensional complex object resembling the well-known Bird's Nest Stadium in Beijing. Potentially, a vast variety of three-dimensional structures with more convoluted geometries and curvilinear details could be quickly assembled by this type of flesh-and-bone actuators, through the inclusion of assorted bundling of "bones" and diverse shapes of "flesh" during the design process.

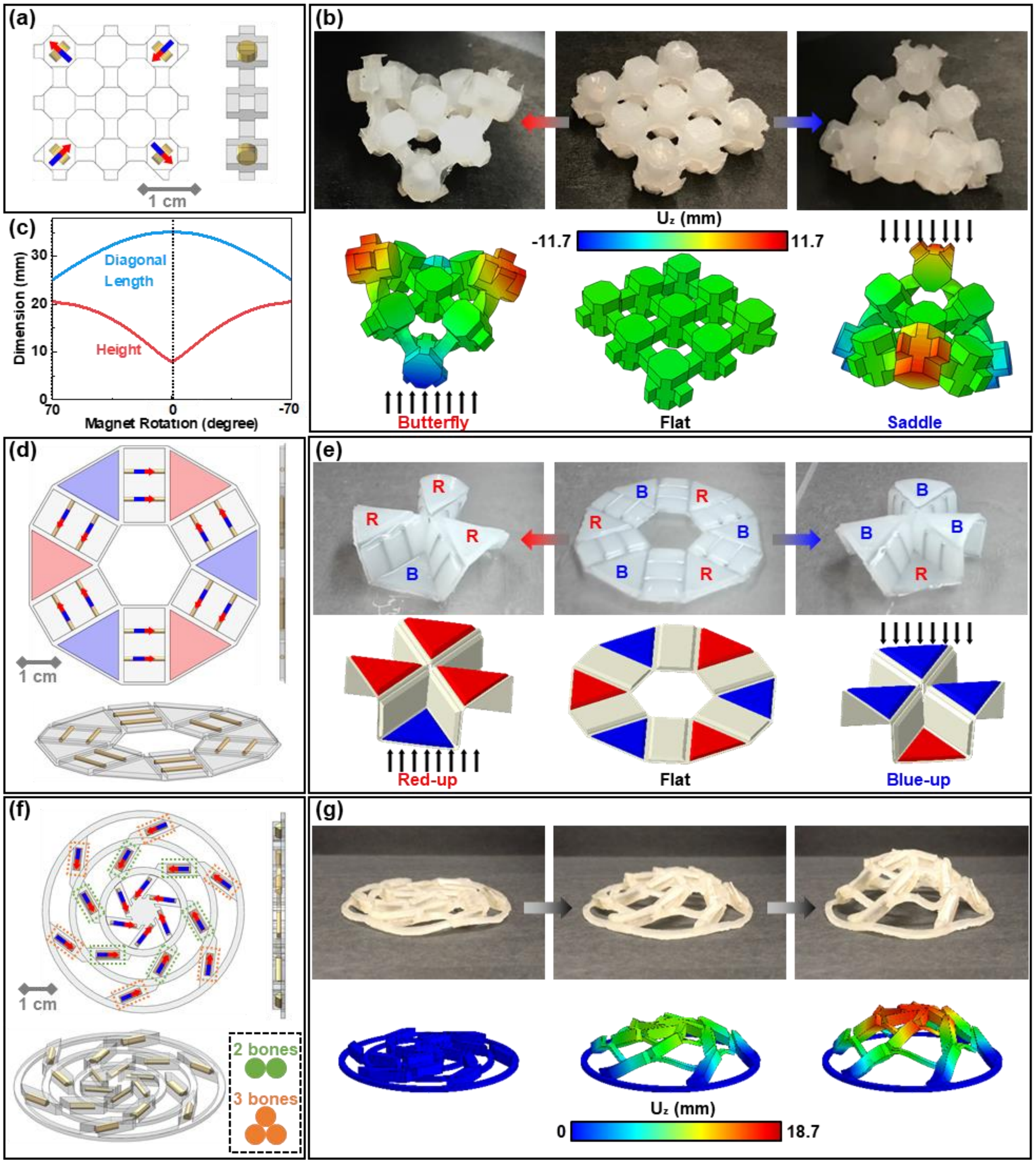

Figure 4.8 ***(a)*** *Schematics of a soft actuator for bending-based 2D-to-3D transformation, in top and side views.* ***(b)*** *Recorded (top column) and computed (bottom column) transitions among the*

"butterfly" state, the undeformed flat state, and the "saddle" state. ***(c)*** *Changes in height and length vs. magnet rotation angle during the actuation process.* ***(d)*** *Schematics of a soft actuator for Origami-type 2D-to-3D transformation, in top, side and tilted 3D views.* ***(e)*** *Recorded (top column) and computed (bottom column) transitions among the "Red-Up" state, the undeformed flat state, and the "Blue-Up" state. In photos, the letters "R" and "B" denote red and blue faces, respectively.* ***(f)*** *Schematics of a soft actuator with magnet bundles for 2D-to-3D transformation, in top, side and tilted 3D views. The inset shows a cross-sectional profile of a two-bone and a three-bone bundle.* ***(g)*** *Recorded (top column) and computed (bottom column) deformations during the actuation process. For panels (b) and (g), colors in FEA denote out-of-plane displacement.*

4.2.4 Actuators with Bistable or Multistable States

A third type of actuators build upon the bistable and multistable structures [36-38]. **Figure 4.9a** illustrates the structure of a bistable pop-up switch, with the four magnetic "bones" embedded in the thick, annular portions of the "flesh". Initially, the switch is without deformation at the "up" position (**Fig. 4.9b**, i). After the switch is pressed elastically downwards by an external force to the preset maximum displacement (**Fig. 4.9b**, ii), it won't return to the "up" position even after the applied load is retracted. Instead, the switch remains locked at a "down" position (**Fig. 4.9b**, iii), until the device is actuated by an external magnetic field for resetting back to the "up" position (**Fig. 4.9b**, iv). **Figure 4.9e** shows the elastic strain energy E and the applied force F corresponding to different stages in the loading and unloading process, as calculated from FEA, where the displacement is normalized. The "up" position is the first stable state (State 1) with elastic strain energy $E_1 = 0$, while the "down" position is a second stable state (State 2) with elastic strain energy E_2 at a local minimum. With the applied force F gradually retracted to zero, the system only recovers to the "down" position (State 2) instead of all the way to the "up" position (State 1), because of the energy barrier near State 2. An amount of elastic strain energy equal to E_2 is therefore trapped in the system. With the applied magnetic field driving the "bones" to provide this system with the additional energy, the system can overcome the energy barrier and reset to its initial configuration.

Actuators for the transitions among multiple stable states are also realized by using a conical membrane with predesigned thickness variations as "flesh", and 24 small column-shaped magnets as "bones" (**Fig. 4.9c**). The thin regions in the membrane can fold inward or remain straight to result in two different shapes. In total, this actuator has four stable configurations, namely State 1, 2, 3 and 4, with corresponding elastic strain energy $0 = E_1 < E_2 < E_3 < E_4$. At each stable state, the elastic strain energy is at the global or a local minimum, and the force transitions from zero to positive (**Fig. 4.9d, f**). Applying a downward force by a finger at the top center of the structure shifts the system to the immediate next configuration with higher strain energy (forward purple arrows), while the magnetic actuation can reset the system to the previous neighboring state (backwards gray arrows). Here, small magnets with low magnetic strength are deliberately chosen to avoid the cross transformation between two nonadjacent states. Multistable systems like this represent a step towards bone-and-flesh actuators imitating the biological structures with multiple joints in series (e.g., the arm and hand of human), where each joint can rest in either flexed or extended positions.

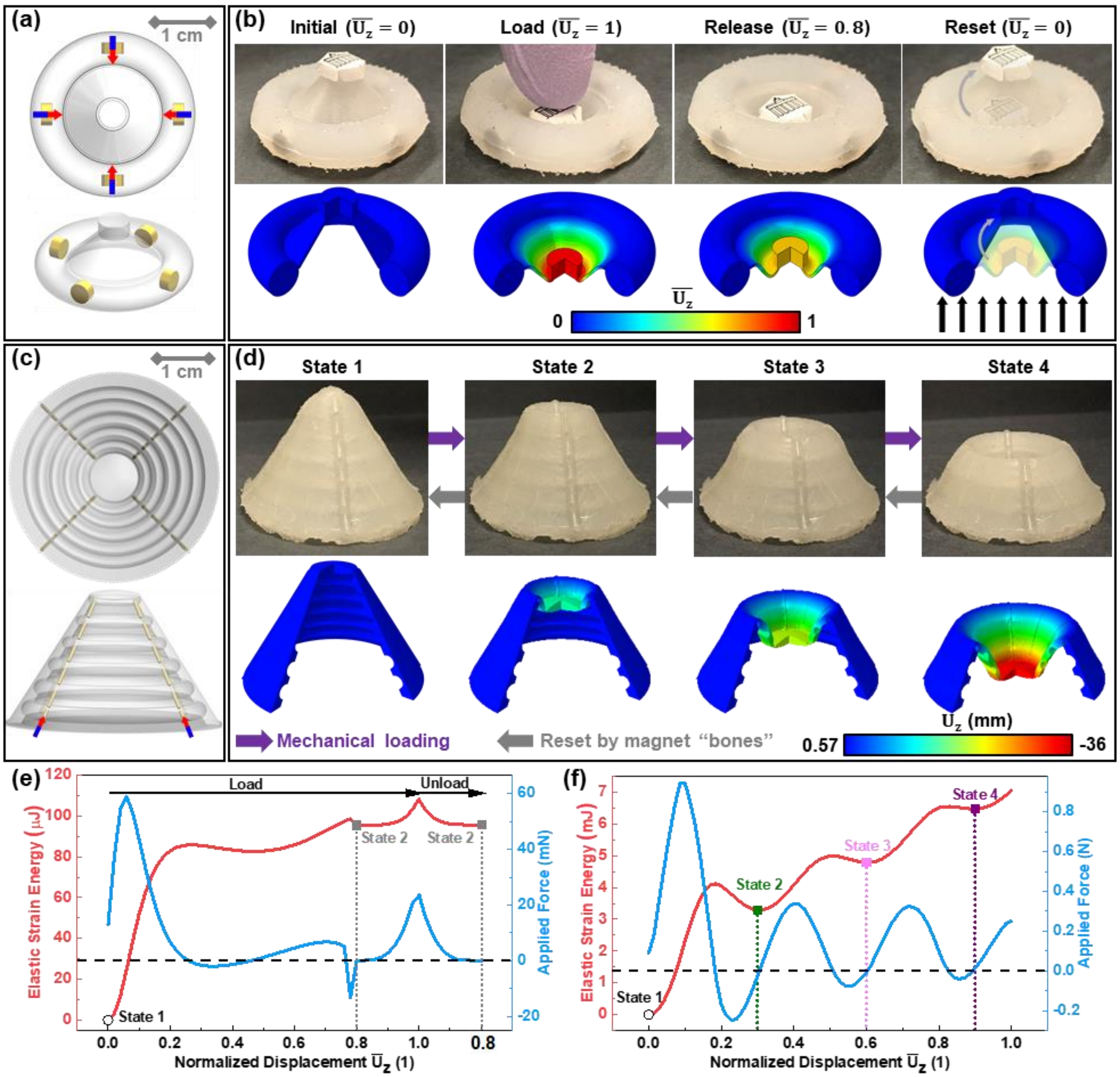

Figure 4.9 ***(a)*** *Schematics of a bistable, pop-up switch, in top and 3D tilted views.* ***(b)*** *Recorded (top row) and computed (bottom row) images for the process of mechanical loading/unloading (first three columns) and magnetically powered reset (last column). Colors in FEA denote normalized out-of-plane displacement.* ***(c)*** *Schematics of a multistable tower, in bottom and 3D tilted views. The red/blue arrows denote the representative polarity of magnets.* ***(d)*** *Recorded (top*

row) and computed (bottom row) images showing the four stable states of the system in (c). Colors in FEA denote out-of-plane displacement. ***(e-f)*** *Elastic strain energy and applied force vs. normalized displacement in the z-direction for (e) the bistable, pop-up switch, and (f) the multistable tower.*

4.2.5 A Soft Gripper

As a last example, a six-fingered, soft gripper that tightens or opens within 0.1 seconds is demonstrated, when subject to a forward or a reversed external magnetic field (**Figs. 4.10a, b)**. The aligning torque on the magnetic "bones" provides sufficient force for the reliable gripping of objects. The magnets are embedded near the base and the six fingers are made of soft "flesh" completely in order to adapt to various shapes of objects without applying excessive pressure. Experiments have been conducted to test the gripper's capability of dexterous grasping and manipulation of small objects. In the first experiment (**Fig. 4.10c**), the gripper is positioned above the 3D-printed letter "R" of the word "TRANSDUCERS", made of ABS and weighs ~0.3 grams. In a downward magnetic field (~200 mT), the gripper picks the letter up, and holds it during the transfer to another site. Afterwards, the gripper opens its fingers under an upward magnetic field to release the object. In similar experiments, we have successfully used the gripper to pick up and transfer heavier objects, such as a peanut (0.8 gram, **Fig. 4.10d**), a screw bolt (4.5 gram, **Fig. 4.10e**), and a set of nut, washer and bolt (9.0 gram, **Fig. 4.10f**). We envision that more challenging tasks such as the manipulations of heavy, brittle, slippery or weird-shaped objects could be completed by other soft grippers with flesh-and-bone constructs through rational improvements, such as including more magnetic "bones" to form multiple joints and optimizing the structures of elastomeric "flesh", etc.

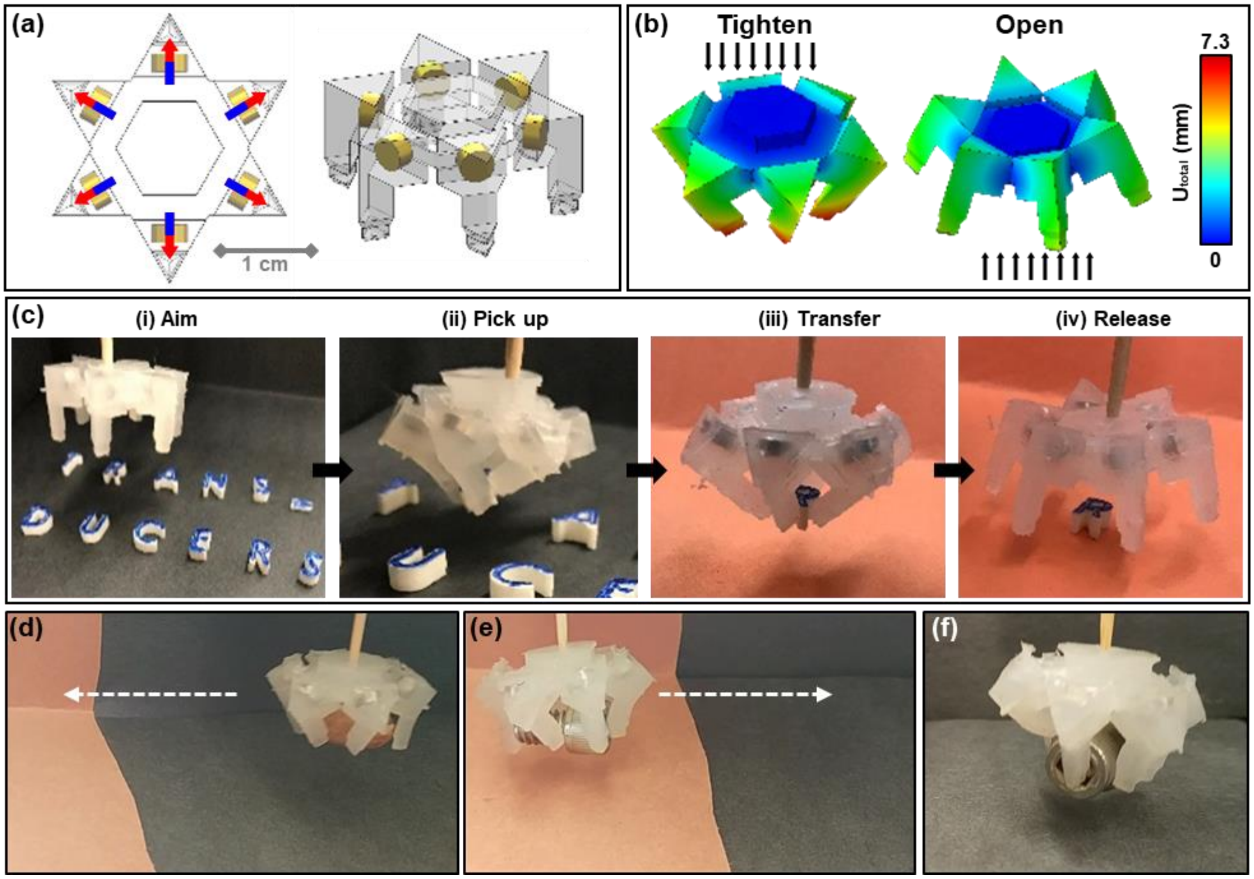

Figure 4.10 *__(a)__ Schematics of a six-finger bone-and-flesh gripper, in top and 3D tilted views. __(b)__ FEA-predicted deformation in the tightening and the opening modes. Colors denote total displacement. __(c)__ Optical images demonstrating the grasping, transferring and release of a small object. __(d-f)__ Optical images of the gripper manipulating (d) a peanut, (e) a screw bolt and (f) a set of nut, washer and bolt.*

4.3 Materials and Methods

4.3.1 Magnets for Actuators

Cylindrical NdFeB magnets with different sizes and grades were used, depending on the need of the specific actuation. The magnetic moment $\mathbf{m}$, describing the magnetic strength of a certain magnet, is proportional to the magnet's volume V and remanence $\mathbf{B}_r$ as $\mathbf{m} = (1/\mu_0)\,\mathbf{B}_r V$, where μ_0 is the permeability of vacuum. Commercial magnets of higher grades (e.g., N42) have higher remanence than those of lower grades (e.g., N35). Therefore, magnets with higher grade and larger volumes (e.g., N52 with the diameter of 1 mm and length of 1 mm, N48 with the diameter of 4 mm and length of 2 mm, N48 with the diameter of 3 mm and length of 2 mm, N42 with the diameter of 1.59 mm and length of 12.7 mm) were used for most devices for fast and large deformations, and lower grade, small magnets (N35 with the diameter of 1 mm and length of 5 mm) were used for the multistable tower demonstration. In addition, slender, column-shaped magnets were used in thin membranes for large out-of-plane displacements, while stubby, disk-shaped magnets were inserted in bulkier portions of "flesh" for in-plane-dominated deformations.

4.3.2 Finite Element Modeling of the Drop-Shock Test

3D FEA simulations of the drop-shock tests were performed using the explicit dynamic module of a commercial simulation software (ABAQUS), for a period of 3.4 milliseconds. Both the magnetic "bone" and the elastomeric "flesh" were modeled with linear brick elements with reduced integration (C3D8R). The floor (ground) was modeled as a rigid body (R3D4). For simulations with or without the "flesh" encapsulation, the column-shaped magnet had the same meshing in FEA for a fair comparison. NdFeB ($E = 100$ GPa, $\nu = 0.24$, density $\rho = 7.45$ g/cm^3) was modeled as a linear elastic brittle material, with failure criterion set as maximum principal strain exceeding 0.15%. The Ecoflex "flesh" (initial shear modulus $\mu_0 = 27.85$ kPa, bulk modulus $K_0 = 2.77$ MPa, $\rho = 1.06$ g/cm^3) was modeled as a hyperelastic material with the Neo-Hookean model. For the free fall from a height of 1.3 meters, an initial velocity of 5.05 m/s in negative Z-direction was assigned to the structure. To match the impact angle between sample and ground in experiments, the initially vertical structures were rotated by 45 degrees about the Y-axis, and then -30 degrees about the X-axis. During the simulations, energy and force were extracted as history outputs for both the cases with and without "flesh" encapsulations, and a Butterworth filter was used for the latter case to eliminate high-frequency noise in dynamic simulations.

4.3.3 Finite Element Modeling of Actuator Deformations

The deformations of actuators were modeled in ABAQUS with rotational displacement boundary conditions on the magnetic "bones". A unique data coordinate system was built on each magnet to correctly assign the rotation angle. While most of the actuators were modeled with second-order tetrahedral elements (C3D10M), the Origami-type actuator in Figs. 4.8d, e was modeled by combining continuum shell elements (SC8R) for capturing the bending of the thin membrane, and quadrilateral elements (C3D8R) for the mesas. The implicit static module was used in most actuators, except for the two actuators in Fig. 4.7. Here, an explicit dynamic model with simulation time set as 400 msec was applied to address the self-contact conditions during the deformations. Ecoflex and NdFeB were modeled using the aforementioned material properties.

4.4 Conclusions of Chapter 4

This chapter reports a bioinspired flesh-and-bone construct for building magnetically powered and untethered soft actuators. This integration of commercial off-the-shelf soft and hard materials into engineered structures not only renders fast and precise actuations with desirable compliant and impact-resistant mechanics, but also remarkably simplifies their fabrication procedures. The demonstrated devices have achieved several distinct functions, including four different auxetic expansions or contractions, three types of planar to out-of-plane transformations, actuation among bistable and multistable states, and the manipulation of small objects by a gripper structure. In the future, the bioinspired hard-soft integrated designs can be expanded using the simple fabrication procedures to accomplish more complex tasks, with the ultimate goal of building multifunctional flesh-and-bone soft robots to emulate their biological counterparts.

References of Chapter 4

[1] L. Hines, K. Petersen, G. Z. Lum, and M. Sitti, "Soft actuators for small-scale robotics," *Advanced Materials*, vol. 29, no. 13, p. 1603483, 2017.

[2] D. Rus and M. T. Tolley, "Design, fabrication and control of soft robots," *Nature*, vol. 521, no. 7553, pp. 467-475, 2015.

[3] A. Miriyev, K. Stack, and H. Lipson, "Soft material for soft actuators," *Nature Communications*, vol. 8, no. 1, pp. 1-8, 2017.

[4] L. Huang *et al.*, "Ultrafast digital printing toward 4D shape changing materials," *Advanced Materials*, vol. 29, no. 7, p. 1605390, 2017.

[5] C. Ahn, X. Liang, and S. Cai, "Bioinspired design of light-powered crawling, squeezing, and jumping untethered soft robot," *Advanced Materials Technologies*, vol. 4, no. 7, p. 1900185, 2019.

[6] T. Chen, O. R. Bilal, K. Shea, and C. Daraio, "Harnessing bistability for directional propulsion of soft, untethered robots," *Proceedings of the National Academy of Sciences*, vol. 115, no. 22, pp. 5698-5702, 2018.

[7] J. Shang and P. Theato, "Smart composite hydrogel with pH-, ionic strength-and temperature-induced actuation," *Soft Matter*, vol. 14, no. 41, pp. 8401-8407, 2018.

[8] H. Zeng, O. M. Wani, P. Wasylczyk, R. Kaczmarek, and A. Priimagi, "Self-regulating iris based on light-actuated liquid crystal elastomer," *Advanced Materials*, vol. 29, no. 30, p. 1701814, 2017.

[9] M. Behl, K. Kratz, U. Noechel, T. Sauter, and A. Lendlein, "Temperature-memory polymer actuators," *Proceedings of the National Academy of Sciences*, vol. 110, no. 31, pp. 12555-12559, 2013.

[10] X. Lu *et al.*, "Liquid-crystalline dynamic networks doped with gold nanorods showing enhanced photocontrol of actuation," *Advanced Materials*, vol. 30, no. 14, p. 1706597, 2018.

[11] Y. Cheng, K. Ren, D. Yang, and J. Wei, "Bilayer-type fluorescence hydrogels with intelligent response serve as temperature/pH driven soft actuators," *Sensors Actuators B: Chemical*, vol. 255, pp. 3117-3126, 2018.

[12] S. Wei *et al.*, "Bioinspired Synergistic Fluorescence-Color-Switchable Polymeric Hydrogel Actuators," *Angewandte Chemie International Edition*, vol. 58, no. 45, pp. 16243-16251, 2019.

[13] M. Lahikainen, H. Zeng, and A. Priimagi, "Reconfigurable photoactuator through synergistic use of photochemical and photothermal effects," *Nature Communications*, vol. 9, no. 1, pp. 1-8, 2018.

[14] L. Fang, T. Fang, X. Liu, S. Chen, C. Lu, and Z. Xu, "Near-Infrared Light Triggered Soft Actuators in Aqueous Media Prepared from Shape-Memory Polymer Composites," *Macromolecular Materials Engineering*, vol. 301, no. 9, pp. 1111-1120, 2016.

[15] S. Miyashita, S. Guitron, S. Li, and D. Rus, "Robotic metamorphosis by origami

exoskeletons," *Science Robotics*, vol. 2, no. 10, p. eaao4369, 2017.
[16] X. Yan *et al.*, "Multifunctional biohybrid magnetite microrobots for imaging-guided therapy," *Science Robotics*, vol. 2, no. 12, 2017.
[17] Y. Kim, H. Yuk, R. Zhao, S. A. Chester, and X. Zhao, "Printing ferromagnetic domains for untethered fast-transforming soft materials," *Nature*, vol. 558, no. 7709, pp. 274-279, 2018.
[18] T. Xu, J. Zhang, M. Salehizadeh, O. Onaizah, and E. Diller, "Millimeter-scale flexible robots with programmable three-dimensional magnetization and motions," *Science Robotics*, vol. 4, no. 29, 2019.
[19] J. Yan, J. J. Mecholsky Jr, and K. B. Clifton, "How tough is bone? Application of elastic–plastic fracture mechanics to bone," *Bone*, vol. 40, no. 2, pp. 479-484, 2007.
[20] E. F. Morgan, H. H. Bayraktar, and T. M. Keaveny, "Trabecular bone modulus–density relationships depend on anatomic site," *Journal of Biomechanics*, vol. 36, no. 7, pp. 897-904, 2003.
[21] D. Taylor, N. O'Mara, E. Ryan, M. Takaza, and C. Simms, "The fracture toughness of soft tissues," *Journal of the Mechanical Behavior of Biomedical Materials*, vol. 6, pp. 139-147, 2012.
[22] B. C. W. Kot, Z. J. Zhang, A. W. C. Lee, V. Y. F. Leung, and S. N. Fu, "Elastic modulus of muscle and tendon with shear wave ultrasound elastography: variations with different technical settings," *PloS one*, vol. 7, no. 8, p. e44348, 2012.
[23] J. van Kuilenburg, M. A. Masen, and E. van der Heide, "Contact modelling of human skin: What value to use for the modulus of elasticity?," *Proceedings of the Institution of Mechanical Engineers, Part J: Journal of Engineering Tribology*, vol. 227, no. 4, pp. 349-361, 2013.
[24] K. Li *et al.*, "A generic soft encapsulation strategy for stretchable electronics," *Advanced Functional Materials*, vol. 29, no. 8, p. 1806630, 2019.
[25] R. Xu *et al.*, "Designing thin, ultrastretchable electronics with stacked circuits and elastomeric encapsulation materials," *Advanced Functional Materials*, vol. 27, no. 4, p. 1604545, 2017.
[26] D. Yang *et al.*, "Buckling of elastomeric beams enables actuation of soft machines," *Advanced Materials*, vol. 27, no. 41, pp. 6323-6327, 2015.
[27] A. Rafsanjani and D. Pasini, "Bistable auxetic mechanical metamaterials inspired by ancient geometric motifs," *Extreme Mechanics Letters*, vol. 9, pp. 291-296, 2016.
[28] K. Bertoldi, M. C. Boyce, S. Deschanel, S. Prange, and T. Mullin, "Mechanics of deformation-triggered pattern transformations and superelastic behavior in periodic elastomeric structures," *Journal of the Mechanics Physics of Solids*, vol. 56, no. 8, pp. 2642-2668, 2008.
[29] Y. Cho *et al.*, "Engineering the shape and structure of materials by fractal cut," *Proceedings of the National Academy of Sciences*, vol. 111, no. 49, pp. 17390-17395, 2014.
[30] Z. Yan *et al.*, "Controlled mechanical buckling for origami-inspired construction of 3D

microstructures in advanced materials," *Advanced Functional Materials,* vol. 26, no. 16, pp. 2629-2639, 2016.

[31] Y. Zhang *et al.*, "A mechanically driven form of Kirigami as a route to 3D mesostructures in micro/nanomembranes," *Proceedings of the National Academy of Sciences,* vol. 112, no. 38, pp. 11757-11764, 2015.

[32] S. Xu *et al.*, "Assembly of micro/nanomaterials into complex, three-dimensional architectures by compressive buckling," *Science,* vol. 347, no. 6218, pp. 154-159, 2015.

[33] D. Rus and M. T. Tolley, "Design, fabrication and control of origami robots," *Nature Reviews Materials,* vol. 3, no. 6, pp. 101-112, 2018.

[34] E. Hawkes *et al.*, "Programmable matter by folding," *Proceedings of the National Academy of Sciences,* vol. 107, no. 28, pp. 12441-12445, 2010.

[35] M. T. Tolley, S. M. Felton, S. Miyashita, D. Aukes, D. Rus, and R. J. Wood, "Self-folding origami: shape memory composites activated by uniform heating," *Smart Materials Structures,* vol. 23, no. 9, p. 094006, 2014.

[36] F. Pan, Y. Li, Z. Li, J. Yang, B. Liu, and Y. Chen, "3D pixel mechanical metamaterials," *Advanced Materials*, vol. 31, no. 25, p. 1900548, 2019.

[37] S. Shan *et al.*, "Multistable architected materials for trapping elastic strain energy," *Advanced Materials*, vol. 27, no. 29, pp. 4296-4301, 2015.

[38] J. R. Raney, N. Nadkarni, C. Daraio, D. M. Kochmann, J. A. Lewis, and K. Bertoldi, "Stable propagation of mechanical signals in soft media using stored elastic energy," *Proceedings of the National Academy of Sciences,* vol. 113, no. 35, pp. 9722-9727, 2016.

Chapter 5: Summary and Future Directions

5.1 Summary

Soft and deformable electronics and actuators are interesting research topics for many potential applications. This dissertation focuses on two goals: (1) utilizations of the elastic instability in structural designs for soft systems, and (2) development of rapid and low-cost approaches for the fabrication of soft and deformable systems. The adopted intriguing elastic structures in this work, including Kirigami, curved serpentines, auxetics, bistable or multistable structures, have facilitated different electronics and/or actuator systems with unique and desirable properties, such as ultrahigh deformability, omnidirectional stretchability, and impact-resistant mechanics to name a few. This dissertation also presents simple and facile fabrication procedures for these soft and deformable electronics and actuator by easily accessible tools and off-the-shelf materials. The specific findings in the three major chapters are summarized as follows:

Chapter 2 presents a series of stretchable micro-supercapacitor patches with Kirigami-inspired constructs to achieve simultaneously high system-level stretchability and high areal coverage of functional components. The stretchable patches can be fabricated in simple steps by the graphitic conversion and laser cutting processes, using a commercial laser cutter with two different power settings. Results show the Kirigami-inspired structures can easily accommodate up to 282.5% overall elongation through buckling and postbuckling deformations, such that the strain in electrodes remains low, and the system electrochemical performances are not compromised. Various electrical connections among supercapacitors in a single patch have been obtained by using diverse Kirigami designs, with different layouts of electrodes and cuts.

Chapter 3 provides a time- and cost-effective fabrication scheme for stretchable electronics with “island-bridge” constructs, without the use of photomasks or lithography-related equipment. Instead, patterning steps are completed through a two-mode mechanical cutting process on a commercially available vinyl cutter. By adjusting the applied force and the blade depth, metal interconnects and pads can be patterned via the “tunnel cuts”, and the flexible overall structure be defined via the “through cuts”. The capabilities of the proposed method are embodied in two device demonstrations, a water-resistant, omni-directionally stretchable supercapacitor array and a skin-mounted module to monitor human breathing. These devices can sustain large geometric changes in their shapes through buckling and post-buckling deformations, and maintain excellent electrical functionalities.

Chapter 4 reports a class of magnetically powered, untethered soft actuators with a bioinspired bone-and-flesh construct. These actuators with compliant and impact-resistant mechanics can be fabricated in a simple manner, using only generic 3D printers and off-the-shelf neodymium magnets and silicone elastomers. Actuators with various shapes of elastomeric “fleshes” and different placements of magnetic “bones” can complete several distinct types of actuations, including auxetic expansion and shrinking, out-of-plane transformations, transition among multiple stable states, and manipulation of small objects. Several of these actuations are realized by rationally engineered structures with elastic instabilities with fast responses.

5.2 Future Directions

The results and findings of this dissertation can potentially benefit many research efforts. The laser graphitic conversion and cutting process described in **Chapter 2**, and the two-mode mechanical cutting process proposed in **Chapter 3** are both time-saving, cost-effective fabrication approaches for stretchable electronics without using photolithography-related cleanroom equipment. In the future, these fabrication approaches could be applied in the development of many stretchable electronics systems, such as wearable sweat sensors [1, 2], deformable power supply modules [3-5], and epidermal or implantable physiological monitors [6-8]. These fabrication approaches are particularly suitable for early-stage research and prototyping requiring short turn-around time, and with frequent design changes and limited budgets. Besides, since most vinyl cutters and laser cutters have platforms greater than 150 square inches, they can be utilized for patterning large stretchable devices that simply could not fit inside a single 6-inch or 8-inch silicon wafer.

Beyond the results of **Chapter 4**, a natural next step is to develop soft robots by combining various types of flesh-and-bone actuators. The resulting soft robots with bone-and-flesh construct could potentially perform complex tasks such as walking, climbing, jumping, or dexterous object manipulations, in a similar way to human and animals. Several challenges remain to be solved before achieving this eventual goal, including but not limited to: developing a platform with controllable, time- and space-varying magnetic field for robust remote actuation; designing structures with “flesh” of highly convoluted shapes and many magnetic “bones”; and inversely finding the initial geometries needed for actuation into a certain configuration, etc.

Finally, while structures with elastic instabilities have shown great potentials, it is still challenging to design such a structure towards a specific application. While current analytical models and computational tools have helped us interpret the underlying physics and analyze some problems, a full systematic picture is still missing. Clearly, there exists patterns that are not expressed explicitly. Recently, machine learning has been successfully used in designing structures towards specific goals in mechanical properties, such as high fracture toughness and isotropic elastic stiffness [9-11]. In the research of structures with elastic instabilities and other exotic mechanics, we believe it is promising to employ machine learning for optimizing designs and generating suitable structures specific to various application scenarios.

References of Chapter 5

[1] W. Gao *et al.*, "Fully integrated wearable sensor arrays for multiplexed in situ perspiration analysis," *Nature,* vol. 529, no. 7587, pp. 509-514, 2016.

[2] Y. Yang *et al.*, "A laser-engraved wearable sensor for sensitive detection of uric acid and tyrosine in sweat," *Nature Biotechnology,* vol. 38, no. 2, pp. 217-224, 2020.

[3] J. W. Lee *et al.*, "Soft, thin skin-mounted power management systems and their use in wireless thermography," *Proceedings of the National Academy of Sciences,* vol. 113, no. 22, pp. 6131-6136, 2016.

[4] J. Pu, X. Wang, R. Xu, and K. Komvopoulos, "Highly stretchable microsupercapacitor arrays with honeycomb structures for integrated wearable electronic systems," *ACS Nano,* vol. 10, no. 10, pp. 9306-9315, 2016.

[5] S. Xu *et al.*, "Stretchable batteries with self-similar serpentine interconnects and integrated wireless recharging systems," *Nature Communications,* vol. 4, no. 1, pp. 1-8, 2013.

[6] J. Kim *et al.*, "Battery-free, stretchable optoelectronic systems for wireless optical characterization of the skin," *Science Advances,* vol. 2, no. 8, p. e1600418, 2016.

[7] J. Liu *et al.*, "Intrinsically stretchable electrode array enabled in vivo electrophysiological mapping of atrial fibrillation at cellular resolution," *Proceedings of the National Academy of Sciences,* vol. 117, no. 26, pp. 14769-14778, 2020.

[8] D. Son *et al.*, "Multifunctional wearable devices for diagnosis and therapy of movement disorders," *Nature Nanotechnology,* vol. 9, no. 5, p. 397, 2014.

[9] G. X. Gu, C.-T. Chen, and M. J. Buehler, "De novo composite design based on machine learning algorithm," *Extreme Mechanics Letters,* vol. 18, pp. 19-28, 2018.

[10] G. X. Gu, C.-T. Chen, D. J. Richmond, and M. J. Buehler, "Bioinspired hierarchical composite design using machine learning: simulation, additive manufacturing, and experiment," *Materials Horizons,* vol. 5, no. 5, pp. 939-945, 2018.

[11] Y. Mao, Q. He, and X. Zhao, "Designing complex architectured materials with generative adversarial networks," *Science Advances,* vol. 6, no. 17, p. eaaz4169, 2020.